Dissertation
submitted to the
Combined Faculties for the Natural Sciences and for Mathematics
of the Ruperto-Carola University of Heidelberg, Germany
for the degree of
Doctor of Natural Sciences

presented by
Dipl.-Phys. Ulrich Warring
born in Wuppertal, Germany

Date of oral examination: 4 November 2009

Laser Spectroscopy on Os^-: A Prerequisite for the Laser Cooling of Atomic Anions

Referees:

Priv.-Doz. Dr. Alban Kellerbauer
Prof. Dr. Markus Oberthaler

Laser Spectroscopy on Os^-: A Prerequisite for the Laser Cooling of Atomic Anions – Laser cooling of neutral atoms or positive ions is today routinely employed in numerous experiments. Negative ions, in contrast, have distinct characteristics which hamper the application of lasers for cooling. But in 1999, the discovery of the unique bound–bound electric dipole transition in the negative osmium ion provided the motivation for a first cooling attempt. This thesis presents the first milestones toward the ultimate goal of laser cooling negative osmium, including high-resolution laser spectroscopy of the relevant bound–bound E1 transition. Its frequency – between the ground $^4F_{9/2}$ and the $^6D_{J_{e1}}$ (bound) excited states – was determined to be 257.831190(35) THz in $^{192}Os^-$, in agreement with a previous measurement, but two orders of magnitude more precise. The determination of the resonant cross-section implicitly provided the corresponding Einstein A coefficient, which was found to be $A \approx 330\ s^{-1}$. Furthermore, the isotope shift of the E1 transition and the hyperfine structure constants of the ground and excited state were obtained, for the first time, from the analysis of the spectra of all naturally abundant isotopes. The hyperfine structure revealed the heretofore unknown total angular momentum of the excited state to be $J_{e1} = 9/2$. Finally, laser spectroscopy in an external magnetic field confirmed the expected line splitting for Os^- due to the Zeeman effect. Based on all these experimental results the prospect of laser cooling negative osmium is reviewed.

Laserspektroskopie an Os^-: Eine Vorraussetzung für die Laserkühlung von atomaren Anionen – Die Laserkühlung von neutralen Atomen und positiven Ionen wird heute erfolgreich in vielen Experimenten eingesetzt. Negative Ionen hingegen besitzen Eigenschaften, die die Anwendung von Lasern zum Kühlen erschweren bzw. unmöglich machen. Die Entdeckung des bislang einzigartigen elektrischen Dipolübergangs im negativen Osmiumion zwischen zwei gebundenen Zuständen – im Jahr 1999 – lieferte die Motivation dafür, einen ersten Kühlversuch zu unternehmen. In dieser Arbeit werden erste Zwischenergebnisse dieses Projekts präsentiert. Zu diesen gehört die hochauflösende Laserspektroskopie des entsprechenden E1-Übergangs, wobei die Übergangsfrequenz in $^{192}Os^-$ zwischen dem $^4F_{9/2}$ Grundzustand und dem angregten (gebundenen) $^6D_{J_{e1}}$ Zustand zu 257.831190(35) THz bestimmt wurde. Diese Frequenz stimmt mit einem zuvor gemessenen Wert überein, hat aber eine um den Faktor 100 höhere Genauigkeit. Die Bestimmung des resonanten Wirkungsquerschnitts lieferte zudem den Einstein-Koeffizienten $A \approx 330\ s^{-1}$. Desweiteren wurden erstmals Messungen der Isotopieverschiebung des E1-Übergangs und der Hyperfeinstruktur an allen stabilen Isotopen durchgeführt und daraus die Isotopieverschiebung des E1-Übergangs sowie die Hyperfeinstruktur-Konstanten bestimmt. Dabei offenbarte die Analyse der Hyperfeinstruktur den bisher nicht bekannten Gesamtdrehimpuls $J_{e1} = 9/2$ des angeregten Zustands. Die Laserspektroskopie in einem äußeren Magnetfeld hat dieses Resultat bestätigt; das Spektrum zeigte, die erwartete Aufspaltung für Os^-. Auf Grundlage dieser experimentellen Ergebnisse werden die Anforderungen besprochen, um Laserkühlung an negativem Osmium durchzuführen.

In Erinnerung an E. W.

CONTENTS

1. Introduction 1

2. Theory 5
2.1 Atomic Anions 5
2.1.1 Structure and Characteristics 6
2.1.2 Photo-Detachment Study on Negative Osmium Ions . 8
2.1.3 Detachment Processes 10
2.2 Ion Trapping and Cooling 15
2.2.1 Confinement of Charged Particles 15
2.2.2 Sympathetic Cooling 20
2.2.3 Laser Cooling 24

3. Experimental Setup 29
3.1 Ion Source and Mass Separation 29
3.2 Laser System 31
3.3 Spectrometer for In-Beam Laser Spectroscopy 33
3.4 Penning Trap 35

4. Collinear Laser Spectroscopy 41
4.1 High-Precision Spectroscopy on $^{192}Os^-$ 42
4.1.1 Transition Frequency 42
4.1.2 Cross Section 43
4.2 Measurements on Other Isotopes of Os 47
4.2.1 Isotope Effect 49
4.2.2 Hyperfine Structure 51

5. Experiments in an External Magnetic Field 57
5.1 Zeeman Splitting of $^{192}Os^-$ 57
5.2 First Trapping Experiments with Electrons 60

6. Prospect of Laser Cooling Negative Osmium 67

7. Conclusion 73

1. INTRODUCTION

Antiprotons ($\bar{\mathrm{p}}$) are a remarkable and extreme species of negative ions. They have the same mass, but opposite sign of charge with respect to the protons – their antiparticle. The discovery of the electron's antiparticle, the positron (e^+), in 1933 [1], a striking feature of Dirac's theory of the electron, suggested that all elementary particles have an antiparticle partner. The antiproton was indeed found in 1955 [2]. The relation between particles and antiparticles is described by the CPT theorem, a well-established postulate incorporated in the Standard Model of particle physics. Today, the Standard Model is one of the most precisely tested theories next to General Relativity – the description of gravity at large scales, like the universe. A (grand) unification of both to a *Theory of Everything* may require the formulation of a quantum gravity theory. In such a theory [3], the interaction would be mediated by exchange particles, as opposed to treating gravity as a geometric phenomenon. The exact nature of the exchange bosons and the charge to which they couple determines whether such a force is always attractive or whether it may become repulsive in certain circumstances. The latter would be a violation of the weak equivalence principle (WEP), which states that the gravitational and inertial mass are identical.

Experimental tests of the CPT theorem have been performed to great precision [4]. An outstanding precision (1.8 parts in 10^{14}) was reached in the measurement of the $1S \rightarrow 2S$ electronic transition in hydrogen [5]. Current experiments at the antiproton decelerator (AD) at CERN, such as ATRAP [6] and ALPHA [7], are aiming for a comparison of that transition frequency with that in antihydrogen ($\bar{\mathrm{H}}$). Antihydrogen is the bound system of a antiproton and a positron – according to CPT invariance it should have exactly the same electronic level structure. The goal of a third group (AEgIS) is the observation of the Earth's gravitational acceleration on antimatter (antihydrogen) [8], a test of the WEP. The review article [9] describes some of the past and future fundamental tests with antimatter in more detail and introduces the production mechanisms for antihydrogen.

The sensitivity of all $\bar{\mathrm{H}}$ experiments greatly depend on the temperature of the sample. Antihydrogen is produced by recombination of positrons with antiprotons at the end of an intricate production and cooling procedure. In 2002 the groups ATHENA and ATRAP independently reported the production of low-energy antihydrogen by the controlled merging of trapped antiprotons and positrons [10, 11]. Under those experimental conditions,

two main processes contribute to the recombination [9]: first, radiative recombination $\bar{p} + e^+ \rightarrow \bar{\mathrm{H}} + h\nu$, and secondly, three body recombination $\bar{p} + 2e^+ \rightarrow \bar{\mathrm{H}} + e^+$. The formed anti-atoms are no longer trapped in the electromagnetic trap, which confines the antiprotons and positrons, and uncontrolledly leave the mixing region in all directions. Although the mixing is done in a cryogenic environment, the temperature of the resulting antihydrogen was found to be much higher than the temperature of the positron plasma [12, 13], which is in thermal equilibrium with the surrounding trap.

Recently, three distinct methods have been proposed to achieve even colder samples of antihydrogen:

1. Only a small fraction of the produced antihydrogen – the coldest fraction – is trapped in an Ioffe trap. In the subsequent step the anti-atoms are laser-cooled via the Lyman-α transition [14], this cooling scheme is shown in Fig. 1.1(a). The minimal temperature achievable via this method is the corresponding Doppler cooling limit ≈ 2.4 mK, but this temperature might still be too high for precision studies.

2. The creation, trapping and sympathetic cooling of $\bar{\mathrm{H}}^+$ with laser-cooled cations [15], e.g., Ba^+, as illustrated in Fig. 1.1(b). After successful cooling, the $\bar{\mathrm{H}}^+$ ions are neutralized by a laser pulse – enabling experiments on the remaining cold antihydrogen. For this method the final temperature of the antihydrogen is in the sub-millikelvin range.

3. The antiprotons are cooled with laser-cooled anions prior to the recombination to antihydrogen [16], as shown in Fig. 1.1(c).

The third scheme depends on a charge exchange process of highly excited positronium (Ps^*), the bound system of an electron and a positron, and antiprotons in the course of antihydrogen formation. Here, the fundamental reaction is $\mathrm{Ps}^* + \bar{\mathrm{p}} \rightarrow \bar{\mathrm{H}}^* + \mathrm{e}^-$ – the excitation of Ps to high Rydberg states enhances the charge exchange cross-section. In this process, the final temperature of the $\bar{\mathrm{H}}$ will be dominated by the initial $\bar{p}$ temperature, due to the ≈ 2000 times larger mass of the antiproton with respect to the positron.

For the sympathetic cooling of antiprotons negative ions have to be deployed, since their negative charge prevents annihilation of the negative antiprotons with the atomic nucleus – the wave function overlap of nucleons and antiprotons is greatly reduced by the Coulomb repulsion. Unfortunately, the characteristics of negative ions are not in favor of laser cooling applications. Their structure does not exhibit a large number of bound states. Strong electric dipole transitions are (almost) inexistent.

In 1999, the discovery of a bound–bound electric dipole transition in the negative osmium ion provided the incentive for a thorough investigation into the prospects for Os^- laser cooling. Its theoretical cooling limit is in the microkelvin range. Thus the cooling of antiprotons with such a cold

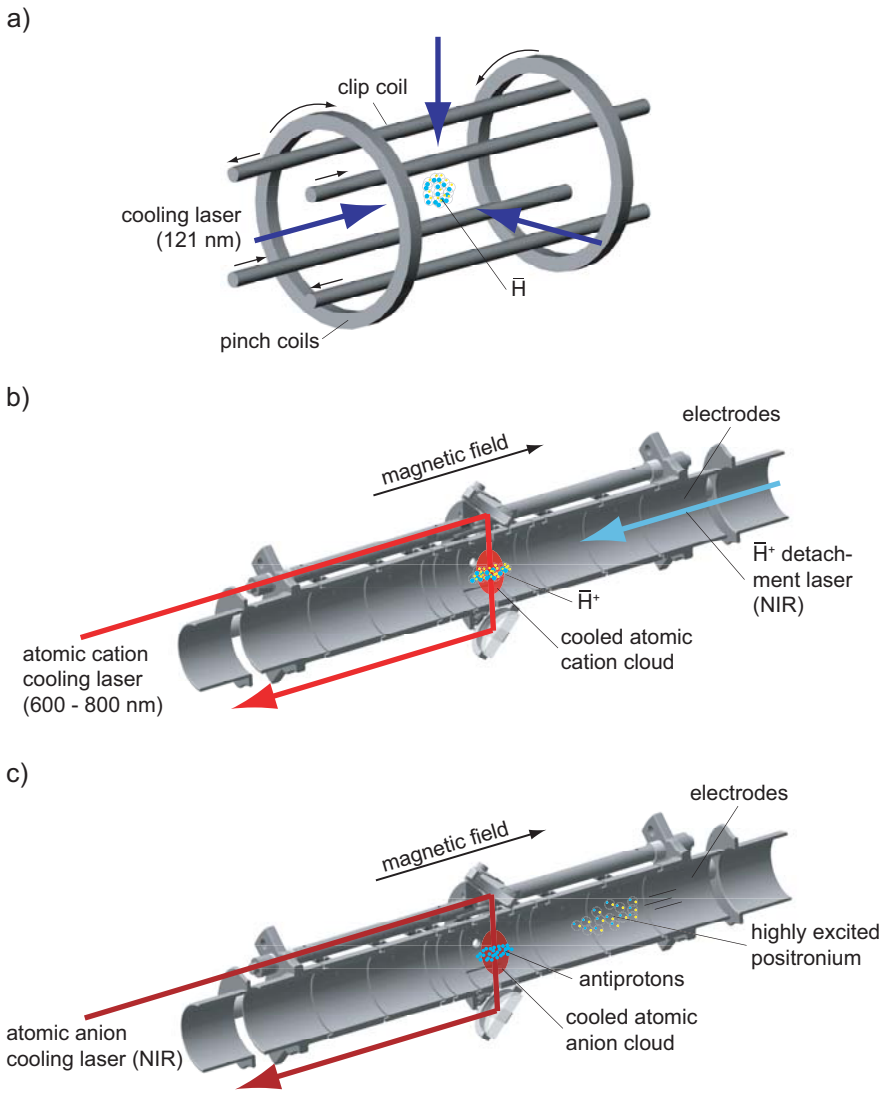

Fig. 1.1: Illustration of three possible ways to produce cold antihydrogen: (a) Trapping and laser cooling of $\bar{H}$ in a Ioffe trap; (b) Cooling of $\bar{H}^+$ with laser-cooled cations, followed by photo-detachment; and (c) Cooling antiprotons with laser-cooled anions, prior to charge exchange with highly excited positronium.

sample represents a promising route to ultracold antihydrogen. However, the characteristics of the relevant transition and the possibility of laser cooling negative osmium have to be explored in detail.

This thesis describes a study of the negative osmium ion using near-infrared laser spectroscopy performed at the Max Planck Institute for Nuclear Physics in Heidelberg. The investigation focuses on the prospects of laser cooling Os^- in a Penning trap – the UNIC project (Ultracold Negative Ions through Indirect Laser Cooling) – with a view to realizing the third production scheme for cold $\bar{H}$ introduced above.

In Chap. 2 an introduction into negative ions and a discussion of the structure and characteristics of the negative osmium ion are given. Relevant ion trapping and cooling techniques are also considered. Chapter 3 describes the components of the current setup of the UNIC apparatus, most of which were planned, designed and brought into operation during the course of this thesis. Chapters 4 & 5 present experimental results of collinear and transverse laser spectroscopy, as well as first trapping experiments in the UNIC trap. Chapter 6 discusses the possibility of and requirements for the Doppler cooling of negative osmium trapped in a Penning trap based on the results obtained in Chap. 4 & 5. Finally, Chap. 7 summarizes all results and concludes with a perspective for future experiments on the cooling of negative ions and antiprotons.

2. THEORY

2.1 Atomic Anions

Over 80% of all naturally occurring elements are capable of forming negative ions [17]. In Fig. 2.1 a portion of the periodic table of the elements is shown, including their electron affinity (EA), which is equivalent to the binding energy of the valence electron. The determination of these EAs is of interest not only on a fundamental level, but also in the applied science field. Since negative ions also often result from neutral molecules (particularly radicals) binding an additional electron, they are of importance in gas-phase chemistry and far beyond [18]. Recently EAs have been playing an important role for example, in studies of molecular clusters [19, 20], interstellar chemistry [21, 22], and even in the development of flat panel displays [23].

An introduction into the general field of negative ions can be found in the two monographs by Massey [24] and Smirnov [25], and review articles of experimental and theoretical methods present an overview of the latest results in the field [26–28]. The following section is dedicated to the origin of the binding and the resulting internal structure of atomic anions and thereby introduces the basic principles of stable negative ions.

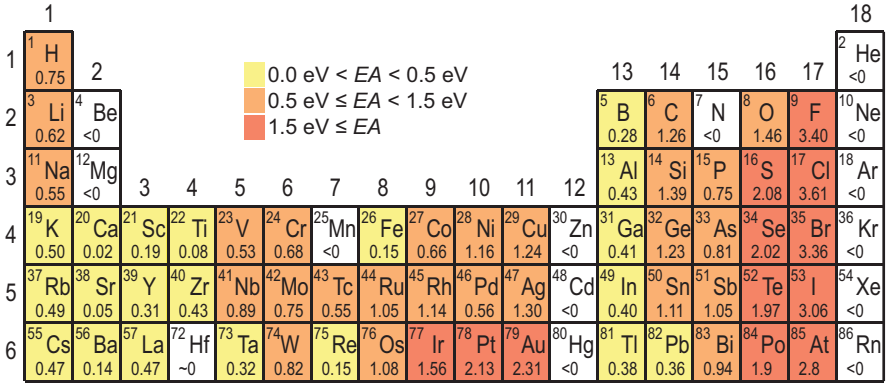

Fig. 2.1: Cutout of periodic table of elements with their electron affinities (EA) in units of eV (after Ref. [17]).

2.1.1 Structure and Characteristics

From an electrostatic point of view, an electron experiences no Coulomb force from a neutral atom, since it has no charge and no permanent electric dipole moment. Nevertheless, an electron is attracted by an isolated neutral atom. This can be understood from a semi-classical point of view. The neutral atom can become polarized in an external electric field, for example, created by an approaching charged particle. In a way analogous to the van-der-Waals interaction between neutral atoms, the force arises from a polarization effect. The interaction between the two partners induces a dipole moment, which in turn leads to an attractive potential.

In the case of the formation of an anion the electric charge of the free electron can polarize the neutral atom – resulting in an induced electric dipole moment – which is sufficient to bind the incident electron to the atom. All noble gases and some other elements do not exhibit stable negative ions, as they all inhabit a closed electron shell structure or sub-shell structure, which corresponds to a low polarizability of the atom and therefore prevent the electron from distorting the spherical symmetric charge distribution.

In the quantum-mechanical picture, binding of the excess electron involves correlations between the approaching electron and the atomic electrons. Thus the stability of the negative ions strongly depends on the sharing of the attractive field of the nucleus between the extra electron and the inner electrons. Correlation effects play a much greater role in negative ions than in atoms or positive ions, because it is the dominant contribution to the stability of such a negative system and therefore enables the understanding by means of the limitations of the independent electron model in other systems (atoms or positive ions) as well. Yet, it is not possible to calculate the binding energy to any desired precision for any other negative ion than H^- on account of the correlation effects which are impossible to handle analytically for many-electron systems. Since H^- can be treated analytically, it has been used as a model case in many calculations [29–31].

The structure of anions differs qualitatively from that of atoms and cations due to a different origin of the binding force. In atoms and cations, the Coulomb field created by the nucleus is strong and long-ranged; it falls as $1/r$ and it is capable of supporting an unlimited number of bound states converging towards the ionization limit. In contrast, the binding potential in anions for the outermost electron is much weaker and short-ranged. Since it arises from polarization effects, it falls at least as rapidly as $1/r^4$. The weakness of the potential causes a binding energy typically one order of magnitude lower than that of the parent atom. In addition it can only support a limited number of bound states, if any at all. In Fig. 2.2 the different types of potentials and their resulting level structures in atoms and anions are compared.

As mentioned above, bound excited states are rare in anions. If they ex-

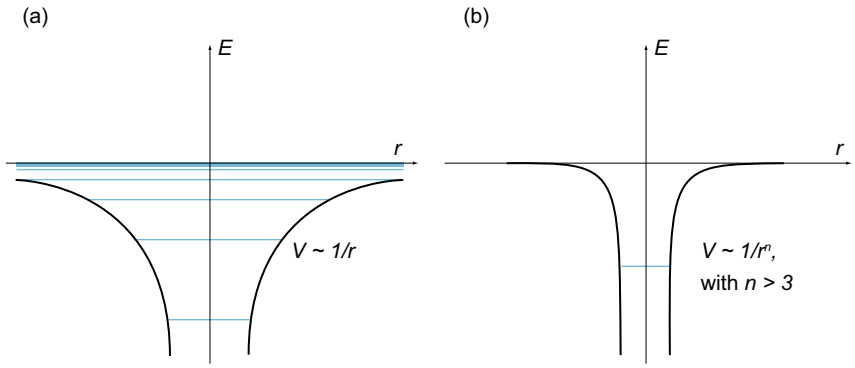

Fig. 2.2: (a) Illustration of the Coulomb potential in a neutral atom, with its infinite number of energy levels, including the Rydberg series. (b) The short-range potential experienced by the outer electron in a negative ion, with its few bound energy levels.

ist, they generally belong to the same fine structure multiplet and therefore have the same configuration and parity as the ground state. This also has an impact on the experimental methods used to investigate the electronic structure in negative ions. For example, laser absorption or fluorescence spectroscopy are impossible due to the lack of strong transitions. Hence, recent experimental studies on anions have focused on photo-detachment spectroscopy. The earliest such investigation was reported in 1973 [32]. In those kind of experiments the valence electron of the negative ion is detached via the absorption of a photon, lifting it above the neutralization threshold. A more detailed description of the experimental procedure is given in Sec. 2.1.2, where the first study on the negative osmium ion is presented, or can be found in one of several review articles [26–28].

Besides a precise determination of the negative-ion binding energies, experiments are also seeking for evidence of opposite-parity bound states. Theoretical calculations predict the existence of such states for the anions of some lanthanides and actinides [33–37] and for cesium [38–40], but the predictive power of these calculations is low. And more recent experiments have ruled out the existence of opposite-parity bound states for cesium and lanthanum [41, 42].

Today cerium is still a promising candidate for an opposite-parity bound state, but unfortunately the results of a photo-detachment experiment have not conclusively confirmed the existence of an opposite-parity bound state in this lanthanide [43]. The determination is rather difficult in this case, because the negative cerium ion exhibits a rich spectrum of resonances around the detachment threshold. These shape resonances are due to bound or quasi-bound excited states, which are commonly present in negative ions.

They lie energetically above the ground state of the parent neutral atom and reveal themselves as auto-detaching resonances in photo-detachment studies. The lifetimes for auto-detachment are of the order of $10^{-11}...10^{-16}$ s – much shorter than a possible radiative decay back to the ground state. But already in 1999 an opposite-parity bound state was experimentally found in the unique negative ion of osmium.

2.1.2 Photo-Detachment Study on Negative Osmium Ions

The experiment which led to the discovery of an opposite-parity bound state in an atomic anion represents a typical photo-detachment study [44]. We will discuss the setup and measurement principle of that experiment to introduce the basic principles of this kind of studies.

In this particular experiment, the setup consists of a negative ion source (c.f. Sec 3.1), from which the ions are extracted and formed into an ion beam with a kinetic energy of a few keV. The beam is then mass-separated and guided by ion optics into a spectrometer section. Here a tunable pulsed dye laser beam crosses the ion beam at an angle of 90°. In the course of the experiment the laser frequency is scanned, leading to a neutralization of a fraction of the ions in resonance. The remaining negative ions are deflected onto a Faraday cup, while the neutral atoms strike a microchannel plate detector (MCP) in forward direction. By recording the number of neutral particles hitting the detector as a function of the applied photon energy, a photo-detachment spectrum is obtained.

In the quoted experiment, two *strong* peak resonances and a *slow* rising near-threshold behavior from the ground state are visible in the collected data, cf. Fig. 2.3. The *narrow* peak has a width of approximately the laser bandwidth and the center is at a photon energy of 1.066316(19) eV. In contrast, the *wide* peak has its center at a 1.08132(4) eV and is about 20 times broader. Furthermore the continuum rises from the ground state threshold position at 1.07780(12) eV continuously with increasing photon energy. In the analysis, the *narrow* peak was attributed to a resonant excitation into a bound state, followed by a subsequent detachment via a second laser photon into the continuum. The *wide* peak was identified as an auto-detachment resonance. Both interpretations are supported by the measured widths of the corresponding resonances.

These experimental observations, combined with theoretical calculations on the ground state configuration of Os^- [45], yield the energy level diagram sketched in Fig. 2.4. However, the two excited states attributed to the two peak resonances lie closely around the threshold value. The ${}^6D_{J_{e1}}$ state is bound with an energy of only $\approx$ 11 meV and the auto-detachment state ${}^6D_{J_{e2}}$ is unbound by $\approx$ 3 meV, and its corresponding lifetime toward detachment is of the order of $\approx 10^{-12}$ s, as determined via the peak width. In Ref. [44], the authors give an estimate of the strength of the bound–bound

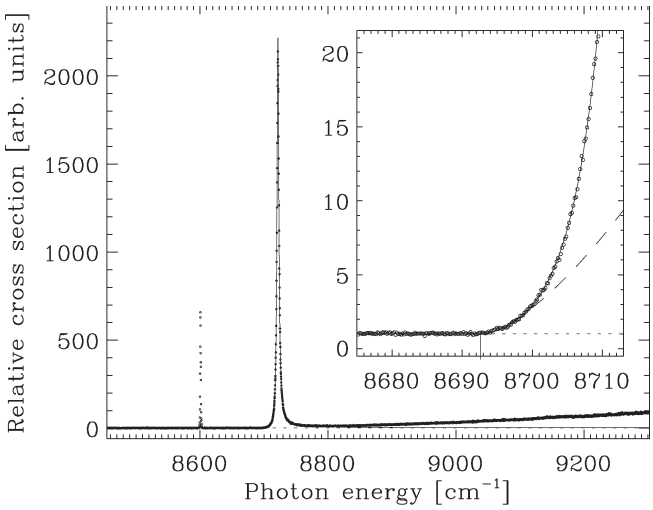

Fig. 2.3: Photo-detachment spectrum of Os^-, taken from Ref. [44]. In the inset a high-resolution scan around the ground state threshold is shown.

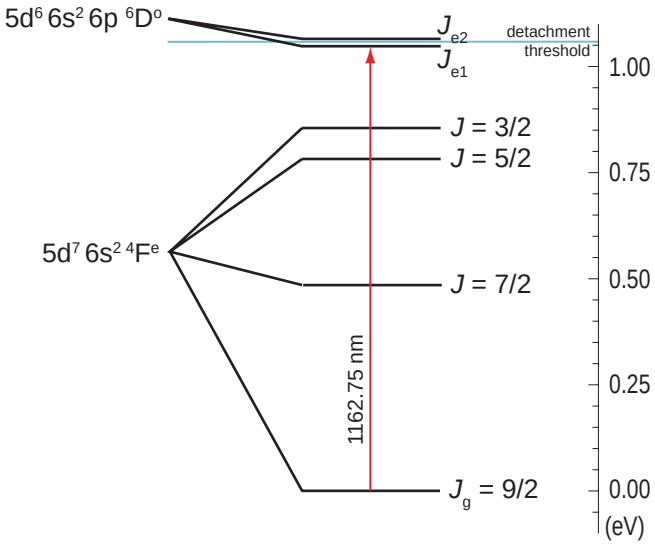

Fig. 2.4: Energy level diagram of Os^-, resulting from the theoretical considerations and the experimental results from [44, 45]. The red arrow shows the relevant E1-transition from the $^4F_{9/2}$ (ground) state to the $^6D_{J_{e1}}$ (excited) state, with the corresponding wavelength of 1162.75 nm.

transition with an Einstein A coefficient of $\approx 10^4$ s^{-1}. This transition rate is too low for a fully allowed E1 transition, but it is not uncommon for a spin-forbidden resonance in heavy elements, as is expected from the energy level diagram.

In conclusion, the cited experiment resolved two excited ionic states of odd parity in Os^-, of which one is actually a bound state. This result makes the negative osmium ion the only known atomic anion with bound states of opposite parity, since its ground state has an even parity configuration. Prior to the work reported in this thesis, the total angular momentum of the excited states was unknown.

2.1.3 Detachment Processes

As stated above, negative ions are fragile objects and therefore potential destruction mechanisms have to be carefully considered. These considerations are particularly important if the ions must be preserved for several minutes or even hours, which might be the case for the UNIC project. Hence, in the following we will consider possible ion loss processes and give estimates of the expected loss rates. Some of these discussions can be found in Ref. [16] as well.

Experimental investigations on Ca^- loss mechanisms in storage rings give some indications of their respective relevance [46], besides the theoretical assumptions made here. These experiments have shown, that detachment by blackbody radiation (BBR) seems to be a non-negligible process, in addition to collisions with residual gas and electric-field detachment. But obviously the relative importance of these processes depends on the exact experimental parameters. In the following sections, the field detachment process and the effect of black-body radiation will be considered in more detail. We will focus on the excited state ${}^6D_{J_{e1}}$ (of the negative osmium ion), since it is the most weakly bound level of interest, and the expected loss rates for all more strongly bound levels are assumed to be much lower.

Electric-Field Detachment

In order to calculate the electric-field detachment rates for excited negative ions in static electric fields, one can adopt the approximations assumed in Ref. [47], which are valid for weakly bound states. Reference [48] extends the results to alternating fields, but essentially arrives at the same estimate for static and uniform electric fields, which are to be considered here.

The valence electron is bound by $E_{\mathrm{bind}} = -1/2\ \gamma^2$ and interacts with an effective charge of the atomic core of Z. For such an electron in an orbital defined by its angular momentum quantum numbers L and M_L, the authors

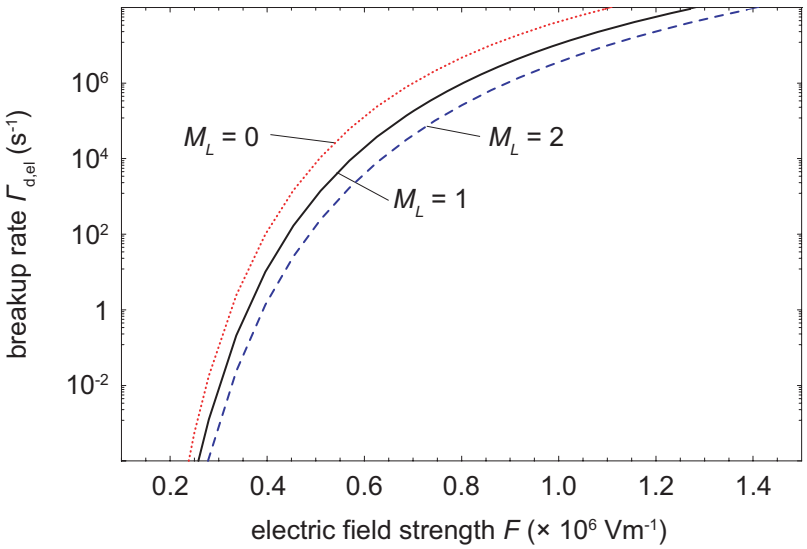

Fig. 2.5: Estimated breakup rate of the ${}^6D_{J_{e1}}$ excited state in Os^- as a function of the strength of a static electric field.

find that the rate of detachment $\Gamma_{\mathrm{d,ef}}$ is given by

$$\Gamma_{\mathrm{d,ef}} = B^2 \frac{2L+1}{2\gamma^{M_L}} \frac{M_L!(L+M_L)!}{(L-M_L)!} \left(\frac{2\gamma^2 e}{a_0^2 F}\right)^{2Z/\gamma - M_L - 1} \exp\left(-\frac{2\gamma^3 e}{3a_0^2 F}\right), \quad (2.1)$$

where B is a constant, determined by the inner form of the wave function, and F denotes the electric-field strength, e the electric charge and a_0 the Bohr radius. All quantities are in atomic units. In Fig. 2.5 the breakup rate for Os^-, in the excited state ${}^6\mathrm{D}^0_{J_{e1}}$ ($Z = 0$, $L = 2$ and $E_{\mathrm{bind}} = 11.5$ meV) and using $B = 0.03$, is plotted. The three curves indicate the different breakup rates for the three possible M_L sub-states: $M_L = 0$ (red/dotted), $M_L = 1$ (black/solid) and $M_L = 2$ (blue/dashed). It is evident that below an electric-field of 0.4×10^6 Vm^{-1} the lifetime $1/\Gamma_{\mathrm{d,ef}}$ is longer than 1 s, no matter in which M_L state the ion finds itself. In the discussion below only the $M_L = 0$ sub-state is considered, since it yields the highest detachment rates.

In case of trapped and strongly confined ions, it is crucial to estimate the expected breakup rate due to ion–ion collisions, since under these experimental conditions ion densities of $\approx 10^7$ cm^{-3} can be achieved, leading to high scattering rates. For an impact parameter of $b = 0$, cf. inset of Fig. 2.6, the ion–ion inter distance is smallest in the collision and thus the experienced electric field becomes largest. In such collisions, the thermal energy E_{therm} is transferred into potential (Coulomb) energy E_{Coul} and the distance of closest approach r_{min} is reached when $E_{\mathrm{Coul}}(r_{\mathrm{min}}) = E_{\mathrm{therm}}$. Thus, the

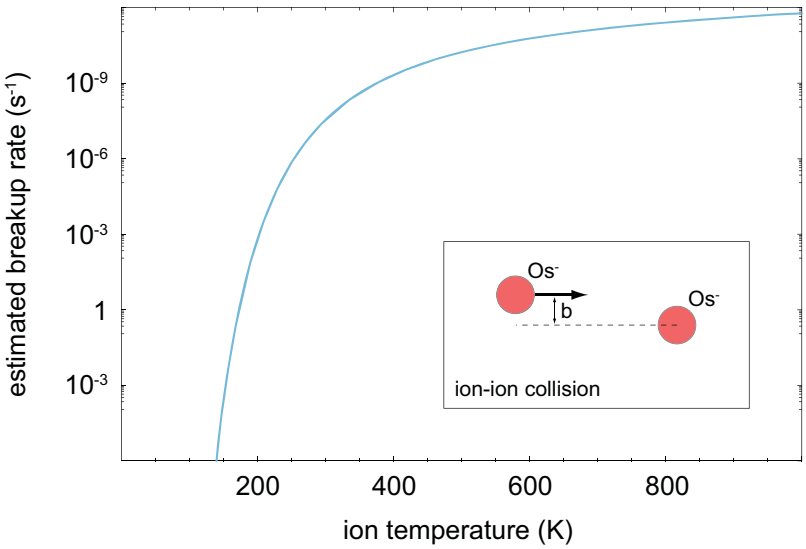

Fig. 2.6: Graph of the estimated breakup rate of the ${}^6D_{J_{e1}}$ state, due to a possible ion–ion collision, as a function of the ion temperature.

maximum electric field, and thus the breakup rate, becomes temperature-dependent. The expected rate as a function of the ion temperature is plotted in Fig. 2.6. However, this rate has to be multiplied by the actual collision rate in order to estimate the final lifetime due to this process. But since a decrease in temperature below 130 K is already sufficient to suppress this loss process by a factor of 10^8, it will not be considered here, implying that the ion temperature needs to be low before confined ions may be excited to the ${}^6D_{J_{e1}}$ state.

Detachment Due to Blackbody Radiation

Another loss mechanism is the photo-detachment by blackbody photons. In this process the cross-section has to be considered as a function of the corresponding energy.

Using the Wigner law [49], one can estimate the expected cross-section behavior near threshold, as determined in photo-detachment studies done on negative ions, see for example Ref. [50, 51]. The relevant Wigner law is the one that applies to photo-detachment, i.e., the case where the particles do not interact in the final state. For negative ions, in fact, the final state of the photo-detachment process includes one neutral particle (the atom) and one charged particle (the electron). In the following, ϵ_{thres} denotes the threshold energy and $\epsilon = hc/\lambda - \epsilon_{\text{thres}}$ the energy above threshold, while $E_{\text{ph}} = hc/\lambda$ is the photon energy. The final photo-detachment cross-section,

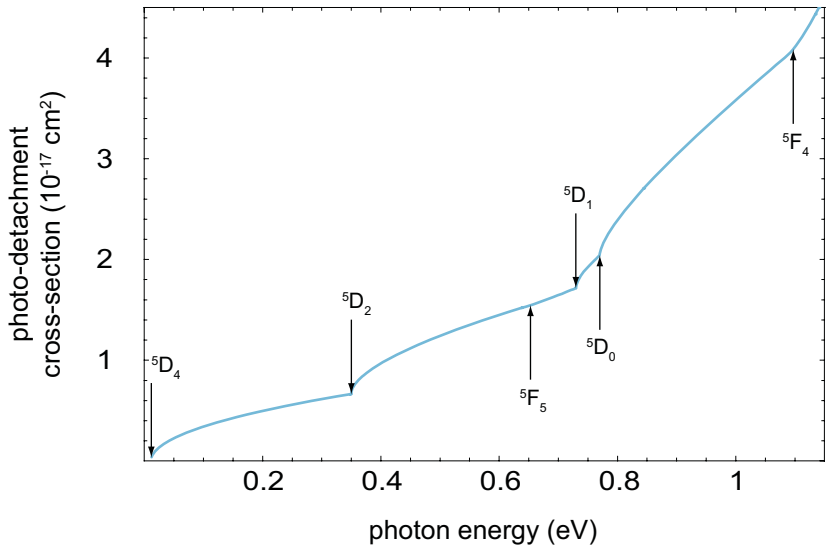

Fig. 2.7: Estimated photo-detachment cross-section from the ${}^6D_{J_{e1}}$ state, based on a sum of Wigner laws and the experimental cross-section of 4×10^{-17} cm^2 at 1.06 eV, cf. [44]. The indications at the different resonance positions show the corresponding energy levels in Os, taken from Ref. [52].

according to [49], is given by

$$\sigma_{\mathrm{d}} \propto \epsilon^{l+1/2}, \tag{2.2}$$

where l is the angular momentum of the escaping electron wave function. Note that this result does not give an absolute value for the cross-section. However, in the case of Os^-, one can take the experimentally determined cross-section of 4×10^{-17} cm^2 at $\lambda = 1162.75$ nm, cf. Ref. [44], to obtain the proportionality constant for the absolute cross-section. But in addition the final state of the atom must be considered for a complete description since, besides a pure detachment, subsequent excitation of the atom can lead to further resonances in the cross-section. In order to account for this fact the Os energy level diagram has to be considered and a sum of Wigner laws has to be established to estimate the cross-section sufficiently, see for example Ref. [50]. The corresponding energy levels are taken from [52] and lead to the plot shown in Fig. 2.7, where the resulting estimate for the photo-detachment cross-section is also displayed.

To estimate the detachment probability due to absorption of a blackbody photon, we consider the number density of photons per unit area and unit

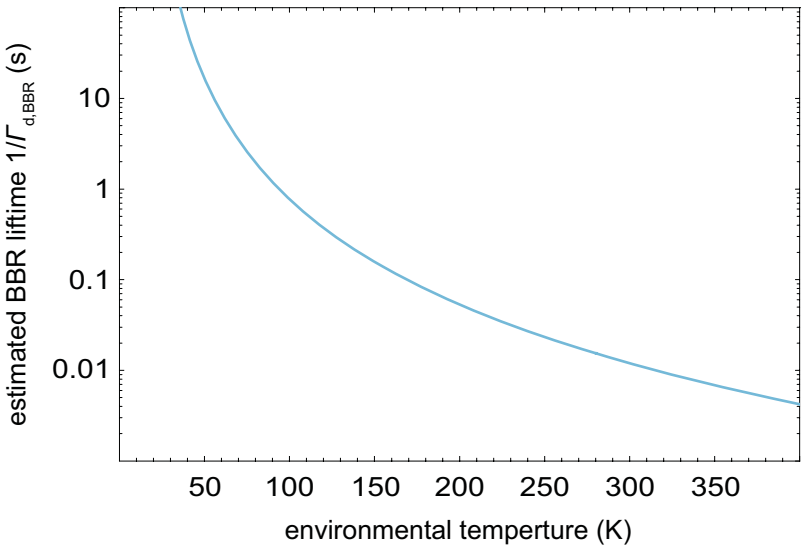

Fig. 2.8: Final estimate of the lifetime of the ${}^6D_{J_{e1}}$ state of Os^- due to BBR, versus the environmental temperature.

time. Taking Planck's law into account, we obtain:

$$n_{\mathrm{ph}}(\lambda, T) = \frac{2\pi hc^2}{\lambda^5} \frac{1}{\exp\left(\frac{hc}{\lambda k_{\mathrm{B}} T}\right) - 1}. \tag{2.3}$$

Finally, the integral of the cross-section with this result leads to the photodetachment rate

$$\Gamma_{\mathrm{d,BBR}}(T) = \int_{\lambda_{\min}}^{\lambda_{\max}} d\lambda \; \sigma_{\mathrm{d}}(\lambda)\, n_{\mathrm{ph}}(\lambda, T)\,. \tag{2.4}$$

Here, the limits $\lambda_{\min}$ and $\lambda_{\max}$ are chosen such that the integral converges in an acceptable range and is not beyond the estimated cross-section range, cf. Fig. 2.7. The resulting lifetime $1/\Gamma_{\mathrm{d,BBR}}$ is displayed in Fig. 2.8. Its strong temperature dependence suggests reducing the temperature of the environment as much as possible in order to suppress this process. A temperature of 100 K already leads to a lifetime for BBR detachment of 1 s, which is acceptable considering that spontaneous emission back to the ground state is much faster. Note that the estimate gives only a rough prediction of the expected detachment rate, due to the uncertainty in the cross-section $\sigma_{\mathrm{d}}(\lambda)$.

2.2 Ion Trapping and Cooling

2.2.1 Confinement of Charged Particles

The trapping of charged particles can be achieved in a number of ways. The most common techniques make use of oscillating electric fields (Paul trap) or static electro-magnetic fields (Penning trap) to confine non-neutral particles in a well-defined space. In particular, the Penning trap uses a strong homogeneous magnetic field (≈ few T) to trap particles in the radial direction and a static electric field to prevent particles from escaping along the axis. For a well-defined particle motion the electric potential needs to be harmonic.

Single Particle Motion in a Penning Trap

The motion performed by a single particle in a Penning trap, has been discussed extensively in Refs. [53–55], and here only a brief summary in the semi-classical treatment is presented. Trapping of charged particles in the idealized Penning trap is achieved by a uniform magnetic field $\vec{B} = B_0\vec{e_z}$ along the z axis in addition to an electrostatic quadrupole potential of the form:

$$\phi(x, y, z) = A_0 \left(2z^2 - x^2 - y^2\right). \tag{2.5}$$

Here A_0 is a parameter which represents the strength of the potential; in Sec. 3.4 it is identified with real experimental parameters. The equation of motion of a charged particle with charge q and mass M, at a point $\vec{r} = (x, y, z)$ in space, is given by:

$$M\ddot{\vec{r}} = q\left(-\vec{\nabla}\phi(\vec{r}) + \dot{\vec{r}} \times \vec{B}\right), \tag{2.6}$$

and its general solutions for the Cartesian components are

$$x(t) = r_- cos(\omega_- t + \theta_-) + r_+ cos(\omega_+ t + \theta_+), \tag{2.7a}$$

$$y(t) = -r_- sin(\omega_- t + \theta_-) - r_+ cos(\omega_+ t + \theta_+), \tag{2.7b}$$

$$z(t) = r_z cos(\omega_z t + \theta_z). \tag{2.7c}$$

Only the absolute values of q, A_0 and B_0 are important; when considering positive or negative charges, the correct sign of each value has to be assigned. The amplitudes for the so-called magnetron motion r_-, the modified cyclotron motion r_+ and the axial motion r_z are defined to be ≥ 0, and the corresponding phases (θ_+,θ_-,θ_z) are fixed by the initial conditions at time $t = 0$. The characteristic frequencies are the magnetron ω_-, modified cyclotron ω_+ and the axial frequency ω_z, which are defined as:

$$\omega_\pm = \frac{\omega_c}{2} \pm \sqrt{\frac{\omega_c^2}{4} - \frac{\omega_z^2}{2}}, \tag{2.8a}$$

species	$\omega_c/(2\pi)$	$\omega_-/(2\pi)$	$\omega_z/(2\pi)$
electrons	140 GHz	2 kHz	26 MHz
neg. osmium	400 kHz	2 kHz	44 kHz

Table 2.1: Calculated trapping frequencies for electrons and negative osmium ions, resulting from a trapping depth of $A_0 = 15.3$ V/cm^2 and a magnetic field strength of $B_0 = 5$ T.

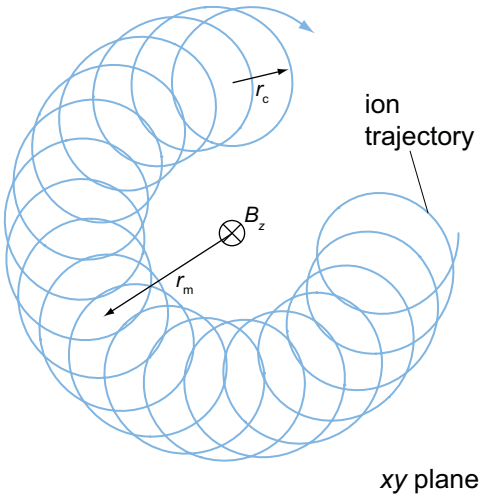

Fig. 2.9: Illustration of the ion orbit in a Penning trap, projected onto the xy plane. The magnetic field points into the drawing plane and the electric charge of the assumed particle is negative.

$$\omega_z = \sqrt{\frac{4qA_0}{M}}. \tag{2.8b}$$

Here ω_c is the true cyclotron frequency and is given by

$$\omega_c = \frac{qB_0}{M}. \tag{2.9}$$

These solutions assume the condition $\omega_c^2 > 2\omega_z^2$, since otherwise the ion motion is unstable. In Table 2.1 typical experimental values are listed for electrons and the negative osmium ions, resulting from a trapping depth of $A_0 = 15.3$ V/cm^2 and a magnetic field strength of $B_0 = 5$ T. To summarize, the ion moves in a simple harmonic motion along the z axis and a superposition of two circular motions in the x and y direction. A typical orbit in the xy plane is drawn as an illustration in Fig. 2.9, here $r_- > r_+$ and, as expected for large magnetic fields, $\omega_- \ll \omega_+$. In this parameter range the magnetron motion can be understood as an $\vec{E} \times \vec{B}$ drift of the center of the cyclotron motion around the trap axis.

The total energy E of the ion is a constant of the motion:

$$E = E_{\mathrm{kin}} + E_{\mathrm{pot}} = \frac{1}{2} M r_{\mathrm{z}}^2 \omega_{\mathrm{z}}^2 + M\Omega(\omega_+ r_+^2 - \omega_- r_-^2), \tag{2.10}$$

where the parameter Ω is given by

$$\Omega = \frac{1}{2}(\omega_+ - \omega_-). \tag{2.11}$$

In spectroscopy experiments, the reduction of the kinetic energy is of primary interest, since this will reduce the shift and broadening of transition lines. In this context it is useful to write down the mean kinetic energy in each mode:

$$\langle E_{\mathrm{kin,-}} \rangle = \frac{1}{2} M r_-^2 \omega_-^2 \tag{2.12a}$$

$$\langle E_{\mathrm{kin,+}} \rangle = \frac{1}{2} M r_+^2 \omega_+^2 \tag{2.12b}$$

$$\langle E_{\mathrm{kin,z}} \rangle = \frac{1}{4} M r_{\mathrm{z}}^2 \omega_{\mathrm{z}}^2 \tag{2.12c}$$

Thus, to reduce the Doppler width, the mode radii r_-, r_+ and r_{z} must be decreased. However, due to the negative potential energy of the magnetron motion, a decrease of r_- leads to an increase in the total magnetron energy. As a consequence the magnetron orbit is unstable toward an increase of r_- if the ion is perturbed, like in a collision with residual-gas atoms in the trap region. However, ion manipulation techniques are available which can prevent this effect.

Ion Clouds – Independent-Particle Model

In the independent-particle model the number of particles is low, the ions can be treated as non-interacting particles. Thus all assumptions concerning the ion motion in the single-particle regime hold and can be applied to each ion individually. Assuming that the energy is Boltzmann distributed, the ion population is given by:

$$\frac{n_{\mathrm{z}}}{n_0} = \exp\left(-\frac{\langle E_{\mathrm{kin}} \rangle}{k_{\mathrm{B}} T}\right). \tag{2.13}$$

Inserting here the results from Eqs. (2.12a)–(2.12c), we find that all ion radii r_-, r_+ and r_{z} follow a Gaussian distribution. The same is not true in the regime of interacting particles.

Ion Clouds – Interacting-Particle Model

In contrast to the previous model, in the interacting-particle model the particle–particle interaction has to be taken into account. One consequence can be seen in the magnetron frequency, as it is essentially independent of the ion charge, mass or position, since the electric field is linear in the radial direction. However, in the interacting-particle regime the effective electric field experienced by the ions, resulting from space charge, becomes non-linear in the radial direction and the frequency in turn becomes position-dependent. This leads to a broad distribution of magnetron frequencies and implies that the charge density is not uniform in the xy plane.

A line broadening of the cyclotron resonances is caused by frequent collisions of individual ions in the trap.[1] Inhomogeneities in the magnetic field can cause additional resonance line broadening. This can directly be seen from Eq. (2.9), when setting $B_0 = B_0(x, y)$. In a real Penning trap this of course might be the case to a certain degree, depending on the chosen materials, the quality of the magnet, and the mechanical alignment.

For the axial motion, space charge effects play a crucial role, since these effects change the effective potential for the magnetron motion, as mentioned above. But the change in the axial resonance frequency can be described more quantitatively using the results from [56, 57]. Here the space-charge-shifted axial frequency is given by:

$$\omega_{\mathrm{z,sc}}^2 = \omega_{\mathrm{z}}^2 - \frac{\omega_{\mathrm{p}}^2}{3}. \tag{2.14}$$

In this expression

$$\omega_{\mathrm{p}} = \sqrt{\frac{nq^2}{M\epsilon_0}} \tag{2.15}$$

denotes the so-called plasma frequency. Furthermore n is the particle density of the ion cloud, assumed to be homogeneous for simplicity. The factor 3 in Eq. (2.14) accounts for the geometry of the particle cloud. If the ion cloud is assumed to be an ellipsoid, the factor can be smaller (prolate) or larger (oblate). This change in axial frequency directly influences also the magnetron and modified cyclotron motion, since they are connected to ω_{z} via Eq. (2.8a).

Plasma Behavior of Ion Clouds

A non-neutral plasma is defined as a dense and/or cold particle ensemble, in which the cloud dimensions are large compared to the corresponding Debye

[1] Note: That is explicitly not the cause of the broadening in the magnetron frequency, since in this mode the ion cloud rotates around the same center and therefore different volume elements do not collide.

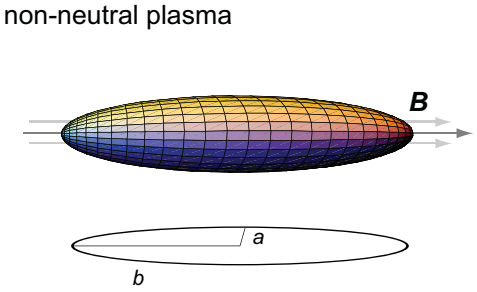

Fig. 2.10: Illustration of an ion cloud in the plasma regime. The magnetic field lines determine the symmetry axis in this non-neutral plasma with $\alpha = 10$.

length

$$\lambda_{\mathrm{D}} = \sqrt{\frac{\epsilon_0 k_{\mathrm{B}} T}{nq^2}}. \tag{2.16}$$

For instance, in laser cooled $^9\mathrm{Be}^+$ clouds the ions have been found to be in the plasma regime [58] and the study of this plasma in thermal equilibrium has shown that the shape of the trapped cloud is that of a uniformly charged spheroid, as illustrated in Fig. 2.10. The plasma frequency ω_{p} of the cloud is fixed via the aspect ratio $\alpha = b/a$ of the plasma, where $2b$ is the axial length and $2a$ is the diameter of the cloud (see Fig. 2.10).

If the plasma is in thermal equilibrium it can be excited to oscillatory modes. A theoretical description of these characteristic modes are presented in Refs. [59, 60]. In this theoretical description the plasma has a spheroidal shape and its oscillating motions are functions of the associated Legendre polynomials P_m^l and Q_m^l, where l and m are integers. All possible plasma modes of oscillation are uniquely determined by the two parameters (l, m). A measurement of the corresponding frequencies of the two lowest order modes provides a powerful tool for non-destructive diagnostics of the plasma [61], since the frequency is a function of the density and the shape of the the cloud.

In the dipole mode $(1, 0)$ the plasma shape remains unchanged, but the center of mass performs an axial motion as in the case of a single ion. The dipole $(1, 0)$ frequency ω_1 is equal to the axial frequency ω_{z} defined in Eq. (2.8b). However, the plasma density and shape are related through the following equation

$$\frac{\omega_1^2}{\omega_{\mathrm{p}}^2} = \frac{1}{\alpha^2 - 1} Q_1^0 \left(\alpha / \sqrt{\alpha^2 - 1} \right), \tag{2.17}$$

where the plasma frequency ω_{p} in turn is directly related to the plasma density n, cf. Eq. (2.15).

When the plasma is excited to the quadrupole $(2,0)$ mode, it remains spheroidal but the aspect ratio α oscillates in time. The corresponding frequency ω_2 for a strongly magnetized plasma[2] is linked to other plasma characteristics [62]. When measuring the $(2,0)$ mode frequency for two different temperatures $T_\mathrm{h} > T_\mathrm{c}$, it is possible to determine the temperature difference $\Delta T = T_\mathrm{h} - T_\mathrm{c}$ from the two corresponding frequencies $\omega_{2,\mathrm{h}}$ and $\omega_{2,\mathrm{c}}$. A temperature change of the plasma manifests itself as an upward shift of the quadrupole mode frequency and is described by the model from Ref. [60]:

$$k_\mathrm{B}\Delta T = \frac{Mb^2}{5}\left(\omega_{2,\mathrm{h}}^2 - \omega_{2,\mathrm{c}}^2\right)\left(3 - \frac{\omega_\mathrm{p}^2\alpha^2}{2\omega_{2,\mathrm{c}}^2}\frac{d^2 f(\alpha)}{d\alpha^2}\right)^{-1}, \tag{2.18}$$

where

$$f(\alpha) = \frac{2Q_1^0\left(\alpha/\sqrt{\alpha^2-1}\right)}{\alpha^2-1}. \tag{2.19}$$

This shows that the temperature variation depends on the density via ω_p, the aspect ratio α, and also on the plasma dimension b. Therefore, in order to monitor the temperature of the plasma, not only a frequency measurement is required, but also the plasma length must be determined, as described in detail in Ref. [62].

In the experiments presented in this thesis, the dipole $(1,0)$ and quadrupole $(2,0)$ modes of an electron plasma are excited, their frequencies are monitored and are used for diagnostics very similar to the ones used in the ATHENA apparatus [62].

2.2.2 Sympathetic Cooling

Laser cooling is a universal tool for preparing a cold ensemble of atoms or ions. Its major limitation is that the atomic system to be cooled must have an appropriate cooling transition. This requirement restricts the number of neutral atoms and positive ions that can be laser-cooled. With negative ions even more severe restrictions come into play. First of all, Os^- is the only atomic anion known to exhibit an electric dipole transition, a property which might be exploited for laser cooling. But the fact that the relevant excited state is very weakly bound, cf. Sec. 2.1.2, leads to further challenges because the ions in the excited state are easily neutralized, as described in Sec. 2.1.3. However, the detachment probability is strongly reduced when the ions are trapped at temperatures well below room temperature. The method proposed to achieve pre-cooling employs so-called sympathetic cooling. A schematic drawing in Fig. 2.11 illustrates the collisional cooling of one species by another actively cooled species. Its underlying principle is

[2] The plasma is in the strongly magnetized regime if $\omega_\mathrm{c} \gg \omega_\mathrm{p}$.

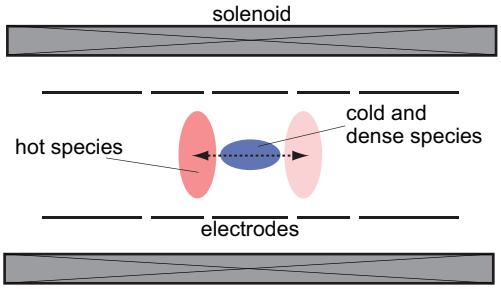

Fig. 2.11: Illustration of the sympathetic cooling technique in a Penning trap. Here the cold and dense species is trapped in the center and the hot species collides axially with the cold one and thereby cools down.

to make use of the Coulomb interaction in order to confer long-term confinement, high density and low temperature on any ion (i.e., Os^-) with an actively cooled ion species (i.e., electrons). Indeed, sympathetic cooling is applicable to any ion species and can be used in any type of trap. However, the oscillating fields of a Paul trap prevent the cooling of a light ion species with a heavy ion species. A Penning trap does not suffer from this restriction.

A first experimental realization of sympathetic cooling of $^{198}Hg^+$ ions with laser-cooled $^9Be^+$ ions was achieved in 1986 [63]. Today, electrons or positrons are used to cool antiprotons to cryogenic temperatures in Penning traps [10, 11], and electrons are also used to increase the phase space density of ion beams in storage rings [64, 65]. The review article [66] gives a broad introduction into the field of electron cooling, a special variant of sympathetic cooling.

Estimation of Expected Cooling Times

For the calculation of cooling (relaxation) times of Os^- ions in a Penning trap we consider a model described in [67]. In this particular model, the resulting cooling power is independent of the sign of charge of the colliding particles. In a more recent theoretical model of the electron cooling mechanism, however, one finds that for different signs of charge of the interacting ion species the relaxation times can vary significantly [68]. Nevertheless, in the context of this thesis, only an estimate using the first approach is carried out which yields an upper limit on the expected relaxation time.

Let us (first) consider a Penning trap which simultaneously holds a cloud of Os^- and e^-, where the electrons are at a temperature T_e and a density n_e. The trapping of $N_e \approx 10^8$ at a density of $n_e \approx 10^8$ cm^{-3} is routinely achieved. The temperature of the electrons is maintained near the surrounding (trap) temperature by emission of synchrotron radiation due to the high

acceleration in the cyclotron motion. Therefore, after the injection of hot electrons into the trap, they rapidly cool down to T_e with a time constant of [69]:

$$\tau_\mathrm{e} = 3\pi\epsilon_0 \frac{M_\mathrm{e}^3 c^3}{e^4 B^2} \approx \frac{4}{B^2}\ [\mathrm{s\ T^2}]. \tag{2.20}$$

This result shows that for a mass of 192 amu the radiation cooling would take 6×10^{16} times longer than for electrons[3] and would be not applicable in any experimental condition. In a next step, $N_\mathrm{Os} = 10^3 ... 10^5$ hot ($k_\mathrm{B} T_\mathrm{Os} \geq$ 2.5 keV) osmium ions are injected into the trap and collide in the axial direction with the cold and dense electron plasma. Now, the electrons in turn are heated by the ions but are constantly cooled via synchrotron radiation. The relaxation time constant for equilibration of the two temperatures in the two-component plasma can be written as [67]:

$$\tau_\mathrm{rel} = \frac{3 M_\mathrm{e} M_\mathrm{Os} c^3}{8\sqrt{2\pi} n_\mathrm{e} e^4 \ln(\Lambda)} \left(\frac{k_\mathrm{B} T_\mathrm{Os}}{M_\mathrm{Os} c^2} + \frac{k_\mathrm{B} T_\mathrm{e}}{M_\mathrm{e} c^2} \right)^{3/2}. \tag{2.21}$$

Here Λ is the ratio of the Debye length to the minimum impact parameter of the individual collisions and is given by:

$$\Lambda = 4\pi \left(\frac{k_\mathrm{B}}{e^2} \right)^{3/2} \sqrt{\frac{T_\mathrm{e}}{n_\mathrm{e}}} \left(T_\mathrm{e} + \frac{M_\mathrm{e}}{M_\mathrm{Os}} T_\mathrm{Os} + 2\sqrt{\frac{M_\mathrm{e}}{M_\mathrm{Os}} T_\mathrm{e} T_\mathrm{Os}} \right). \tag{2.22}$$

In order to study the time evolution of the ion and electron temperatures the following system of rate equations is established:

$$\frac{dT_\mathrm{Os}(t)}{dt} = -\frac{1}{\tau_\mathrm{rel}(t)} \left[T_\mathrm{Os}(t) - T_\mathrm{e}(t) \right], \tag{2.23a}$$

$$\frac{dT_\mathrm{e}(t)}{dt} = \frac{N_\mathrm{Os}}{N_\mathrm{e}} \frac{1}{\tau_\mathrm{rel}(t)} \left[T_\mathrm{Os}(t) - T_\mathrm{e}(t) \right] - \frac{1}{\tau_\mathrm{e}} \left[T_\mathrm{e}(t) - T_\mathrm{trap} \right]. \tag{2.23b}$$

It describes the process of thermalization and also takes into account that while the ions are cooled, the electrons are heated at the same rate. The numerical evaluation of these rate equations yields the graphs shown in Fig. 2.12. The upper graphs show the evolution of the osmium ions, whereas the lower graphs indicate the change in electron temperature. For these evaluations a magnetic field of 5 T and an initial beam energy of the osmium ions of 2.5 keV is assumed. Furthermore the surrounding temperature is assumed to be[4] $\approx$ 65 K, corresponding to an initial electron energy of 5.6 meV.

The graphs reveal the strong dependence of the cooling time on the number of osmium ions with respect to the number of electrons, and the electron density. Also, note that a variation of the magnetic field has a

[3] Assuming a magnetic field of $B = 4$ T, the cooling time for electrons is ≈ 1 s.
[4] For more details on the trap temperature see Sec.3.4.

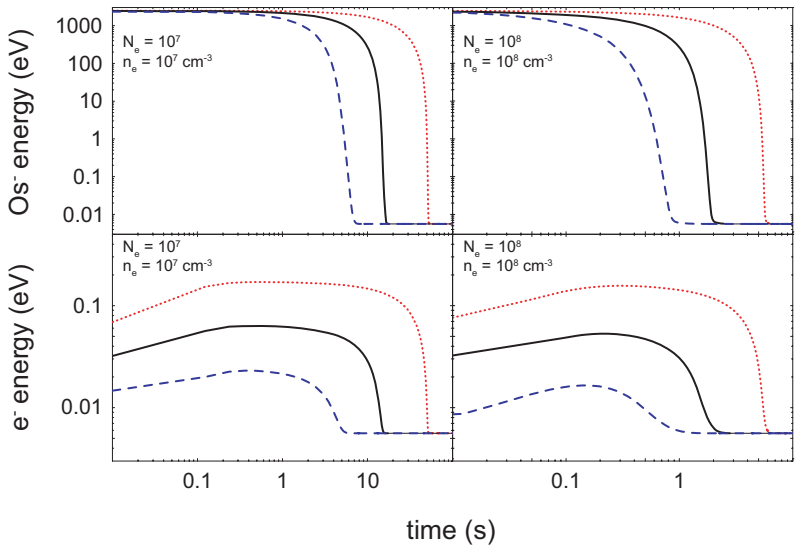

Fig. 2.12: Calculated time evolution of the Os^- and e^- energies for for different ion numbers as a function of electron number and density: $N_{Os} = 10^3$ (blue/dashed), 10^4 (black/solid) and 10^5 (red/dotted). The initial ion energy is 2.5 keV and the initial electron energy is 5.6 meV.

strong impact on the relaxation times, as it changes the electron cooling time, cf. Eq. (2.20). These results indicate that the expected sympathetic cooling time is of the order of a few tens of seconds for realistic experimental parameters.

A potential difficulty in the application of this pre-cooling technique in the trap might be the centrifugal separation of the electrons and the heavy ions, thereby reducing the spatial overlap of the two species. In a Penning trap both species rotate at the same magnetron frequency, which depends on the trap potentials, magnetic field and space charge effects. It has been noted that in equilibrium a separation occurs as long as the difference in the centrifugal potentials $(M_1 - M_2)\omega_-^2 r_-^2$ is larger than their thermal energy $k_B T$ [70]. The only direct observation of such separation was reported in the system of laser cooled Be^+ and Hg^+ [63], but cooling was nevertheless achieved. Furthermore the results from ATHENA and ATRAP concerning the cooling of antiprotons with electrons show the successful use of that method [10, 11]. It has to be noted that only the axial motion of the hot species is cooled via this technique. In order to cool the radial motions as well, a coupling of the cyclotron motion to the axial motion is required. To a certain degree this is already the case for particles trapped in a non-ideal Penning trap, with a slight misalignment between the magnetic and electric fields. At magnetic field magnitudes of a few Tesla, this might be sufficient to ensure cooling of the radial motions.

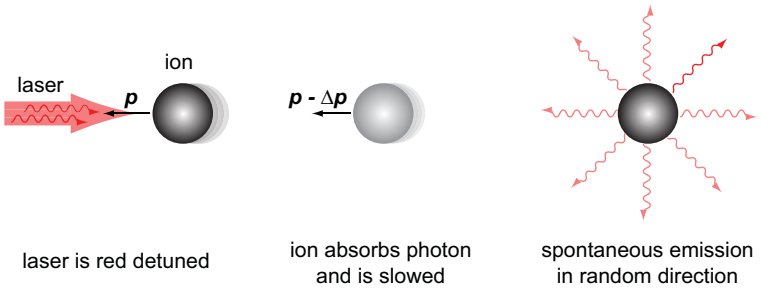

Fig. 2.13: Illustration of the laser cooling principle in three steps. The atom or ion absorbs a photon and is slowed down. Followed by spontaneous emission in a random direction. On average the ion is slowed down (cooled).

2.2.3 Laser Cooling

The first laser cooling of positive ions was achieved in 1978 [71, 72]. Until now, three different atomic ion species have been laser-cooled in a Penning trap: Mg^+, Be^+ and more recently Ca^+ [71–73]. This limited number of ion species cooled in a Penning trap is owed to the complex level structure resulting from the Zeeman splitting in magnetic fields. This results in numerous possible decay channels which must be repumped to ensure a closed cooling transition, requiring several laser systems. In case of negative ions, further challenges arise due to the higher photo-detachment rate.

Principle of laser cooling

The basic principle of laser cooling involves the absorption and subsequent spontaneous emission of photons, leading to a light force as illustrated in Fig. 2.13. This force is velocity-dependent due to the Doppler effect: atoms moving in the opposite direction of a red-detuned laser beam will scatter photons at a higher rate than those moving in the same direction.

Considering an atomic two level system with an excitation energy $\hbar\omega_0$. Now, an ideally monochromatic laser field (photon energy: $\hbar\omega_{\mathrm{las}}$), traveling in the z direction, acts on that system. The light resonantly excites the atom if the atomic velocity component v_z causes a Doppler shift that matches the detuning of the laser:

$$v_z = \frac{\omega_{\mathrm{las}} - \omega_0}{k_z}, \tag{2.24}$$

where $k_z = \omega_{\mathrm{las}}/c$ is the wave number of the light. Since the atom absorbs the energy $\hbar\omega_{\mathrm{las}}$ from the laser field, it also experiences a recoil due to momentum conservation. Hence the particle momentum changes by

$\Delta p_{\mathrm{ph}} = \hbar k_z$ in the direction of the light. When the atom decays via a spontaneous emission, the direction of the outgoing photon is independent of the direction of the initial laser field, and the recoil momentum occurs in a random direction. On average, the momentum transfer due to spontaneous emission is zero, and the atom experiences an overall momentum transfer of Δp_{ph}, leading to a velocity change of

$$\Delta v_z = \frac{\hbar k_z}{M}. \tag{2.25}$$

But since the spontaneous emission causes the atom to recoil in random directions, these recoil kicks lead to a random walk in momentum space. And fundamentally,a lower limit on the temperature achievable using this method is set by the recoil energy

$$E_{\mathrm{recoil}} = \frac{(\hbar k)^2}{2M}. \tag{2.26}$$

More detailed considerations on the theoretical cooling limit yield to the following temperature limit [74–76]:

$$T_{\mathrm{limit}} = \frac{\hbar \Gamma_{\mathrm{nat}}}{2k_{\mathrm{B}}} \tag{2.27}$$

where Γ_{nat} denotes the natural radiative line width of the cooling resonance. This key result is the Doppler cooling limit and is only valid for a laser detuning of $\delta = \Gamma_{\mathrm{nat}}/2$.

Since the laser bandwidth is finite ($\Gamma_{\mathrm{las}} > 0$), it cannot be neglected when the absorption line width Γ_{res} is of the same order of magnitude, cf. Fig. 2.14. Starting with a hot ensemble of atoms or ions – when the absorption line is broad $\Gamma_{\mathrm{res}} \ll \Gamma_{\mathrm{las}}$ – the laser width can be neglected and red-detuned, resulting in cooling (see upper graph in Fig. 2.14). Cooling is most effective when the laser light is detuned by $\delta = \Gamma_{\mathrm{res}}/2$ [77]. As the absorption line gets narrower (reduction of Doppler width), the position of the central laser frequency must be adjusted for optimal cooling (see lower graph in Fig. 2.14). Finally, part of the laser light is blue-detuned resulting in a small heating effect, but cooling is still dominant. Evidently, the achievable temperature is limited by the finite laser bandwidth, and the final temperature can be estimated by replacing Γ_{nat} by Γ_{las} in Eq. (2.27).

In order to cool an atom or ion from a temperature T_{h} to a temperatures $T_{\mathrm{c}} < T_{\mathrm{h}}$, a number

$$N_{\mathrm{ph}} = \frac{p(T_{\mathrm{h}}) - p(T_{\mathrm{c}})}{\Delta p_{\mathrm{ph}}} \tag{2.28}$$

of photons must be emitted via spontaneous emission. Considering the natural linewidth of the cooling transition, an estimate on the total cooling time is given by:

$$t_{\mathrm{cool}} = \frac{4\pi N_{\mathrm{ph}}}{\Gamma_{\mathrm{nat}}}. \tag{2.29}$$

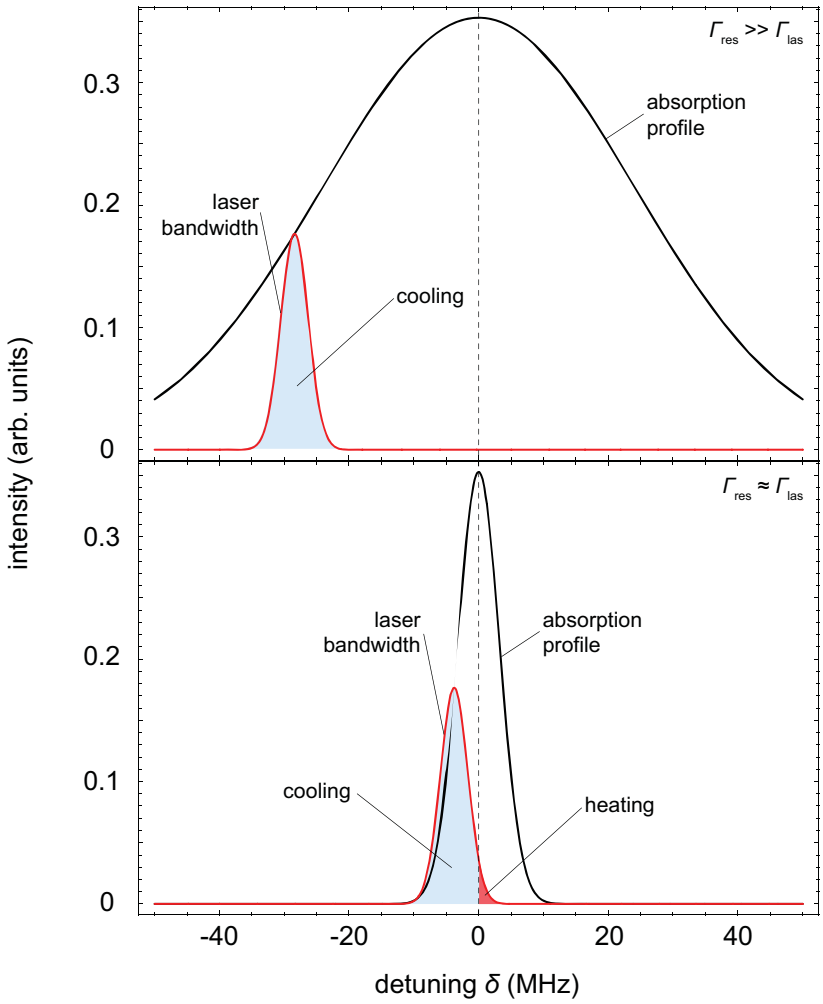

Fig. 2.14: Decrease of the absorption line width (black line) in the course of laser cooling. In addition the red-detuned laser line (red line) is shown, including an illustration of the decrease in cooling efficiency due to the finite laser bandwidth.

This result leads to additional concerns for successful laser cooling. Because only spontaneous emission contributes to cooling, the laser intensity must be kept as low as possible to avoid decay via stimulated emission.

Laser Cooling in Ion Traps

Laser cooling applied in an ion trap is to some extent different than the cooling of freely moving particles. The ion motion in a radio frequency (RF) trap can be approximated as a superposition of three harmonic oscillations along three orthogonal axes. Laser cooling in such traps leads to a tight confinement in all three dimensions. In contrast, ions in a Penning trap perform the superposition of two circular motions in the radial plane, cf. Sec. 2.2.1. As a result, laser cooling is less straightforward in this system and the confinement in the radial plane may be poor [75]. In addition, the energy levels of atomic ions display strong Zeeman splitting when confined in the high magnetic field of a Penning trap, thus requiring a more complicated laser system compared with having the same ion species confined in a RF trap. However, better control over the radial motion can be achieved by the axialization technique [78], or the rotating-wall technique suitable for an ion cloud/plasma [79]. The latter has been demonstrated in conjunction with laser cooling [80], thereby overcoming one of the disadvantages of a Penning trap. Furthermore confinement in a Penning trap is provided by the homogeneous magnetic field together with moderate static voltages applied to the electrodes (few tens of volts) and the use of static fields avoids the heating of the ions due to oscillating fields. In addition, the electrode structure can be larger than in RF traps while maintaining the confinement strength. Other heating effects, such as patch potentials on the mechanical surfaces, are also alleviated in larger traps.

Independently from the type of trap used, laser cooling of confined particles can imply further characteristics. Assuming that the trapped particle is moving longitudinal to the laser beam in an one dimensional harmonic potential of the form

$$\phi(r) = \frac{1}{2} M \omega_{\mathrm{trap}}^2 r^2, \tag{2.30}$$

where ω_{trap} is the angular frequency of oscillation and r is the position of the particle in the trap. When considering classical motion, the velocity of the trapped particle is given by $v(t) = v_0 \cos(\omega t)$. In comparison with the spontaneous transition rate Γ_{nat}, there are two limiting cases: (1) $\omega_{\mathrm{trap}} \ll \Gamma_{\mathrm{nat}}$ is called the *heavy-particle limit* and (2) $\omega_{\mathrm{trap}} \geq \Gamma_{\mathrm{nat}}$ is called the *fast-particle limit*.

In the first case, for a constant laser detuning $\delta = \omega_{\mathrm{las}} - \omega_0$, the laser cooling process takes place at almost constant velocity and constant position. Here the particle exchanges one or several recoil momenta with the laser field every time it crosses the resonance velocity expressed by Eq. (2.24), and the

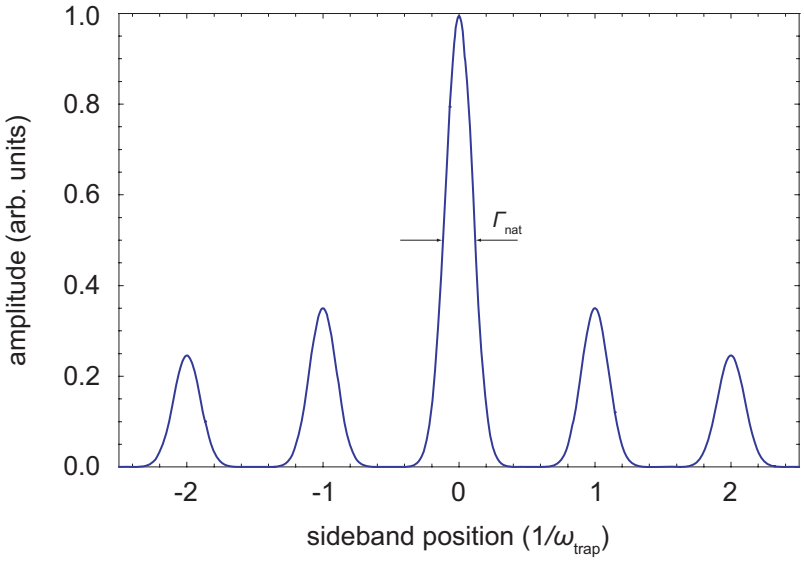

Fig. 2.15: Illustration of sidebands in a harmonic trap due to frequency modulation, in the *fast-particle* limit

situation is similar to the one of a freely moving particle.

In the second limiting case $\omega_{\mathrm{trap}} \geq \Gamma_{\mathrm{nat}}$, the particle motion is fast, and the spontaneous emission occurs over an extended part of the ion's trajectory. The rest frame resonance frequency ω_0 seems to be modulated by the Doppler shift $kv(t)$. As a result, sidebands on either side of the resonance frequency appear. The relative strength of the lth sideband is given by $|J_l\left(kv_0/\omega_{\mathrm{trap}}\right)|^2$, where J_l is the Bessel function and ω_{trap} is the distance between two sidebands, cf. Fig. 2.15. In this case, cooling can be achieved by tuning the laser frequency to a red sideband, below the carrier resonance. This cooling principle is called sideband cooling.

3. EXPERIMENTAL SETUP

The UNIC apparatus is installed at the Max Planck Institute for Nuclear Physics (MPIK) in Heidelberg, Germany. Its construction and assembly started in August 2007. The apparatus consists of an ion source including a mass separation unit, a laser system, a spectrometer for in-beam laser spectroscopy, and a cylindrical Penning trap. In the following, all of these components are presented in detail.

3.1 Ion Source and Mass Separation

There are several experimental techniques available which allow the production of negative ions. The three main methods are [81]:

1. Charge exchange of a positive ion beam in a gas or metal vapor;
2. Extraction of negative ions out of a Penning-type or plasma source; and
3. Sputtering from a cesium covered surface.

Due to the high melting point of osmium (≈ 3300 K) it is most convenient to use the third method for the production of negative ions of this element.

In our experimental setup the negative osmium ions are produced with a Middleton-type sputter negative-ion source [82]. The working principle is illustrated in a cross-sectional view in Fig. 3.1. A water cooled-cathode contains the target material, in this case osmium powder, which is compressed into a cartridge and later screwed onto a supporting rod. A constant flux of cesium vapor is delivered from a heated reservoir within the source chamber. The cesium fulfills three distinct tasks in the negative ion production mechanism [83]. First, part of the vapor condensates on top of the target material and covers its surface with roughly half a mono-atomic layer. This coverage lowers the effective work function of the surface and thereby enhances the extraction efficiency for atoms out of the bulk. Secondly, some cesium atoms are ionized in the ionizer and accelerated toward the target by a voltage of typically $U_{\mathrm{cath}} \approx 1.7$ kV. The energy deposited by the impacting cesium ions enables atoms from the target material to exit the bulk. Some of these atoms, typically less than 10%, can bind an electron from the neutral cesium layer, which constitutes the third task of the cesium.

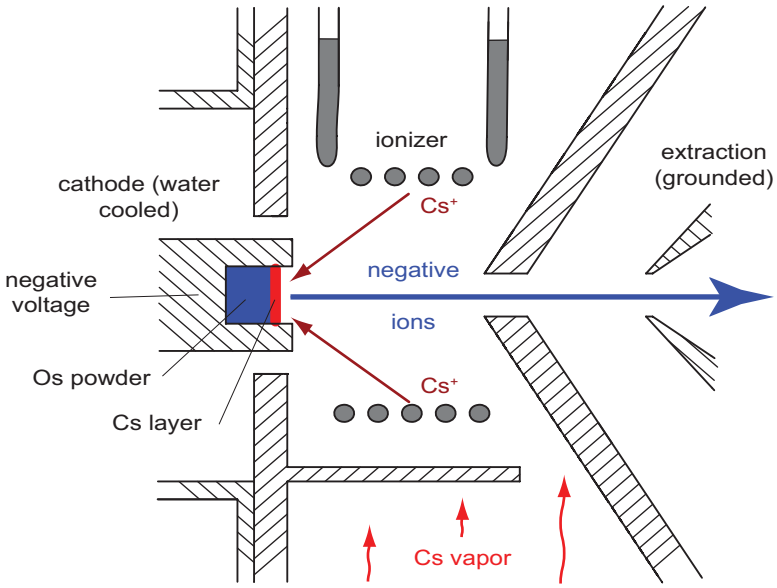

Fig. 3.1: Sketch of the Middleton-type sputter negative-ion source (MISS) in a cross-sectional view, illustrating its working principle.

The resulting negative ions are accelerated by a voltage applied to the extraction aperture to form an ion beam whose energy can be tuned in the range of $E = 1.0...6.5$ keV. Figure 3.2 shows the ion beam optics and mass separation unit for preparing an isotopically pure beam for further use. The einzel lens and the first electrostatic quadruple triplet shape the ion beam and guide it into the mass-separating magnet. In the first diagnostic unit a Faraday cup and a scintillator crystal can be moved in and out of the beam axis. With the Faraday cup the total ion beam current is recorded, and the source parameters can be optimized by maximizing the ion current. The scintillator crystal allows a rough monitoring of the ion beam shape. With these tools the focusing into the mass-separating magnet is checked. The mass separation itself is done in the dipole magnet ($R = 500$ mm) with a typical resolving power of 180. The magnet focuses the ions into the second diagnostic unit, where a second Faraday cup records the mass spectrum as a function of the applied magnetic field. A typical result of such a scan is shown in the inset of Fig. 3.2. After mass separation, the ion beam consists of over 90% of the desired osmium isotope. In the case of $^{192}Os^-$, an ion current of 50 nA is delivered for further use, including only low levels of impurities of $^{190}OsH^-$ and $^{192}OsH^-$. The next beam line component is another electrostatic quadrupole triplet, which is used to optimize the beam transmission through the next components, i.e., the electrostatic bender, the Penning trap and/or the spectrometer section. For a more detailed description of the ion source and the ion-optical setup the reader is referred

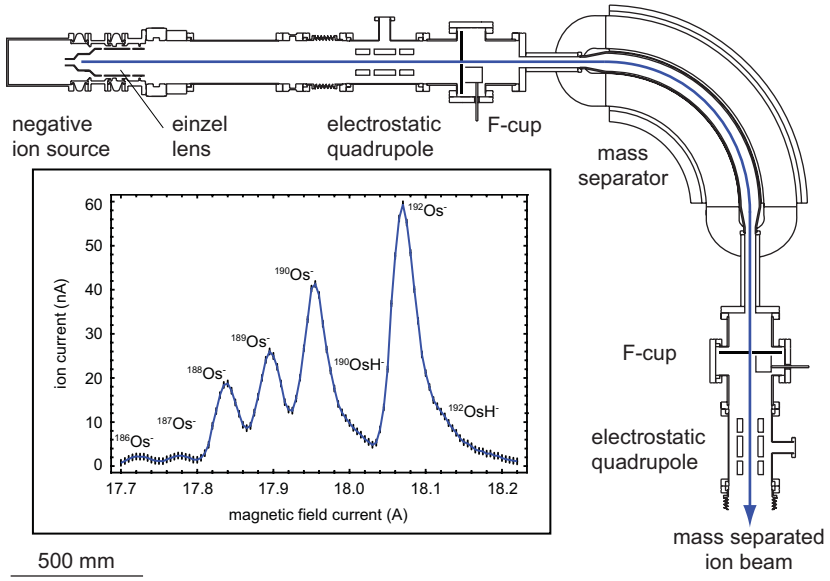

Fig. 3.2: Ion beam setup including the mass separation unit. Inset: Typical mass spectrum, which shows that almost every stable Os isotope is resolved and that some contamination of OsH^- molecules is present.

to the diploma thesis of Jan Meier [84].

3.2 Laser System

In order to perform high-resolution laser spectroscopy on the negative osmium, a narrow-bandwidth laser in the near infrared ($\lambda \approx 1163$ nm) is required. For this spectral region, commercial offerings of suitable laser systems are scarce, and the choice fell to a continuous-wave optical parametric oscillator (cw-OPO) system custom-built by Xiton Photonics for this experiment. In Fig. 3.3 a scheme of the cw-OPO is shown.

The OPO is pumped by a frequency-doubled Nd:YAG laser (Verdi V5 Coherent Inc.) with a maximum output power of 5 W. The pump beam at 532 nm wavelength is focused into the periodically poled lithium niobate crystal (PPLN) which is embedded in a bow-tie cavity. The optical amplification yields a signal wave at 980 nm and an idler wave at 1163 nm, fulfilling the quasi-phase-matching condition. In the resonator the idler wave oscillates and supports self-amplification, allowing for the extraction of roughly 4% of the idler beam. For a more stable performance of the system a rotatable etalon is introduced into the resonator – to prevent sudden resonator mode hops by a further reduction of permitted modes. The extracted laser beam has a bandwidth of $\Gamma_{\mathrm{las}} \leq 5$ MHz, as determined with a Fabry-Pérot interferometer, and at a pumping power of 2 W roughly 200 mW of infrared narrow-bandwidth light are provided.

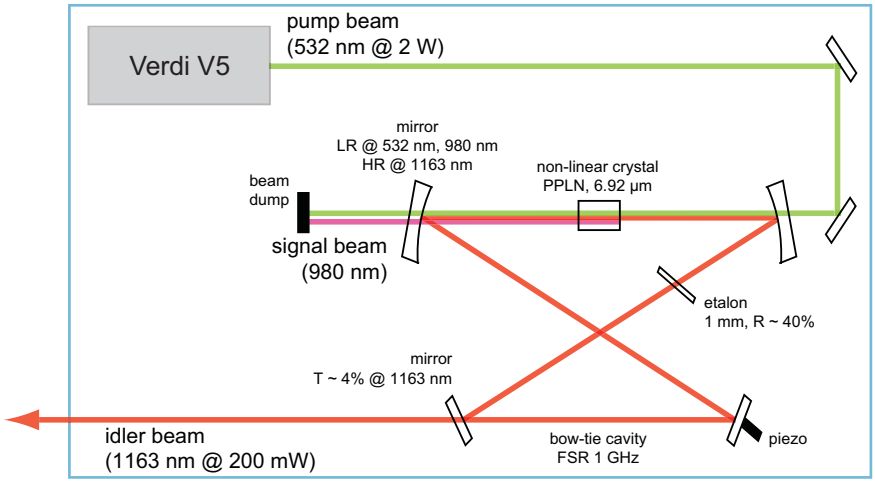

Fig. 3.3: Schematic view of the cw-OPO system

In order to tune the idler wavelength to a desired value, three distinct parameters must be adjusted:

1. Crystal temperature; a change in temperature shifts the gain profile of the optical amplification in the crystal (coarse tuning in the THz range);

2. Etalon angle; tilting the etalon results in a change of its transmission spectrum (tuning in the range of tens of GHz);

3. Resonator length; a change in length modifies the transmission spectrum of the resonator (fine tuning in the MHz range).

By iteratively optimizing these three parameters, it is possible to continuously change the wavelength in the range of 1140 nm to 1200 nm. There are only a few inaccessible regions in the emission spectrum, which cannot be reached by any combination of parameters. This phenomenon is not yet fully understood and currently under investigation [85].

A small fraction of the extracted laser light is guided into a wavemeter (HighFinesse Ultimate WSU-30 IR-PID), which determines and stabilizes the wavelength via a feedback loop with the OPO resonator. The wavemeter is calibrated with a stabilized diode laser. In turn the calibration laser is locked to the D_2 line in ^{6}Li (wavelength 670.977338 nm) via Doppler-free spectroscopy [86]. The absolute accuracy of 30 MHz of the wavemeter limits the final uncertainty of each absolute frequency measurement. Figure 3.4 shows a scan of the etalon angle at a fixed crystal temperature and fixed resonator length, resulting in a frequency sweep of 200 GHz.

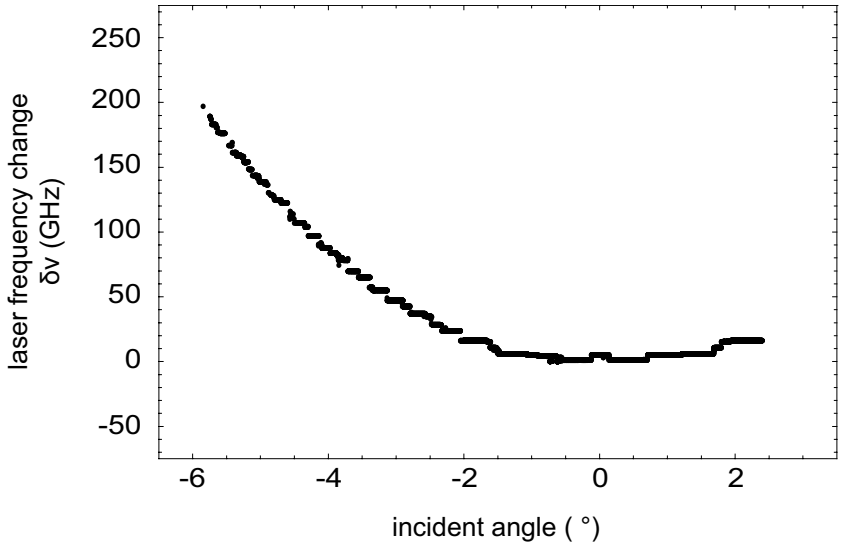

Fig. 3.4: Change in frequency of the idler wave as a function of the etalon angle at a fixed crystal temperature and fixed resonator length.

3.3 Spectrometer for In-Beam Laser Spectroscopy

Since the Os^- ion current and excitation cross-section were expected to be quite low, a suitable detection scheme for excited ions was required. A common technique for (positive) ion beam spectroscopy is the detection of fluorescence light. However, the long lifetime of the excited state with respect to reasonable observation times in an ion beam ruled out that method. In negative-ion experiments it is common to conduct photo-detachment studies to determine binding energies and to detect above-threshold resonances [28]. In the previous experiment on the negative osmium ion, it was also possible to detect a resonance below threshold, but with a two-step process [44]. As a first step, the ion was resonantly excited from the ground to the excited state. As a second step, another laser photon brought the valence electron from the excited state into the continuum. In order to achieve reasonable count rates for this subsequent two-photon process, a high-intensity laser source would be required. In [44] a pulsed laser system was used, which delivered 8 ns long pulses with a pulse energy of up to 3 mJ. Conversely, for precision spectroscopy a narrow-bandwidth and hence a continuous-wave laser is mandatory, limiting available intensities to a few hundred mW. For this reason it was decided to combine two existing experimental techniques to create a more efficient detection scheme: resonant laser excitation followed by electric-field detachment of the excited state, rendering the photo-detachment process obsolete. The technique of electric-field detachment was first conceived almost 50 years ago [87] and is still used for the detection of

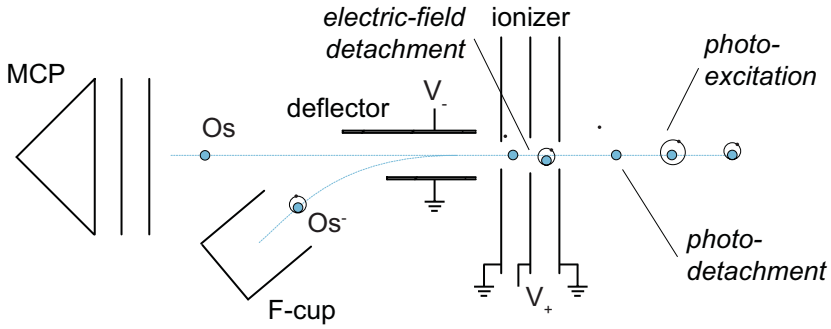

Fig. 3.5: Schematic view of the spectroscopy section, indicating possible mechanisms for electron detachment.

negative ions or Rydberg atoms. For a successful detachment by an electric field, field strengths of $\approx 10^6$ Vm^{-1} are necessary, cf. Sec. 2.1.3. Another important issue is the adequate separation of neutral particles from the remaining ions.

The spectroscopy section was designed to meet all of these requirements. It consists of a set of ionizing diaphragms (to promote the field-detachment), a deflector, a microchannel plate detector (MCP) and a Faraday cup. A cross-sectional schematic diagram of the spectrometer is shown in Fig. 3.5. In the ionizer the ion beam passes a longitudinal electric field. It is assembled as a sandwich of three electrically isolated stainless-steel apertures. Each has a diameter of 7.5 mm and is covered by a copper mesh. Together, all three layers have a transparency of roughly 70%. While the two outer apertures are grounded, the central aperature can be set from 0 up to $\pm$6.5 kV, creating a maximum electric field of $\approx 2 \times 10^6$ Vm^{-1}. The deflector consists of two parallel stainless-steel plates, while the shorter plate is grounded and its short length provides a pathway for the ions into the Faraday cup, as the longer plate is biased from 0 to 6.5 kV to produce an electric field perpendicular to the beam axis. During the ion-optical optimization procedure the appropriate deflection voltage is found by maximizing the ion current on the Faraday cup, which is very sensitive to the beam energy. In addition to the ion-optical optimization, the Faraday cup is used to monitor and record possible ion current fluctuations throughout each measurement. The MCP in the forward direction detects and counts the number of neutral particles. The detection efficiency is roughly 40% for a single neutral particle with an energy of a few keV [88].

The spectroscope was commissioned, installed and first successfully used for the measurements of the bound–bound transition in $^{192}Os^-$ described in Chap. 4. Furthermore its high overall sensitivity enabled the measurements of the corresponding transitions in high magnetic fields reported in Chap. 5.

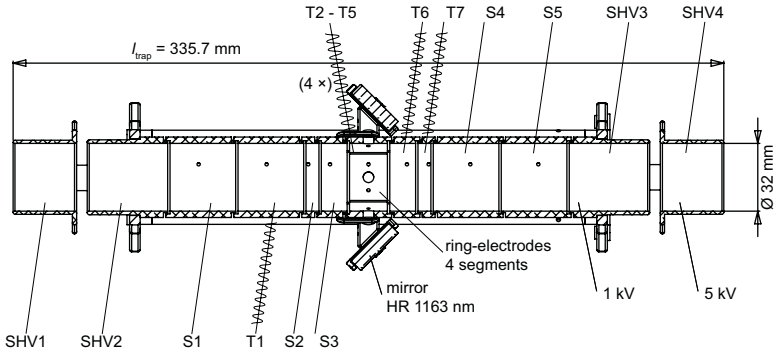

Fig. 3.6: Detailed sketch of the Penning trap.

3.4 Penning Trap

As mentioned in Sec. 2.2.1 several different types of ion traps are commonly used in experiments ranging from atomic to nuclear to particle physics. For the UNIC experiment the choice fell to a cylindrical Penning trap, in order to fulfill the requirements dictated by the projected physical and experimental restrictions:

1. Capturing ions with an initial kinetic energy of a few keV as well as electrons of some tens of eV;

2. Allowing for electron and heavy-ion diagnostics and manipulations;

3. Providing a radial laser beam access to the central trap region; and

4. Achieving a trap temperature for the ions of well below 300 K.

The importance of each individual requirement becomes obvious when recalling the intermediate steps necessary for accomplishing the UNIC project. The first, second and fourth requirement result from the planned pre-cooling of negative ions to cryogenic temperatures via collisional cooling with cold electrons, cf. Sec. 2.2.2. For the subsequent fluorescence spectroscopy of trapped negative ions and the final laser cooling procedure, the third requirement needs to be fulfilled. Of course, compromises had to be made in order to meet not only physical and experimental but also mechanical and constructive constraints.

In order to guarantee a large acceptance of ions, a cylindrical Penning trap with a large diameter was chosen. All 13 electrodes are made of gold-plated aluminum to minimize stray potentials and thereby enhance the achievable storage times in the trap. A sketch of the ion trap is shown in Fig. 3.6. The final design includes two high voltage end caps (up to ±5 kV DC). Both can be switched from 0 to 3 kV within 100 ns in order to trap and

	dimension (mm)	V_i/V_0	$\lvert V_{\max}\rvert$ (kV)
inner trap radius (r_{trap})	16	–	–
ring electrode (T2-T5)	17.9	1.00	0.1
1st correction (S3 & T6)	12.2	0.83	0.1
2nd correction (S2 & T7)	6.1	0.34	0.1
1st part end cap (T1 & S4)	31.0	0.00	0.1
2nd part end cap (S1 & S5)	31.0	0.00	0.1
1st stopping electrode (SHV2 & SHV3)	38.0	–	1.0
2nd stopping electrode (SHV1 & SHV4)	30.0	–	5.0

Table 3.1: Design values for trap dimensions and voltages. The electrode labels are those defined by the drawing in Fig. 3.6

eject an ion bunch. These switching times are possible with a commercially available solid state switch (Behlke GHTS 30 A). A second set of stopping electrodes is included in the trap setup and can be set from 0 up to ±1 kV. The inner electrodes can be separately biased (−100...100 V) to shape a desired trapping well. Since a well defined harmonic potential is mandatory for a precise plasma manipulation and diagnostics (see Sec. 2.2.1) the central trap region is carefully designed following the suggestions given in Ref. [89]. In that paper, the precise electrode lengths and the voltages required for production of a central harmonic potential are given. In our setup it was decided to use two correction electrodes and one split end cap on each side of the central ring electrode, resulting in eleven electrodes for the inner potential. The final design values for the lengths and appropriate voltages are listed in Table 3.1.

Prior to the final mechanical design of all elements the electrical potential on axis was simulated and the result is plotted in Fig. 3.7. In order to verify the quality of the harmonic potential, it was analyzed in terms of a polynomial expansion:

$$V(z) \approx \frac{V_0}{2}\left(\frac{C_2}{d^2}z^2 + \frac{C_4}{d^4}z^4 + ...\right), \tag{3.1}$$

where V_0 denotes the trap depth (applied voltage difference between the end cap and ring electrodes), d is a characteristic dimension of the trap and C_i are expansion coefficients, cf. Eq. (2.5). Note that the coefficients of the odd powers of z are all zero due to axial symmetry. In the inset of Fig. 3.7 a comparison of the simulated potential with the expansion is shown. By setting the C_2 coefficient to 1, a characteristic trap dimension of

$$d = 1.6 \cdot r_{\text{trap}}, \tag{3.2}$$

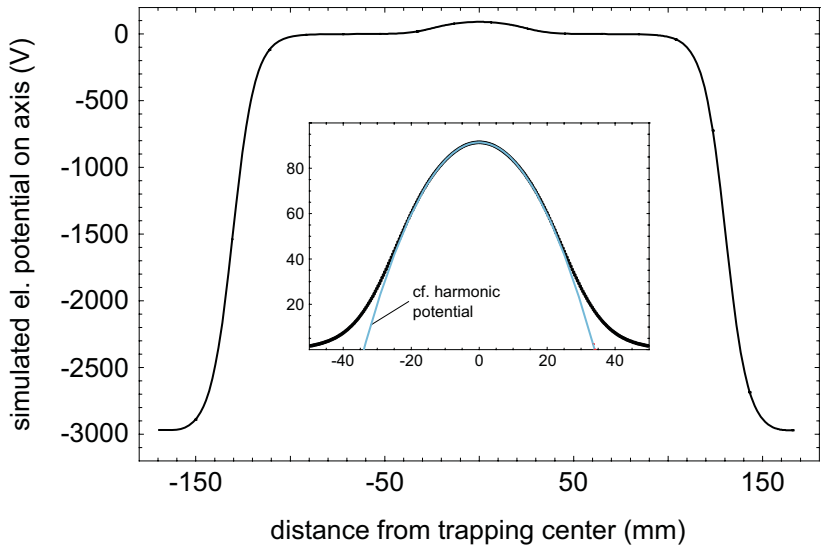

Fig. 3.7: Simulated electric potential along the symmetry axis of the trap. The HV end cap potential is sufficient to capture negative particles with an average energy of 2.5 keV or even higher. The inset shows a blow-up of the central trap region, where the simulated potential is compared with a purely harmonic potential.

is obtained, a result which will be of interest in Chap. 5. The octupole term, as the first order correction of a pure quadrupole potential, contributes to the potential with an expansion coefficient of $C_4 \approx 0.1$.

The ring electrode is additionally four-fold segmented and contains four radial apertures with a diameter of 4.5 mm, of which two are used for the laser beam access. The support structure for the electrodes also supports two highly reflective mirrors (coated for a high reflectivity at 1160 nm), which guide the laser beam radially through the central trapping region, cf. Fig. 3.6.

The whole ion trap is mounted on a CF-flange via four stainless steel tubes. This flange also contains all electrical feedthroughs for the electrode connection and two temperature sensors installed close to the central ring electrode. The trap is inserted into the superconducting solenoid from the downstream side. The solenoid magnet (Cryogenic Ltd.) is a liquid-cryogen-free superconducting magnet. Its cooling is provided by a cryocooler (Sumitomo compressor CSW71C and cryocooler SRDK-415) which delivers a cooling power of up to 1.5 W at 4 K and more than 27 W at its 40 K stage. The initial cooling down from room temperature to the operating temperature takes roughly 21 hours. The specifications of the magnet are listed in Table 3.2. A 3D illustration in Fig. 3.8 shows the trap inside the bore of the magnet and also indicates the corresponding temperatures on the relevant

magnet specification	
coil length	300 mm
cold bore inner diameter	150 mm
max. magnetic field	6 T
max. operating current	95 A
inductance	20 H
homogeneity	10^{-4}
persistent mode stability	$2 \cdot 10^{-5}$ h^{-1}

Table 3.2: Specifications of the 6-T magnet. Note: The homogeneity is given in a 20 mm diameter sphere volume (DSV) located in the center of the magnet.

sites – all temperatures are monitored and recorded via a computer interface at all times. The magnet shares its isolation vacuum with the experimental vacuum and therefore it is possible to thermally connect the trap electrodes to the cooling shield of the magnet, which has a temperature of ≈ 40 K. The available cooling power allows for the additional heat load introduced by the trap material, support structure, cabling and thermal radiation. In this way the trap electrodes, connected to the cooling shield by four chopper streaks (each 1 mm thick and 10 mm wide), are cooled down to $T_{\mathrm{trap}} \approx 65$ K, sufficient for the planned experiments.

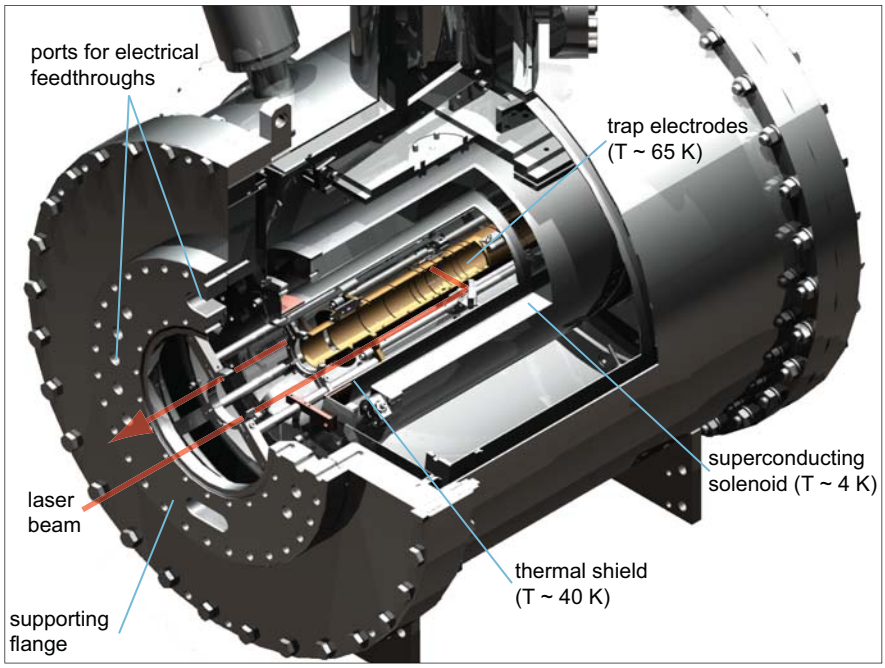

Fig. 3.8: 3D illustration of the Penning trap, mounted inside the superconducting magnet. The available transverse laser beam pathway is shown and the different temperature regions are indicated.

4. COLLINEAR LASER SPECTROSCOPY

The experiments reported in this chapter were conducted in a collinear configuration. This has the following advantages:

- Increased interaction time with the ion beam, compared to a transverse configuration. A longer interaction time of the ion beam with the laser light, in contrast to a transverse setup. A long interaction time is desired since the magnitude of the relevant cross-section for the laser excitation is expected to be rather low [44].

- Reduction of Doppler broadening. The effect of velocity bunching, which is a well-known advantage of collinear spectroscopy, reduces the Doppler width of a transitions (see for example [90]) and thereby leads to a more precise determination of the resonance frequency. For typical operating parameters (ion temperature $T \approx 1500$ K and acceleration voltage 5 kV) a reduction of about a factor ten with respect to the transverse case can be achieved.

A schematic diagram of the experimental setup is shown in Fig. 4.1. The mass-separated ion beam is bent into the laser spectroscopy setup by an electrostatic bender. The interaction region is delimited by the entrance diaphragm (diameter 7.5 mm) and the ionizer (cf. Sec. 3.3). In the interaction region (length 520 mm), the laser beam, which is parallel to the ion beam, is superposed on it before the ions enter the spectrometer section, whose principle is described in Sec. 3.3. The MCP can be moved into and out of the beam axis. In this way, the collimated laser beam (≈ 1 mm di-

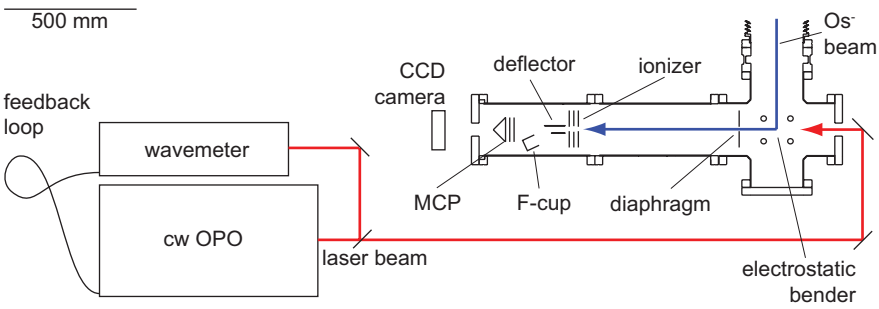

Fig. 4.1: Sketch of the experimental setup for the collinear laser spectroscopy.

ameter) can be projected through the entire spectrometer arm and aligned with the help of a CCD camera (DAT-TaperCamD) behind the MCP.

First, the most abundant isotope (^{192}Os) is investigated. The transition frequency of the $^4\mathrm{F}_{9/2}$ to $^6D_{J_{\mathrm{e1}}}$ transition and the corresponding cross-section are of particular interest. The main results of these measurements have been previously published [91]. In Sec. 4.1 a more detailed account of the high-resolution spectroscopy of $^{192}\mathrm{Os}^-$ is given, especially concerning the relevant systematic effects. Furthermore, the E1 transition of all other naturally abundant isotopes was studied. The hyperfine splitting of the odd-A isotopes is used to determine the total angular momentum $^6D_{J_{\mathrm{e1}}}$ of the excited state (Sec. 4.2).

4.1 High-Precision Spectroscopy on $^{192}Os^-$

4.1.1 Transition Frequency

During data taking for a precision measurement, the laser frequency is tuned around the resonance in the shape of triangular scans. Typically a range of 100 to 200 MHz is scanned, while the number of neutralized negative osmium ions is recorded. If an ion in the interaction zone is excited, it is detached by the electric field of the ionizer. Furthermore the excited state may be detached by other competing mechanisms as discussed in Sec. 2.1.3. In any case the neutral atoms are detected by the MCP. Other contaminant ions, e.g., $^{190}\mathrm{OsH}^-$ or $^{192}\mathrm{OsH}^-$, are always guided in the direction of the Faraday cup and can only contribute to a higher background level on the MCP. In order to suppress this or other background events, a chopper is introduced into the laser pathway, which is operated at a frequency of typically 250 Hz. The data acquisition system records both the detector background, which is measured when the laser light is blocked by the chopper wheel, and the signal, when the laser light traverses the interaction region. In a later step the background events are subtracted from the signal, resulting in an enhanced signal-to-noise ratio. Figure 4.2 shows a typical resonance spectrum obtained at a beam energy of 5 keV. This spectrum clearly shows the enhancement due to the electric-field detachment process in the ionizer. The width (FWHM) of the resonance peak $\Gamma_{\mathrm{res}} = 45$ MHz is dominated by the Doppler width of the negative ion beam, and its shape is compatible with a Gaussian line profile except for an asymmetry at high frequencies, which can be attributed to a corresponding asymmetry in the velocity distribution of the ions. This systematic effect contributes an uncertainty of 5 MHz to the determination of the central frequency.

Another systematic effect has to be considered in this experiment: In a collinear setup with co-propagating beams all absorbed photon frequencies are blue-shifted with respect to the rest frame of the atoms. Thus data points at different beam energies are taken (see Fig. 4.3) to extract the rest

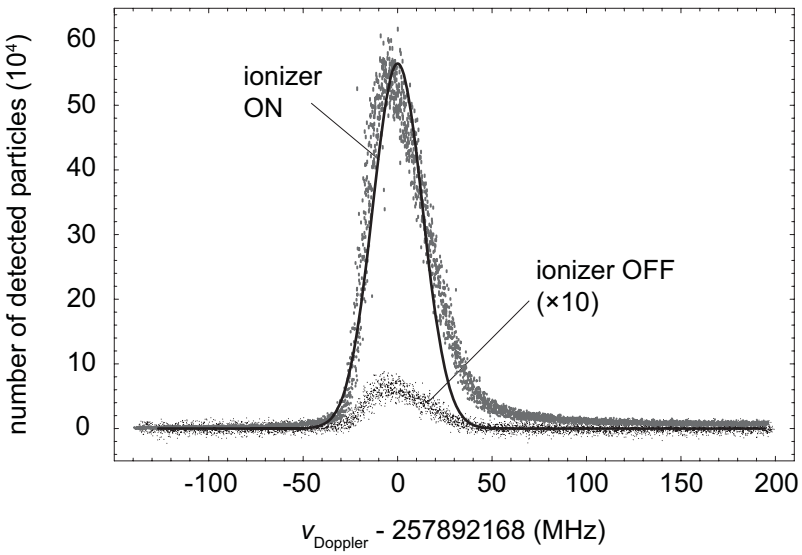

Fig. 4.2: Typical resonance spectrum of the $^4F_{9/2}$ to $^6D_{J_{e1}}$ transition at an ion beam energy of 5 keV. It illustrates the efficiency gain due to the field-detachment process in comparison to all competing detachment mechanisms. The corresponding Gaussian fit of the data is drawn as a solid curve.

frame resonance frequency from a fit to the data with the function for the Doppler shift:

$$\nu = \nu_0 \sqrt{\frac{c+v}{c-v}}, \tag{4.1}$$

where the velocity $v = \sqrt{2(E+\Delta E)/M}$ is a function of the beam energy $(E + \Delta E)$. In addition to the un-shifted transition frequency ν_0, a constant offset of the beam energy ΔE was introduced into the fit, in order to account for a a possible offset in the energy. For this parameter a fit value of $\Delta E = 0.4(5)$ eV indicated that further consideration was not necessary. The overall quality of the fit is demonstrated by the plotted residuals in Fig. 4.3(c). The final result for the resonance frequency $\nu_0 = 257.831190(35)$ THz is in agreement with the previous experimental value of 257.8341(46) THz [44], with a deviation of 0.6 σ.

4.1.2 Cross Section

For the determination of the excitation cross-section, it is useful to consider the time evolution of the ground and excited state populations in the laser field, as well as the evolution of the number of neutralized atoms. In order to describe the combined processes of photo-excitation and electric-field detachment of the excited state, while also taking into account the

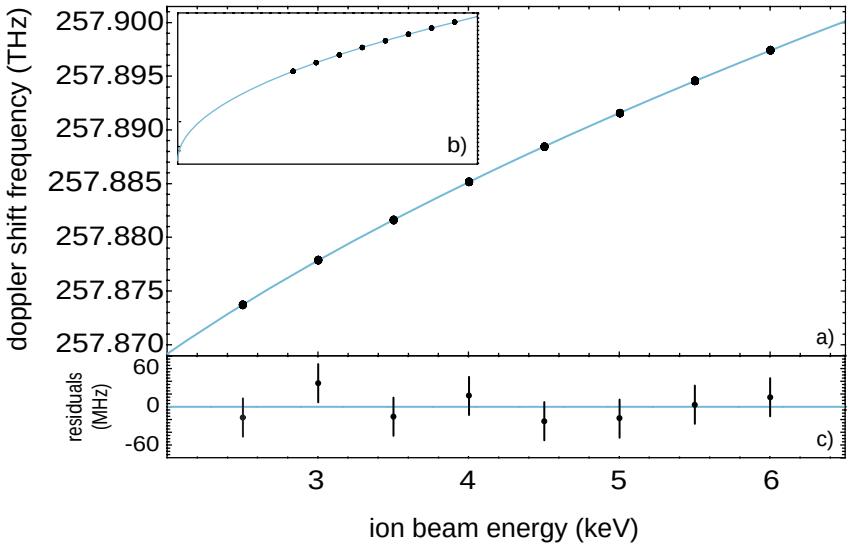

Fig. 4.3: a) Measured blue-shifted central frequencies of the resonance as a function of the ion beam energy. The error bars are too small to be visible. The solid curve represents the resulting fit for the Doppler shift, from which the rest frame frequency is extracted. b) For illustration the function is shown over the entire energy range (without explicit scales). c) Residuals are shown to illustrate the quality of the fit.

sequential two-photon detachment, a system of standard rate equations is introduced [92]:

$$\frac{dN_{\mathrm{g}}(t)}{dt} = -\sigma_0\phi N_{\mathrm{g}}(t) + (\sigma_0\phi + \tau_0^{-1})N_{\mathrm{e}}(t) \tag{4.2a}$$

$$\frac{dN_{\mathrm{e}}(t)}{dt} = \sigma_0\phi N_{\mathrm{g}}(t) - [(\sigma_0 + \sigma_{\mathrm{d}})\phi + \tau_0^{-1} + \tau_{\mathrm{loss}}^{-1}]N_{\mathrm{e}}(t) \tag{4.2b}$$

$$\frac{dN_{\mathrm{d}}(t)}{dt} = (\sigma_{\mathrm{d}}\phi + \tau_{\mathrm{loss}}^{-1})N_{\mathrm{e}}(t), \tag{4.2c}$$

where N_{g} and N_{e} are the ground and excited state (later field-detached) populations and N_{d} is the number of detached atoms, respectively. The parameter τ_0 denotes the lifetime of the excited ($^6D_{J_{\mathrm{e}1}}$) state decaying to the ground ($^4F_{9/2}$) state via spontaneous photon emission. The lifetime is connected to the cross-section σ_0 by the relation

$$\tau = c^2/(4\pi^2\sigma_0\nu_0^2\Gamma_{\mathrm{res}}). \tag{4.3}$$

Furthermore, τ_{loss} denotes the lifetime of the excited state with respect to all possible detachment processes other than absorption of a second laser photon, and ϕ is the laser photon flux. In this model a possible decay into the intermediate ($J = 7/2$ and $5/2$) states is neglected because the partial lifetimes, which scale as ν^{-3}, are expected to be approximately 10 times longer for those channels.

The set of differential equations (4.2a)–(4.2c) can be solved analytically. In a next step, the populations $N_{\mathrm{e}}(t)$ and $N_{\mathrm{d}}(t)$ (where $t = 0$ at the time the ions enter the laser field) are expressed as a function of the photon flux ϕ. In addition, the photon flux is modeled to have a spatial Gaussian beam profile, in line with the observations from the beam profile CCD camera. In Fig. 4.4 the calculated time evolution of each state is presented for different laser powers and therefore different laser intensities, while all other parameters are kept fixed. Here the black/solid line indicates the evolution of the ground and the blue/dashed line that of the excited state population. The red/dotted line represents the fraction of photo-detached ions, which are already detached prior to the electric-field detachment in the ionizer. In the following, it is assumed that the efficiency for detaching Os^- in the $^6D_{J\mathrm{e}1}$ state in the electric-field ionizer is 100%. Finally, the total number of neutralized particles $N_{\mathrm{neut}}(\sigma_0, \sigma_{\mathrm{d}}, \tau_{\mathrm{loss}}, N_0, P_{\mathrm{las}}) = N_{\mathrm{e}}(t) + N_{\mathrm{d}}(t)$ is a function of the average laser power and has four independent parameters: The resonant and non-resonant cross-sections σ_0 and σ_{d}, the number of ions within the overlap region N_0 and the lifetime τ_{loss}. The latter was held fixed at the estimated BBR detachment rate, which was calculated to be ≈ 10 ms for a surrounding temperature of 300 K, cf. Sec. 2.1.3. The resulting cross-sections σ_0 and σ_{d} are unaffected by this additional detachment channel even when allowing for detachment rates ($1/\tau_{\mathrm{loss}}$) up to about a factor of

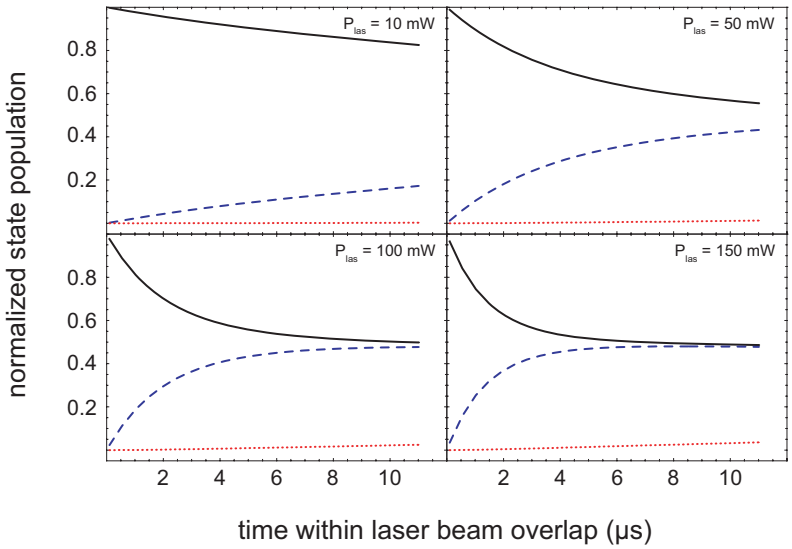

Fig. 4.4: The time evolution for different laser powers of the ground (black/solid) and excited state (blue/dashed) population in the beam and the fraction of neutral atoms (red/dotted) is displayed. The graphs are obtained from the solution of the rate equations.

50 higher than estimated. It should be pointed out that in this analysis a precise knowledge of the MCP detection efficiency is not necessary, provided it is constant during the course of the measurement. The function N_{neut} is very sensitive to σ_0, the main parameter of interest, and to N_0, the asymptotic value of N_{neut} at a high laser powers.

The measurements were conducted in the following way. The total number of neutralized atoms (detected on the MCP) was recorded for beam energies ranging from 2.5 keV to 5.5 keV as a function of the laser intensity, which was varied via a polarizing beam splitter from 0 to 160 mW without changing other laser beam characteristics. Figure 4.5 shows a typical result of such a measurement at a beam energy of $E = 2.5$ keV, along with a fit according to the rate equation model (solid line). Ion-optical simulations with SIMION$^{\mathrm{TM}}$ have shown that the beam divergence between the diaphragms is $\approx 1.5°$, effectively reducing the interaction volume by 30%, without any other consequences for the parameteres obtained from the fit. The weighted mean of 10 such measurements yields a final value of $\sigma_0 = 2.5(7)\times10^{-15}$ cm^2, where the uncertainty includes a contribution which is equal in magnitude to the beam divergence correction. Furthermore, great care was taken to exclude other effects which could mimic the asymptotic behavior of the data. In particular MCP saturaton cannot be ruled out completely and unfortunatly such an effect would make the cross-section appear larger than the true value. The fit result does not constrain the photo-detachment cross-section

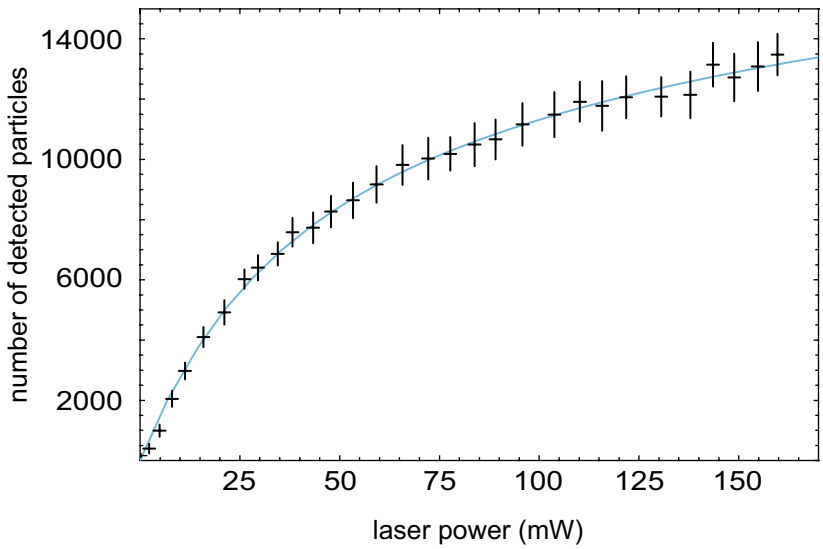

Fig. 4.5: Number of detected atoms vs. laser intensity at the resonance frequency ν_0 at a fixed ion beam energy of $E = 2.5$ keV. The solid curve is a fit to the data according to Eqs. (4.2a)–(4.2c), which yields the cross-section σ_0 for the transition.

very well, and only a rough estimate of $\sigma_\mathrm{d} \approx 10^{-17}$ cm^2 was obtained, in line with the expected value for a non-resonant process and the estimation given in Ref. [44]. As pointed out above, the partial lifetime for decay into the ground state by spontaneous emission can be deduced from the cross-section via Eq. (4.3). In this way, using $\Gamma_\mathrm{res} = 45$ MHz, which represents the experimental width of the resonance, a value of $\tau_0 = 3(1)$ ms is obtained from the fit result for the value of σ_0.

The corresponding Einstein A coefficient is ≈ 330 s^{-1}, confirming that the resonance is due to an electric-dipole transition, although the Einstein coefficient is at the lower end of the scale for E1 transitions. This is however not unusual for a spin-forbidden resonance. The measurements discussed here indicate that the natural line width is even narrower than suggested by the result of Bilodeau and Haugen, who found $A \approx 10^4$ s^{-1} [44]. The profound consequences of the results obtained in this section are discussed in the summarizing Chap. 6, which is deals with the further prospects of laser cooling.

4.2 Measurements on Other Isotopes of Os

Since two out of the seven naturally abundant isotopes, ^{187}Os and ^{189}Os, have a non-vanishing nuclear spin, the presence of hyperfine structure (HFS) is expected in the corresponding laser spectra. The HFS is of special interest

isotope	isotope mass (amu)	natural abundance %	measured frequency ν_0 (THz)
$^{192}Os^-$	191.9614807(27)	40.78(19)	257.831190(35)
$^{190}Os^-$	189.9584470(16)	26.26(2)	257.830296(35)
$^{189}Os^-$	188.9581475(16)	16.15(5)	257.829613(35)
$^{188}Os^-$	187.9558382(15)	13.24(8)	257.829282(35)
$^{187}Os^-$	186.9557505(15)	1.96(2)	257.828422(35)
$^{186}Os^-$	185.9538382(15)	1.59(3)	257.828068(35)
$^{184}Os^-$	183.9524891(14)	0.02(1)	257.826880(35)

Table 4.1: Complete list of all stable isotopes showing the masses [93], the natural abundances [94] and the measured resonance frequencies of the investigated E1 transition (in the rest frame). For the odd isotopes with non-vanishing nuclear spin the center-of-gravity of the hyperfine splitting is given.

in the context of this project, as it contains valuable information about the electronic level structure of the negative osmium ion and can thus reveal the so far unknown total angular momentum J_{e1} of the excited state. Another expected effect is the isotope shift (IS), which results from the finite mass and the finite volume of the nucleus.

All measurements are carried out in the same way described in Sec. 4.1.1. For each isotope the magnetic field of the mass separator is chosen such that the ion current of the corresponding mass on the last Faraday-cup (at the end of the spectrometer section, cf. Fig. 4.1) is maximal, while simultaneously optimizing the other ion-optical devices. Only for $^{184}Os^-$ this procedure turns out not to be applicable. Due to its low abundance of only 0.02%, it is not possible to observe its presences in the ion mass-spectrum with this setup (cf. the mass spectrum shown in the inset of Fig. 3.2). Hence the value of the magnetic field is extrapolated from the heavier isotopes to $A = 184$, thereby permitting a measurement of the laser spectrum of $^{184}Os^-$.

Table 4.1 gives an overview of the masses of the relevant isotopes, their naturally abundance and their determined center frequencies (in the rest frame) for the $^4F_{9/2}$ to $^6D_{J_{e1}}$ transition. For the isotopes with even mass numbers the laser spectra are fitted with a single Gaussian profile. Their observed widths of $\Gamma_{\mathrm{res}} \approx 45$ MHz are in agreement with the corresponding width in $^{192}Os^-$ (cf. Sec. 4.1.1). The fitting routine for the odd isotopes is explained in more detail in Sec. 4.2.2, since considerations concerning the HFS are needed to evaluate the multiple peak structure. For these ions, the center-of-gravity of each spectrum is extracted and listed in the table. The correction for the blue shift due to the Doppler effect is done by comparing the transition frequencies with that in $^{192}Os^-$. Since the reference transition yields a precise determination of the ion beam energy, a transformation of all

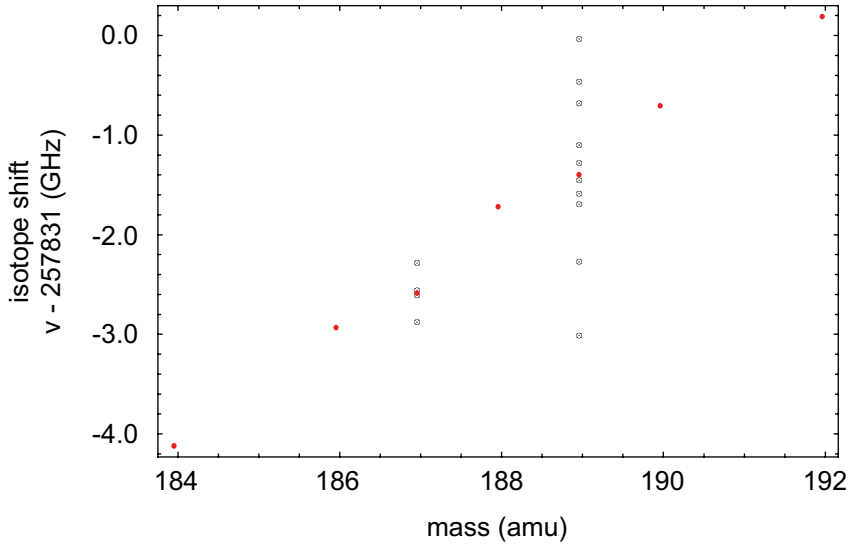

Fig. 4.6: Measured E1 transition for all stable osmium isotopes (red dots). For the odd isotopes the non-vanishing nuclear spin results in hyperfine splitting (black dots) the corresponding center-of-gravity of these lines are also shown (red dots).

spectra into the rest frame is achieved in this way. The rest frame frequency shifts, calculated relative to the reference frequency of $^{192}Os^{-}$, are plotted in Fig. 4.6. The graph demonstrates a strong dependence of the frequency shift on the isotopic mass which is approximately linear.

4.2.1 Isotope Effect

Background on Isotope Shift

The phenomenon of isotopic shifts in atomic systems – meaning the change of transition frequencies in different isotopes of the same element – can be traced back to two distinct origins (see for example [95, 96]):

- The so called mass shift (MS), a result of the change in mass, which is dominant for light elements ($Z < 30$);
- The so called field shift (FS), a consequence of the change in nuclear volume, which is dominant for heavy elements ($Z > 58$).

Thus the isotope shift between two isotopes A and A' for a given transition can be written to good approximation as a sum of those two contributions:

$$\delta\nu^{AA'} = \delta\nu^{AA'}_{\mathrm{MS}} + \delta\nu^{AA'}_{\mathrm{FS}}. \tag{4.4}$$

The mass shift is in turn divided into two parts: first, the normal mass shift (NMS) and second, the specific mass shift (SMS):

$$\begin{aligned}\delta\nu_{\mathrm{MS}}^{AA'} &= \delta\nu_{\mathrm{NMS}}^{AA'} + \delta\nu_{\mathrm{SMS}}^{AA'} \\ &= (M_{\mathrm{NMS}} + M_{\mathrm{SMS}})\frac{A'-A}{AA'},\end{aligned} \tag{4.5}$$

both proportional to the same purely nuclear factor, a function of the mass numbers A and A' of the corresponding isotopes with $A' > A$. In contrast to the factor M_{SMS} for the specific mass shift – which depends on the electronic wavefunction of the participating states, cf. Ref. [95] –, the factor M_{NMS} for the normal mass shift can be calculated from the following relation:

$$M_{\mathrm{NMS}} = \nu_0 \frac{M_{\mathrm{e}}}{M_{\mathrm{u}}}, \tag{4.6}$$

where ν_0 denotes the transition frequency, and M_{e} and M_{u} are the electron mass and the relevant atomic mass. The origin of the NMS lies in the reduced mass correction for the electron motion inside the atom.

The second term in Eq. (4.4) represents the field shift and can again be written as a product of a purely nuclear and a purely electronic term:

$$\delta\nu_{\mathrm{FS}}^{AA'} = F\delta\left\langle r^2\right\rangle^{AA'}. \tag{4.7}$$

Here the factor $\delta\left\langle r^2\right\rangle^{AA'}$ is the change in mean square nuclear radii of the corresponding isotopes and the electronic factor F is proportional to the difference of the total non-relativistic electron charge density at the site of the nucleus $\Delta\left|\Psi(r=0)\right|_i^2$.

Both M_{SMS} and F depend strongly on the details of the electron wave function and are thereby not trivial to calculate. However, they can be deduced from the experimental data recorded in the present measurements.

Analysis

In order to obtain the values of the parameters M_{SMS} and F, a subtraction of the NMS from the total isotope shift is necessary and yields to the so-called residual isotope shift (RIS):

$$\delta\nu_{\mathrm{RIS}}^{AA'} = M_{\mathrm{SMS}}\frac{A'-A}{AA'} + F\delta\left\langle r^2\right\rangle^{AA'}. \tag{4.8}$$

After transposing with the numeric factor the following linear equation is obtained:

$$\delta\nu_{\mathrm{RIS}}^{AA'}\frac{AA'}{A'-A} = M_{\mathrm{SMS}} + F\left(\delta\left\langle r^2\right\rangle^{AA'}\frac{AA'}{A'-A}\right). \tag{4.9}$$

A	$\delta\nu_{\mathrm{RIS}}^{A,192}$ (MHz)	$\delta\langle r^2\rangle^{A,192}$ (fm^2)
190	−887(15)	−0.063(6)
189	−1576(15)	−0.111(11)
188	−1892(15)	−0.134(10)
187	−2757(15)	−0.191(14)
186	−3098(15)	−0.215(13)
184	−4278(15)	−0.298(17)

Table 4.2: Experimental residual isotope shifts of Os isotopes (from this work) and changes in nuclear charge radii (taken from Ref. [97]).

M_{NMS} (GHz amu)	M_{SMS} (THz amu)	F (GHz/fm^2)
141.4	2(13)	16(10)

Table 4.3: Calculated normal mass shift M_{NMS}, specific mass shift M_{SMS} and field shift coefficient F for the E1 transition in negative osmium, derived from the linear fit shown in Fig. 4.7.

A linear regression fit allows the determination of M_{SMS} and F, assuming that the changes in mean square radii $\delta\left\langle r^2\right\rangle^{AA'}$ are known for the different isotopes. Summary tables of experimental values can be found in Ref. [97].

The experimentally determined residual isotope shifts are listed in Table 4.2, together with the values from the literature for the changes in mean square nuclear radii. All values were calculated $^{192}\mathrm{Os}^-$ ($A' = 192$) as the reference isotope. The values of Table 4.2 are also plotted in Fig. 4.7. In the graph, a weighted linear regression fit (solid line) to the data points is shown. The fit delivers the values for the SMS and the FS coefficients, the two free parameters in Eq. (4.9). Table 4.3 summarizes the results and it also gives the calculated value for the NMS, cf. Eq. (4.6). The main source of uncertainty in these values is the fairly large uncertainty in the published values of $\delta\langle r^2\rangle^{A,192}$. The largest contribution to the total isotope shift is due to the field shift, as is expected even from the simple model developed in the beginning of this section.

4.2.2 Hyperfine Structure

Two isotopes have a non-vanishing nuclear spin – $I = 1/2$ for ^{187}Os and $I = 3/2$ for ^{189}Os – resulting in a HFS which is characterized by the total angular momentum $\vec{F} = \vec{J} + \vec{I}$. As we see in the following, an analysis of the observed hyperfine splitting can reveal the so far unknown total angular momentum J_{e1} of the excited bound state. By recalling the selection rules

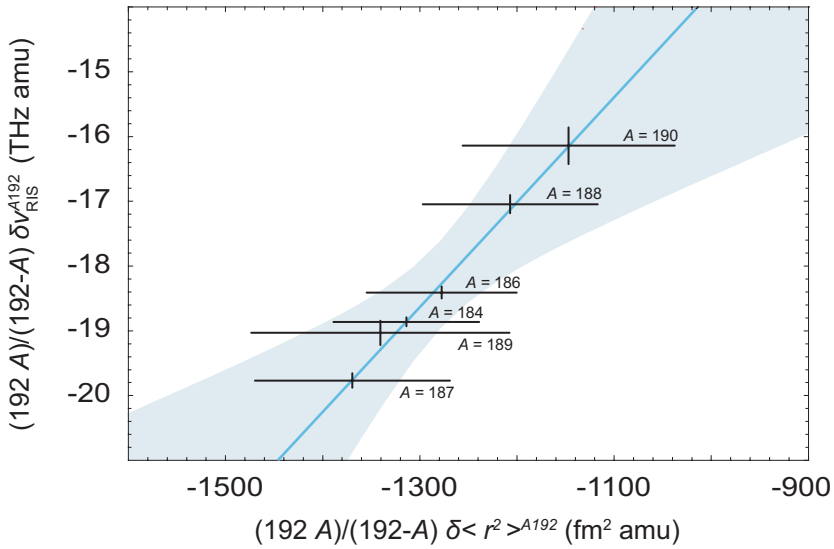

Fig. 4.7: Experimental residual isotope shifts as a function of the change in nuclear mean square radii. The line represents a weighted linear regression fit of the data and the shade indicates its confidence level.

and counting the number of transitions visible in the spectra of $^{187}Os^-$ and $^{189}Os^-$ it is possible to deduce J_{e1}. The recorded spectra for these two isotopes are displayed in Fig. 4.8. Since we observe four transitions in the case of $^{187}Os^-$ and ten for $^{189}Os^-$, it follows from the selection rule for the total angular momentum, $\Delta F = 0, \pm 1$, that the angular momentum must be $J_{e1} = 9/2$. Hence, the two other potential values 7/2 and 11/2 are ruled out.

A more detailed analysis of the hyperfine spectra allows the determination of the magnetic dipole constant A and the electric quadrupole constant B, as defined in the Casimir formula, which describes the energy shift ΔE_{HFS} for a specific energy state:

$$\Delta E_{\mathrm{HFS}} = A\frac{C}{2} + B\frac{\frac{3}{4}C(C+1) - I(I+1)J(J+1)}{2I(2I-1)J(2J-1)}, \tag{4.10}$$

where

$$C = F(F+1) - I(I+1) - J(J+1). \tag{4.11}$$

In particular, the energy level is specified by its quantum numbers J and F, and the corresponding energy shift is due to the interaction of the electron's angular momentum $\vec{J}$ with the nuclear spin $\vec{I}$.

The magnetic dipole coupling results from the interaction of the nuclear magnetic moment with the magnetic field induced by the bound electrons.

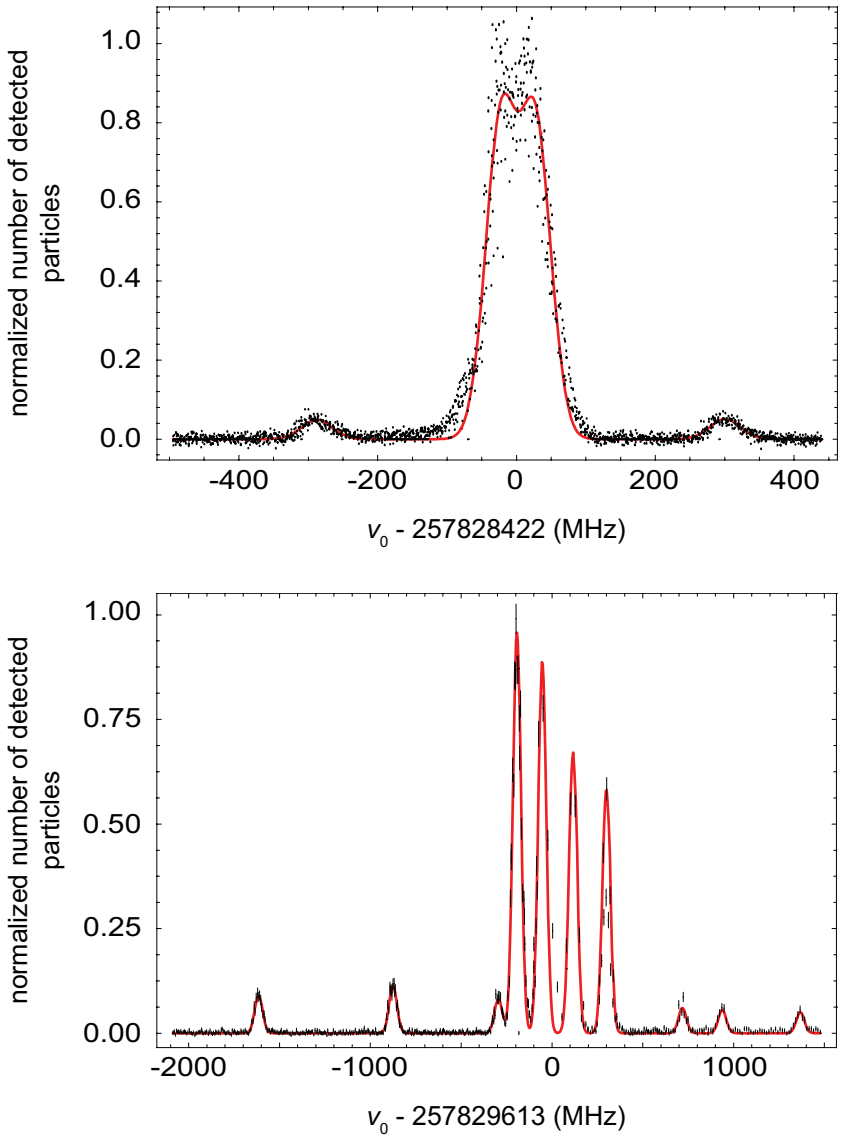

Fig. 4.8: Measured hyperfine splitting of $^{187}Os^-$ (top) and $^{189}Os^-$ (bottom) and resulting fit of the data (red/solid).

The magnetic-dipole constant is defined by

$$A \equiv \mu_{\mathrm{I}} \frac{\bar{H}(0)}{IJ}, \tag{4.12}$$

where μ_{I} is the dipole moment of the nucleus, in units of the nuclear magneton $\mu_{\mathrm{N}} = e\hbar/(2M_{\mathrm{p}})$, and $\bar{H}(0)$ is the average magnetic field induced by the electrons orbiting the nucleus.

The lowest-order electric contribution to the HFS results from the electric quadrupole coupling, which is a consequence of the nuclear electric quadrupole moment interacting with the electric field produced by the electrons. Its coupling constant is defined in the following manner:

$$B \equiv eQ\bar{\Psi}_{\mathrm{JJ}}(0), \tag{4.13}$$

here e is the electron charge, Q denotes the electric quadrupole moment of the nucleus and $\bar{\Psi}_{\mathrm{JJ}}(0)$ represents the vector gradient of the electric field which is produced by the electron cloud at the site of the nucleus. Note: A permanent nuclear electric dipole moment has so far not been observed and is under investigation in recent research activities, see for example Ref. [98].

For the extraction of the A and B constants of the ground and excited states from the experimental spectra, the data are fitted to Eq. (4.10) with a simple fitting routine. The fitting function consists of a sum of Gaussian peaks – the number is fixed by the quoted selection rule – and their relative distance depends on the values of A and B of the ground and excited state. Each peak represents an allowed transition, as illustrated in the energy level diagram shown in Fig. 4.9. Their intensities, the widths of the individual peaks, and the center-of-gravity frequency of the entire spectrum are other parameters of the fit. The peak widths are fixed at 45 MHz by the observed line widths of the isotopes without HFS. Furthermore the relative intensities for each line can be calculated using the formula given in Ref. [99], stating that the sum of the strengths of the lines belonging to the same ground state is proportional to its statistical weight, and that the sum of strengths of the lines ending in the same excited state is also proportional to its corresponding statistical weight. The complete intensity formulas were first derived by Kronig [100], Sommerfeld and Hönl [101], and Russell [102] based on the correspondence principle, and quantum-mechanically by Dirac [103].

This leaves a total of six independent parameters in the fitting routine: the absolute intensity, the center-of-gravity frequency (of interest for the isotope effect), and the values for A and for B both for the ground and the excited state. For ^{187}Os the two B values are zero, since a nucleus with a nuclear spin $I = 1/2$ has a spherical charge distribution and therefore no electric quadrupole moment. Unfortunately, due to the experimental spectra (only), two sets of solutions for the ground and excited state A and B coupling constants are possible. However, using the published values for A

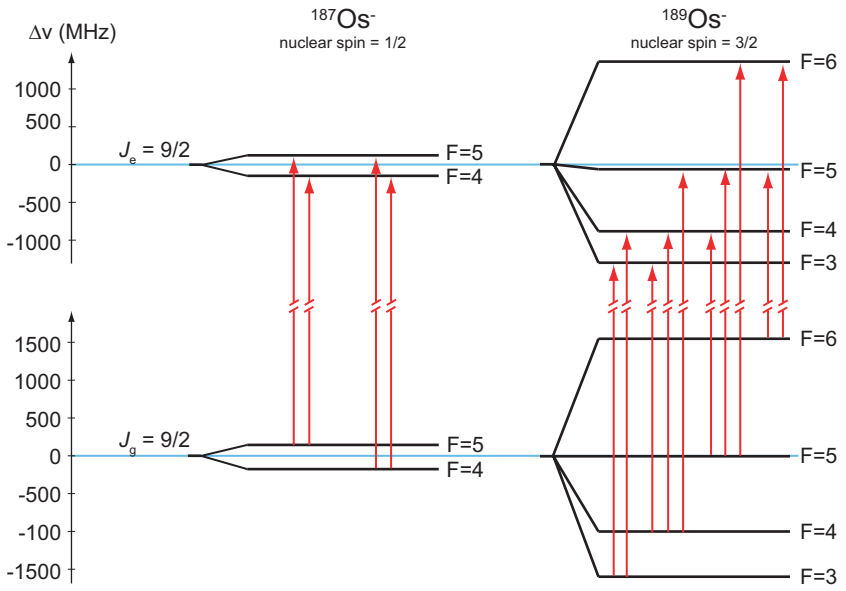

Fig. 4.9: Energy level diagram for ^{187}Os$^-$ and ^{189}Os$^-$ including their hyperfine levels. The arrows indicate allowed E1 transitions.

and B for the ground state of ^{189}Os$^-$ from Ref. [45], we can assume that the signs of these parameters should all be positive. This rules out one possible set of solutions and leads to our final experimental values displayed in Table 4.4. The theoretical and experimental values are in surprisingly good agreement, considering that the calculations can only be made numerically and the electron–electron correlation effects are not simple to treat [105].

The values for A in ^{187}Os$^-$ and ^{189}Os$^-$ represent redundant information, since they are connected via the ratio of the magnetic dipole moments of

isotope	state	A_{exp} (MHz)	B_{exp} (MHz)	A_{lit} (MHz)	B_{lit} (MHz)
^{189}Os	$^4F_{9/2}$	215(2)	399(4)	214; 386	420; 381
	$^6D_{9/2}$	184(2)	481(4)	–	–
^{187}Os	$^4F_{9/2}$	64(2)	–	–	–
	$^6D_{9/2}$	54(2)	–	–	–

Table 4.4: Hyperfine structure constants obtained by fitting our experimental data to Eq. (4.10). The literature values are theoretical values from [45] derived by two different methods. For ^{187}Os$^-$, $\mu_{\mathrm{I}}/\mu_{\mathrm{N}} = 0.06465184(6)$ and $I = 1/2$, and for ^{189}Os$^-$, $\mu_{\mathrm{I}}/\mu_{\mathrm{N}} = 0.659933(4)$, $I = 3/2$ and $Q = 0.91(10) \times 10^{-24}$ cm^2 all from Ref. [104].

$R^{\mathrm{g}}_{\mathrm{exp}}$	$R^{\mathrm{e}}_{\mathrm{exp}}$	R_{lit}
0.297(10)	0.294(11)	0.293902(2)

Table 4.5: Comparison of experimental A value ratios with the value based on literature – derived from the magnetic dipole moments ratio.

each individual nucleus, cf. Eq. (4.12):

$$\frac{A(^{187}\mathrm{Os})}{A(^{189}\mathrm{Os})} = \frac{\mu_{\mathrm{I}}(^{187}\mathrm{Os})}{\mu_{\mathrm{I}}(^{189}\mathrm{Os})} \frac{I(^{189}\mathrm{Os})}{I(^{187}\mathrm{Os})} \tag{4.14}$$

Thus the quality of the experimental values of A can be checked independently from the theoretical calculations, by comparing the published values of the ratio of the magnetic dipole moments and nuclear spins (R_{lit}) with the experimental values from the individual A parameters. For the ground states this ratio is denoted by $R^{\mathrm{g}}_{\mathrm{exp}}$ and for the excited states $R^{\mathrm{e}}_{\mathrm{exp}}$. The values are displayed in Table 4.5. In this systematic check, our experimental values are in good agreement with the more accurate value from the literature.

For laser spectroscopy in high-magnetic fields, which is presented in the next chapter, it is crucial to know the number and corresponding quantum numbers of Zeeman sub-levels, as provided by these results. Furthermore, they have important implications for the prospect of laser cooling, which is discussed in Chap. 6.

5. EXPERIMENTS IN AN EXTERNAL MAGNETIC FIELD

5.1 Zeeman Splitting of $^{192}Os^-$

In order to develop a suitable laser-cooling scheme for negative osmium ions in an electromagnetic ion trap, a knowledge of the ionic spectra in an external magnetic field is required. In magnetic fields of a few T, which are necessary to confine the ions effectively for long times, the line splitting due to the Zeeman effect is of the order of a few tens of GHz. The knowledge of each transition frequency and its corresponding strength is crucial for the development of a feasible laser-cooling scheme for Os^-.

Expected Zeeman Splitting – Semi-Classical Estimate

The line splitting in an external magnetic field results from the coupling of the magnetic moment of the atom or ion with an external magnetic field $\vec{B}$, see for example [77]. The magnetic moment $\vec{\mu}$ of an atom (ion) has orbital and spin contributions:

$$\vec{\mu} = -\mu_\mathrm{B}\vec{L} + g_s\mu_\mathrm{B}\vec{S}, \tag{5.1}$$

where $\mu_\mathrm{B} e\hbar/(2M_\mathrm{e})$ denotes the Bohr magneton, $\vec{L}$ the orbital angular momentum and $\vec{S}$ the total spin angular momentum. This description is valid in the Russell-Saunder (ls-coupling) regime only, in contrast to the jj-coupling regime, where the sum of all orbital angular momenta $\vec{L}$ and the total spin vector $\vec{S}$ are not a good basis for describing the wavefunction. The corresponding theory results in a more complex derivation of the Zeeman effect, which is beyond the scope of this thesis.

The interaction Hamiltonian of an atom in an external magnetic field is given by $\hat{H}_\mathrm{ZE} = \vec{\mu}\vec{B}$ and its expectation value is calculated on the basis of $\vec{L}$, $\vec{S}$, the total angular momentum $\vec{J}$ and its corresponding quantum number[1] M_J. The projection of the magnetic moment onto $\vec{J}$ and setting $\vec{B} = B \cdot \vec{e_z}$ allows for a calculation of the expectation value. Finally, the energy shift due to a static external magnetic field is written as:

$$\Delta E_\mathrm{ZE} = g_J \mu_\mathrm{B} M_J B, \tag{5.2}$$

[1] As long as this interaction can be treated as a perturbation to the fine structure.

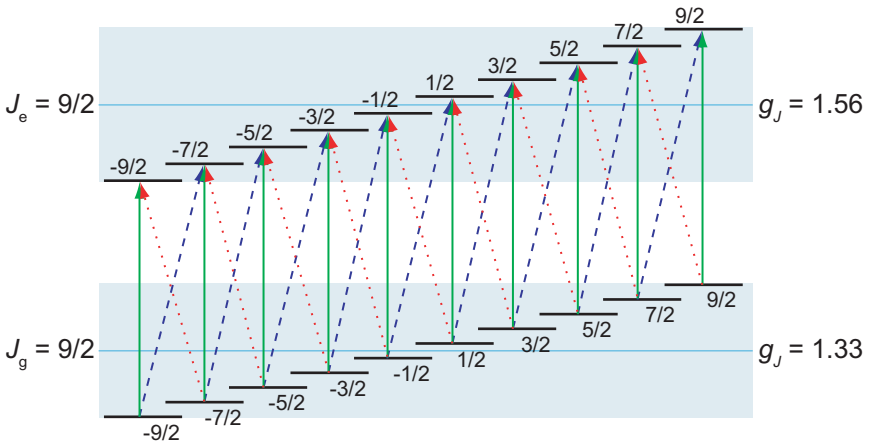

Fig. 5.1: Expected energy level diagram based on theoretical calculations of the Landé factors, including the magnetic sub-levels. The arrows indicate all possible transitions. Green/solid arrows represent the ten π transitions, blue/dashed arrows the nine σ^+ transitions and red/dotted the nine σ^- transitions.

where g_J denotes the Landé factor, which is given by[2]:

$$g_J = \frac{3}{2} + \frac{S(S+1) - L(L+1)}{2J(J+1)}. \tag{5.3}$$

The resulting energy shift for any given energy level is therefore a function of the quantum numbers L, S,and J. Hence a knowledge of the total angular momentum of the excited state is indeed required to calculate the level splitting.

Inserting the known quantum numbers of the ground and excited state of the relevant transition into Eq. (5.3), we obtain the following Landé factors: $g_J^{\mathrm{calc}}(^4F_{9/2}) = 1.33$ and $g_J^{\mathrm{calc}}(^6D_{9/2}) = 1.56$. With these values the energy level diagram shown in Fig. 5.1 is obtained. Using the appropriate selection rule $\Delta M_J = 0, \pm 1$ yields a splitting into 28 allowed transitions, indicated by the arrows in Fig. 5.1. These 28 transitions are comprised of ten π transitions and two times nine σ transitions.

Measurements

Measurements of the Zeeman splitting are carried out in the Penning trap, which requires that the magnetic field be homogeneous in the interaction

[2] When assuming the free electron g_s factor to be = 2.

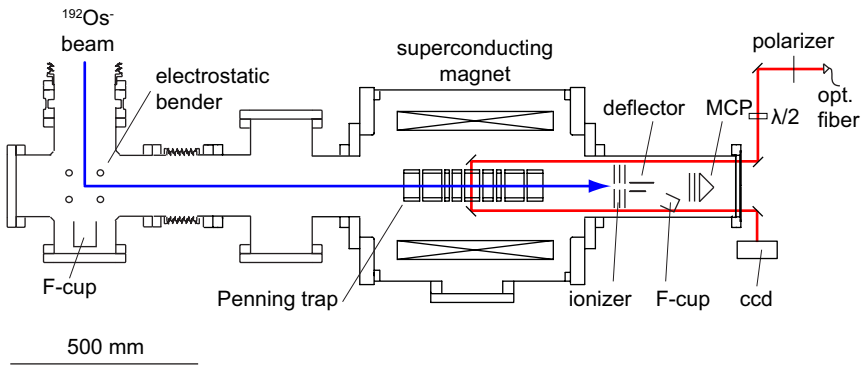

Fig. 5.2: Experimental setup for the transversal spectroscopy in the high magnetic field region.

region between ion beam and laser. For this purpose, the spectroscopy section is modified and attached to the superconducting magnet as shown in Fig. 5.2. In this arrangement the mass-separated ions – we have chosen $^{192}Os^{-}$ for the laser spectroscopy – are deflected towards the Penning trap by the electrostatic quadrupole bender. As discussed in Sec. 3.4 the laser light intersects the ion beam axis in the central magnetic field region, where its homogeneity and strength are maximal. In this volume the magnetic field is parallel to the ion beam axis. After interaction of the ions with the laser field, the osmium ions, now in either the ground or the excited state, travel in the direction of the spectrometer, which is placed as close to the interaction region as mechanical restrictions permit. Here the excitation of the ions is detected, using the same principle as described in Sec. 3.3.

For precise positioning of the laser light in front of the laser entrance window into the vacuum, an optical fiber is used. In this way the crucial laser alignment for guiding the light transversally through the Penning trap is decoupled from any re-alignment within the laser system itself. The alignment trough the trap is done with the help of the CCD camera, which is positioned in front of the exit window, as shown in Fig. 5.2. The linearly polarized light from the cw-OPO is coupled into a polarization-maintaining (PM) optical fiber on the laser table. An additional polarizer is placed behind the output coupler to reduce the amount of depolarized light due to imperfections in the optical fiber. For controlled rotation of the angle of the polarization ($\vec{P}$) with respect to the magnetic field a $\lambda/2$ plate is introduced into the laser path. This is necessary in order to change from the observation of π transitions ($\vec{P} \parallel \vec{B}$) to the observation of σ transitions ($\vec{P} \perp \vec{B}$).

The data acquisition system is left unmodified from the collinear spectroscopy case. Here again a chopper is used in order to reduce the level of background. Many spectroscopy measurements are performed for a range of magnetic-field strengths, starting with zero field and up to a maximum

state	g_J^{exp}	g_J^{calc}
$^4F_{9/2}$	1.31(7)	1.33
$^6D_{9/2}$	1.50(8)	1.56

Table 5.1: Comparison of experimental values of the Landé factors with the calculated estimate from Eq. (5.3). The experimental error results from the magnetic field uncertainty of ±5%

field strength of 1 T. In this way the center position of the transition is checked by comparing it with the result from the collinear setup. At each magnetic-field strength, the laser frequency is scanned and the spectra for each laser polarization with respect to the magnetic field are recorded.

All in all 28 spectra, each containing ten or 18 peaks depending on the laser polarization, were taken at twelve different magnetic-field strengths. Two typical spectra at 0.035 T are plotted in Fig. 5.3. The upper graph shows the spectra for the σ transitions and the lower one for the π transitions. These graphs include fits based on Eq. (5.2). Actually, two different fitting functions are needed, one for the σ and one for the π transitions. They use the following parameters: the line intensities, the peak width, the Landé factors and the magnetic-field strength. The peak widths are held fixed at the value found for zero field strength, where only one peak is present in the spectrum. The actual field of the superconducting magnet is entered directly into the fit. Finally, the g_J factors are the main parameters of interest. They can be compared in a straightforward manner with the calculated values. For this purpose, the fit routine is applied to all recorded spectra and the weighted means of the Landé factors are computed. Unfortunately, the magnetic-field strength is only determined from the current readout of the magnet power supply. The uncertainty of the resulting field is estimated to be 5%. This is the dominant systematic uncertainty and results in a corresponding final uncertainty in the determined Landé factors. For a more precise experimental determination, an independent measurement of the magnetic field, at the site of the interaction of the laser field with the ions, would have to be established.

The experimental results are shown in Table 5.1 together with the calculated values from Sec. 5.1, and it is evident that they are in agreement. However, it should be mentioned, that the theoretical values are calculated without taking into account relativistic effects, which can be of the order of a few percent or even more.

5.2 First Trapping Experiments with Electrons

The final set of measurements presented in this thesis concerns systematic tests of the UNIC Penning trap, and in particular a check of the quality

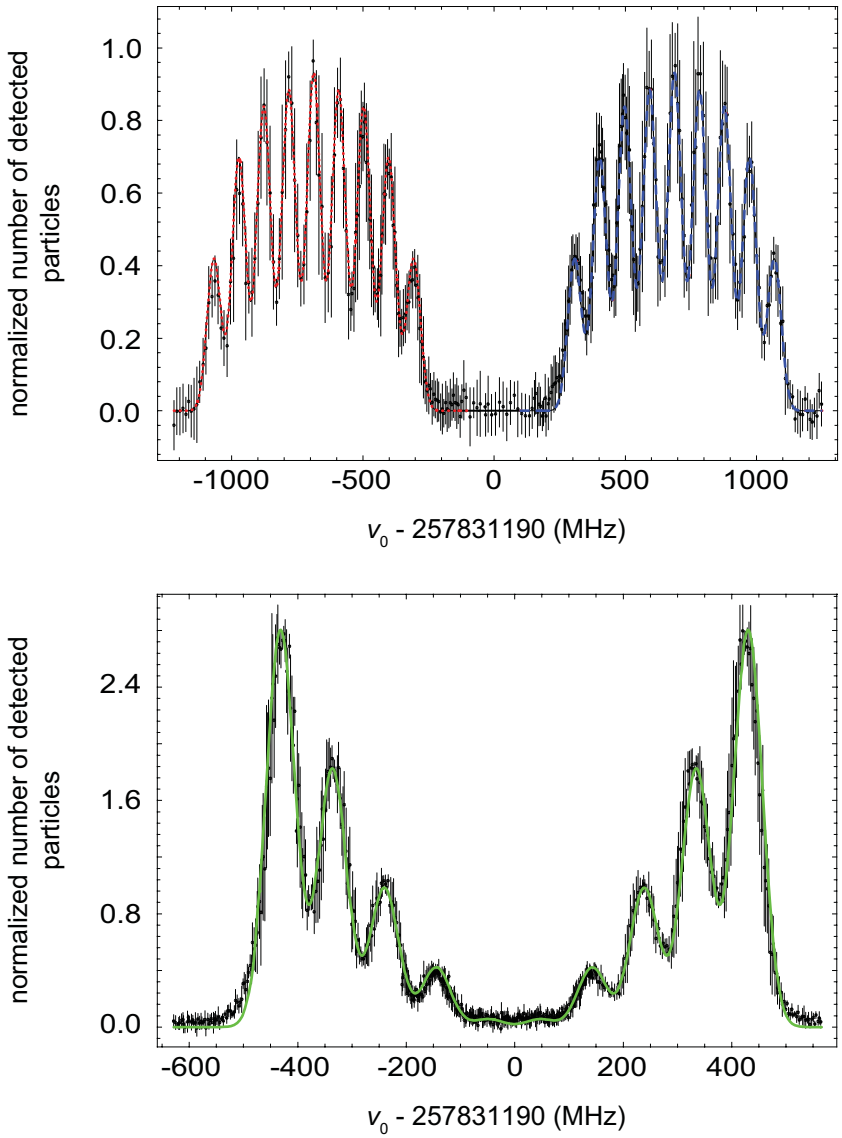

Fig. 5.3: Measured absorption spectrum in an external magnetic field of 0.035 T, Top: 2 times 9 peaks of the σ transitions. Bottom: 10 peaks of the π transitions. Both graphs also include the corresponding fits.

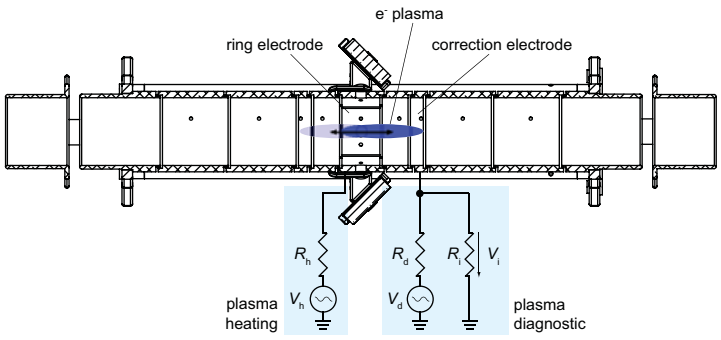

Fig. 5.4: Penning trap electrodes and heating and mode detection electronics used for the electron plasma diagnostics.

of its harmonic electric potential. For this purpose, measurements with a cold and dense electron plasma are performed. In addition to the plasma diagnostics mentioned in Sec. 2.2.1, a knowledge of the characteristics of the electron plasma is important for another reason. The sympathetic cooling of the osmium ions, prior to laser cooling, depends greatly on the density, ion number and temperature of the electron plasma (cf. Sec. 2.2.2). The successful application of that method therefore depends on a knowledge and control of these parameters.

Major parts of the plasma diagnostics are designed and assembled by the group of G. Testera at the National Institute for Nuclear Physics (INFN) in Genoa, Italy, and are finally adapted to the special requirements of the UNIC trap setup. An illustration of the trap including a sketch of the diagnostics setup is shown in Fig. 5.4. In this diagnostic system, the two axial plasma modes, the dipole $(1,0)$ and quadrupole $(2,0)$ modes, are excited by applying a sinusoidal RF perturbation to one of the correction electrodes, resulting in an electromotive force

$$V_d = v_\mathrm{d} \exp(i\omega t) \tag{5.4}$$

acting on the electron plasma. The oscillation of the ion cloud induces a current in the pickup electrode[3] and the corresponding voltage

$$V_\mathrm{i} = v_\mathrm{i}(\omega) \exp(i\omega t) \tag{5.5}$$

is measured across the resistance R_d. Experimentally the ratio $v_\mathrm{i}(\omega)/v_d$ is recorded as a function of the drive frequency ω_d by means of a network analyzer. A narrow stepwise frequency sweep of the voltage source across the resonance frequency is performed for each of the individual modes. The excitation amplitude v_d is of the order of 100...200 μV, and 20 to 30 steps in a

[3] In this setup, the pickup electrode is the same electrode on which the driving RF field is previously applied.

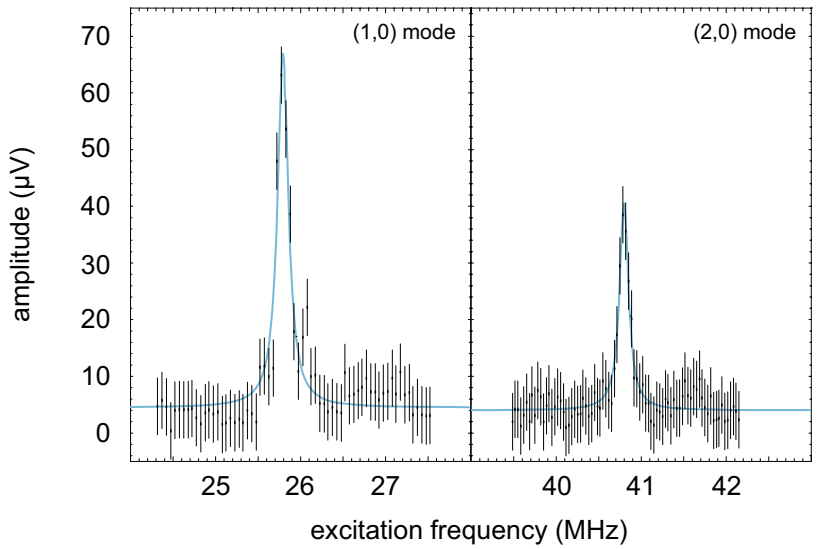

Fig. 5.5: Electron plasma excitation response following excitation near the (1,0) and (2,0) resonance frequencies, including corresponding Lorentzian fits to each resonance peak. Left: Detection of $(1,0)$ mode frequency. Right: Resonance of $(2,0)$ mode.

frequency range of 3 to 7 MHz are taken. Figure 5.5 shows typical resonance spectra of the first two plasma modes, which are recorded at Penning trap potential of: $V_0 = 95$ V and a magnetic field of $B_0 = 4.5$ T.

One important systematic test is the determination of the axial plasma oscillation frequency, because a comparison with a value calculated from Eq. (2.8b) indicates the quality of the electric potential and might reveal certain systematic effects. For this comparison the excitation frequency is scanned around the $(1,0)$ frequency of the electron plasma, which is equal to the axial frequency (cf. Sec. 2.2.1), and its response is recorded. This procedure is repeated for different trap depths, and the measured central frequencies are plotted in Fig. 5.6. The dashed line shows the behavior expected from Eq. (2.8b). As can be seen from the figure, there is no significant deviation of the experimental results from theory. We therefore deduce that the quality of the electric trap potential meets the requirements of this project.

In a second systematic test the electron plasma is heated by superimposing a radio frequency (RF) signal onto the constant ring electrode voltage, as illustrated in Fig. 5.4. The applied RF signal is in the range of 24 to 26 MHz (close to the first mode). Its amplitude can be set between 0 and 0.9 V. In the actual measurement the plasma evolves for a few seconds, then the RF heating is turned on (again for several seconds), and finally the electrons cool down due to their synchrotron radiation within a few seconds.

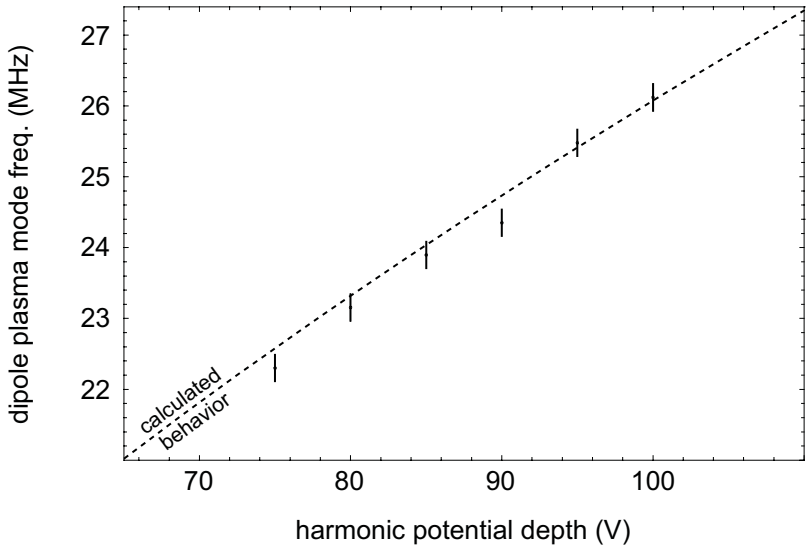

Fig. 5.6: The (1,0) plasma mode frequency vs. applied trap depth. The dashed line shows the calculated axial frequency (all parameters are fixed by simulation or experimental settings).

During the whole procedure the plasma modes are recorded. As we have seen in Sec. 2.2.1, the quadrupole mode frequency depends on the plasma temperature. Thus by fitting an exponential decay to the recorded data points in the time interval during which the electron plasma cools down again, the cyclotron cooling time of the electrons can be extracted. A typical measurement at a magnetic field of 2 T is plotted in Fig. 5.7. The RF heating phase is indicated by a red/shaded band. In this particular case the cooling time constant is determined to be $\tau = 1.4(2)$ s. Furthermore an estimation of the temperature change in the electron plasma due to the applied heating can be derived from the change in the 2nd mode frequency. This is achieved by inserting the obtained frequency values, at low and high plasma temperatures, into Eq. (2.18). Assuming an aspect ratio $\alpha \approx 19$, a plasma length $b \approx 4.5$ mm and a density $n \approx 10^8$ cm^{-3}, a temperature change $\Delta T \approx 900$ K is obtained.

Similar measurements were conducted for different magnetic fields. The resulting relaxation times are plotted in Fig. 5.8 and compared to the theoretical prediction of the synchrotron radiation time constant τ_e, as introduced in Eq. (2.20). The dashed line in the figure represents this theoretical prediction. The apparent disagreement indicates the presence of one or more heating effects concurrently with the dominating cyclotron cooling. A similar result is obtained in the cooling time measurements, conducted also on a cold pure-electron plasma, presented in Ref. [69]. For higher magnetic

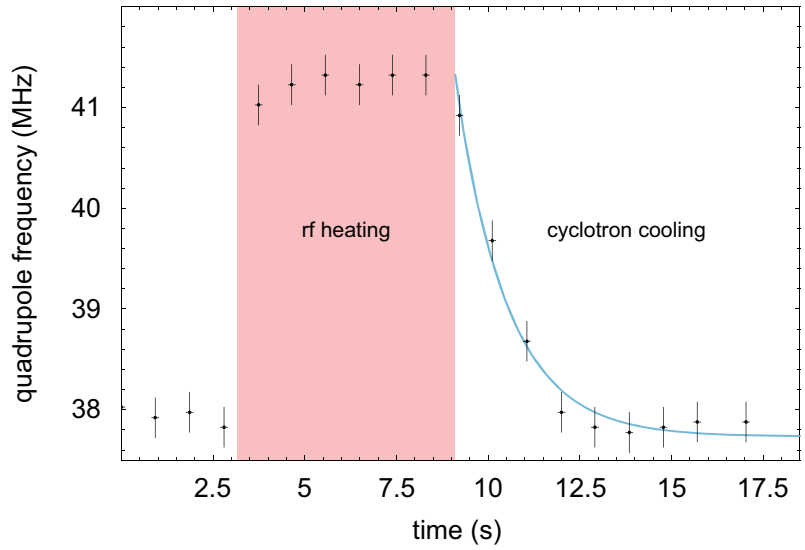

Fig. 5.7: RF heating of the e^- plasma followed by cyclotron cooling after the heating is turned off ($B_0 = 2$ T). An exponential fit to the (2,0) mode frequency during the cooling results in a determination of the cooling time of the electrons.

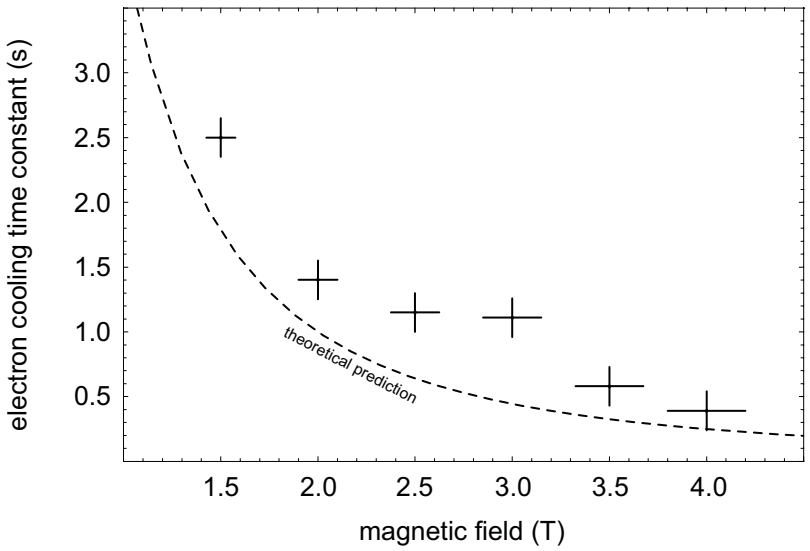

Fig. 5.8: Electron cooling time constant as a function of the magnetic field. The observed time constants are higher than expected from theory (dashed), probably due to additional heating effects.

fields, corresponding to higher cooling rates, the heating effects become less prominent.

Further investigations on the origin and strength of the observed heating process(es) are required as progress is made toward laser cooling of Os^-. However, the systematic checks presented above are a good starting point for the intended sympathetic cooling of the negative osmium ions. In addition, first attempts of trapping Os^- have been made. They indicate storage times of several seconds and more. However, these preliminary results are not presented here, since not all systematic effects are understood and further improvements of the trapping procedure are expected in future attempts.

6. PROSPECT OF LASER COOLING NEGATIVE OSMIUM

This chapter summarizes all relevant results in order to give an outlook on the prospect of laser cooling negative osmium ions. In particular, the influence of the magnetic field is considered, beyond the points already discussed in Ref. [16]. The most significant results obtained in the course of this thesis are:

- The total angular momentum of the excited state was found to be $J_{e1} = 9/2$;
- High-resolution spectroscopy of the ${}^4F_{9/2} \rightarrow {}^6D_{9/2}$ transition yielded a transition frequency of $\nu_0 = 257.831190(35)$ THz;
- An observed cross-section of $\sigma_0 = 2.5(7) \times 10^{-15}$ cm^2 was measured, resulting in an estimate of the Einstein A coefficient of $A \approx 330$ s^{-1};
- The expected Zeeman splitting in an external magnetic field was confirmed, yielding the Landé factors $g_J^{g1} = 1.31(7)$ and $g_J^{e1} = 1.50(8)$;
- In the external magnetic field, the intensity ratio in the ensemble of the 28 lines in the ${}^4F_{9/2} \rightarrow {}^6D_{9/2}$ transition was observed.

All of the following discussion and remarks are based on these facts as well as additional considerations, most of which have already been introduced in Chap. 2, or are taken from Refs. [44] and [45].

The Doppler cooling of negative osmium will take several minutes when using Eq. (2.29) and assuming an Einstein A coefficient of 330 s^{-1}. The corresponding theoretical Doppler cooling limit, cf. Eq. (2.27), is $T_{\text{limit}} \approx 1.3$ nK. It can, however, not be achieved with our current experimental setup, since the laser bandwidth of ≈ 5 MHz will limit the minimal temperature (cf. Sec. 2.2.3) to ≈ 120 μK.

The starting point of our analysis is an ensemble of negative osmium ions trapped in a Penning trap in thermal equilibrium, assuming that their equilibrium temperature of $T_{\text{Os}} \approx 100$ K (or 4.2 K) has been reached by a pre-cooling technique. As mentioned in Sec. 2.2.2, this could be achieved by sympathetic cooling with electrons, or, if this does not prove feasible, by buffer gas cooling [106, 107] or resistive cooling [108]. The corresponding spectral line width due to Doppler broadening at that temperature is $\Gamma_{\text{res}} \approx 80$ MHz (or 16 MHz). We implicitly assume that the storage time

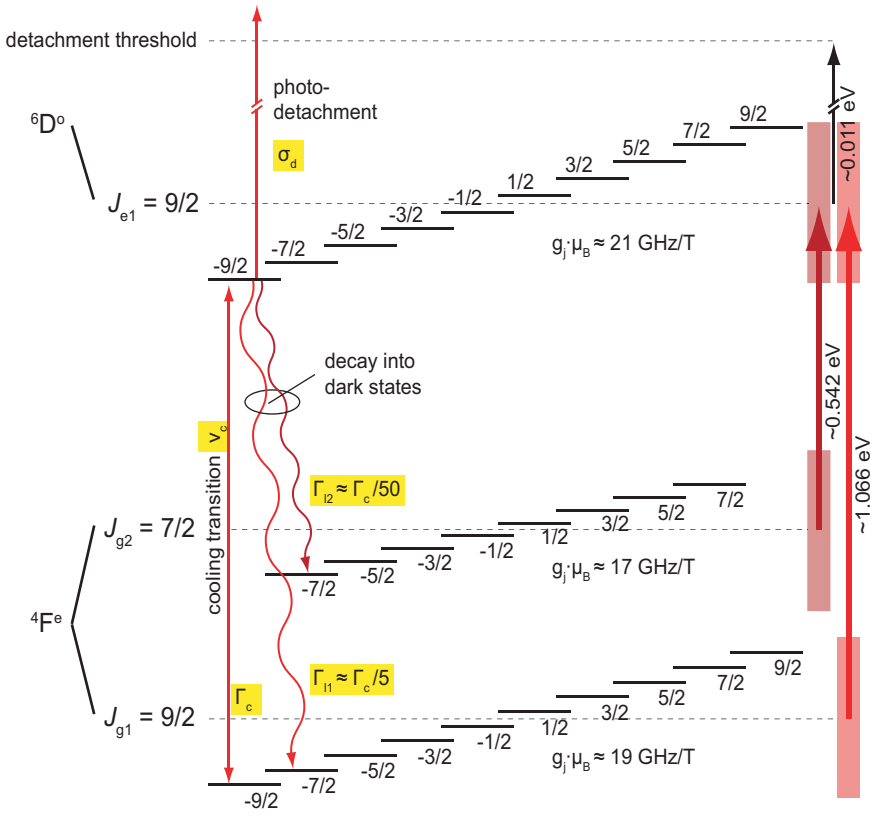

Fig. 6.1: Energy level diagram of Os^- in the presence of a magnetic field. The straight arrow indicates the strongest transition, which can be deployed as a cooling transition, whereas the wiggly arrows illustrate the possible escape channels, which will need to be re-pumped.

of the negative osmium ions inside the trap is long enough to proceed with laser cooling – at least several minutes. Here, the laser cooling will be performed via the ${}^4F_{9/2} \rightarrow {}^6D_{9/2}$, $M_J = -9/2$ to $M_J = -9/2$ transition, since it is one of the strongest available transitions. When tuning the laser to this transition, the light interacts only with roughly 1/6 of the ion ensemble, according to the intensity ratios observed in the absorption spectrum in the presence of the external magnetic field (cf. Fig. 5.3). In Fig. 6.1 the chosen transition is indicated by ν_c and its decay rate by Γ_c. It is denoted in the following as the cooling transition with the cross-section σ_c. In addition, all decay and loss channels from the excited state ${}^6D_{9/2}$, $M_J = -9/2$ are illustrated in this energy level diagram and their individual branching ratios are indicated. In particular, the partial lifetime $1/\Gamma_{l1} \approx 5/\Gamma_c$ of the decay into the ${}^4F_{9/2}$, $M_J = -7/2$ ground state is determined from the spectra shown in Fig. 5.3, and the partial lifetime $1/\Gamma_{l2}$ into the ${}^4F_{7/2}$, $M_J = -7/2$ ground state is estimated to be approximately ten times longer, using the fact that

the lifetimes scale as ν^{-3}. This then leads to a decay rate of $\Gamma_{l2} \approx \Gamma_c/50$. Finally, the photo-detachment cross-section σ_d from the excited state into the continuum is considered, since a laser photon can cause the detachment of the valence electron, leading to an undesirable loss of ions.

In order to describe the time evolution of the states in the presence of the cooling laser, a system of standard rate equations, similar to the one applied in Sec. 4.1.2, is introduced. When considering all fundamental decay and loss channels mentioned above, and assuming that the ions remain in the laser spot at all times, the system of rate equations is given by:

$$\frac{dN_{g1}(t)}{dt} = -\sigma_c \phi N_{g1}(t) + (\sigma_c \phi + \Gamma_c) N_e(t) \tag{6.1a}$$

$$\frac{dN_{g2}(t)}{dt} = \Gamma_{l1} N_e(t) \tag{6.1b}$$

$$\frac{dN_{g3}(t)}{dt} = \Gamma_{l2} N_e(t) \tag{6.1c}$$

$$\frac{dN_e(t)}{dt} = \sigma_c \phi N_{g1}(t) - [(\sigma_c + \sigma_d)\phi + \Gamma_c + \Gamma_{l1} + \Gamma_{l2}] N_e(t) \tag{6.1d}$$

$$\frac{dN_d(t)}{dt} = \sigma_d \phi N_e(t), \tag{6.1e}$$

where N_{g1} is the ${}^4F_{9/2}$, $M_J = -9/2$ state, N_{g2} the ${}^4F_{9/2}$, $M_J = -7/2$ state and N_{g3} the ${}^4F_{7/2}$, $M_J = -7/2$ state population. The population of the ${}^6D_{9/2}$, $M_J = -9/2$ excited state and the number of photo-detached ions are denoted by N_e and N_d. Moreover, the observed resonant cross-section is given by $\sigma_c = \left(4\pi^2 \nu_c \tau \Gamma_{res}\right)/c^2$, in order to take into account that the resonance has a finite width due to the Doppler broadening and the finite laser bandwidth. The photon flux ϕ is given by $\phi = I_{las}/(h\nu_{las})$, where I_{las} is the laser intensity and ν_{las} its frequency. Laser cooling is most effective when the laser is detuned from resonance by $\delta = \Gamma_{res}/2$. Furthermore, the laser intensity should be chosen such that the ion absorbs a photon only after its spontaneous decay back into the ${}^4F_{9/2}$, $M_J = -9/2$ ground state, otherwise photo-detachment can occur. We can estimate the required optimal laser intensity by:

$$I_{las} \approx \frac{h\nu_{las}}{2\tau\sigma_c(\delta)}, \tag{6.2}$$

since the scattering rate saturates to $1/(2\tau)$ [109]. For Os^- this intensity will lead to the maximal scattering rate of $\approx 165\ s^{-1}$ of photons from the laser field. In Eq. (6.2), $\sigma_c(\delta)$ denotes the observed cross-section for a chosen detuning δ, which is determined by the measurement in Sec. 4.1.2.

The system of rate equations is solved analytically; it is assumed that all ions are initially in the ${}^4F_{9/2}$, $M_J = -9/2$ ground state and their temperature (T_{ion}) does not significantly change within the observed timescales. The

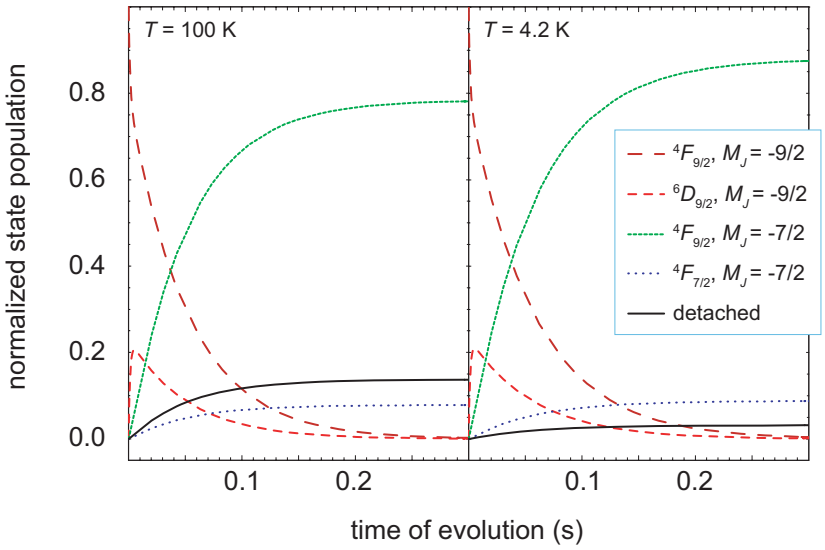

Fig. 6.2: Time evolution of the ion state population in the presence of a laser field for two different ensemble temperatures. The calculation is based on the solution of Eqs. (6.1a)–(6.1e) with the parameters listed in Table 6.1.

T (K)	Γ_{res} (MHz)	I_{las} (mW/cm^2)
100	80	39.9
4.2	16	8.2

Table 6.1: The parameters for different ensemble temperatures used in Eqs. (6.1a)–(6.1e) to produce the plots in Fig. 6.2. The required laser intensity I_{las} is calculated using Eq. (6.2).

result of the evaluation for two different ensemble temperatures is plotted in Fig. 6.2 and the corresponding parameters are listed in Table 6.1. The following conclusions can be drawn from this calculation:

- The small Einstein A coefficient of the cooling transition leads to rather low cooling powers and correspondingly long cooling times; any possible loss mechanism has to be minimized;
- The loss of ions due to photo-detachment is very sensitive to the laser intensity. A lower pre-cooling temperature of 4.2 K would greatly reduce the fraction of neutralized ions; and
- The transition of ions into *dark* states[1] stops the cooling process after the scattering of only ≈ 50 photons – however, at least $\approx 10^4$ photons have to be scattered for a significant cooling effect.

In this consideration the laser-ion interaction ends after ≈ 0.3 s, because the ions find themselves in the $^4F_{9/2}$, $M_J = -7/2$ and $^4F_{7/2}$, $M_J = -7/2$ (dark) states. Their lifetimes toward a decay back into the initial $^4F_{9/2}$, $M_J = -9/2$ state are assumed to be long, seconds or even longer – typical lifetimes of metastable states. Most critical is the loss into the $^4F_{9/2}$, $M_J = -7/2$ state, as can be seen in Fig. 6.2. Thus, a method has to be applied which brings the ions from these dark states back into the cooling cycle. For example, further lasers can be introduced to re-pump the ions back into the $^6D_{9/2}$, $M_J = -9/2$ state – from here they can contribute again to the cooling cycle. These re-pumpers should be narrow-bandwidth lasers, since otherwise their own contribution to photo-detachment becomes non-negligible. However, the processes within the confining potential of the Penning trap, e.g. the occurrence of sidebands, the corresponding influence of the finite laser bandwidth and, finally, the internal dynamics – the evolution of states – of the ions, have to be studied in more detail in order to understand all restrictions and/or possibilities of laser cooling of negative osmium.

Laser-Assisted Evaporative Cooling – Alternative Approach

Another well-known cooling technique is evaporative cooling. In the case of negative ions it can be combined with laser excitation. A theoretical description of this specific method, which is based on velocity-selective photo-detachment, is presented in Ref. [110]. It has no analogous form in positive ions or atoms.

For laser-assisted evaporative cooling the frequency is tuned slightly below the photo-detachment threshold, thereby causing a loss of ions above a certain velocity component in the direction of the laser beam. Here, we

[1] States which are no longer addressed by the cooling laser.

again assume that the ion ensemble is in thermal equilibrium. However, in contrast to the Doppler cooling that is described above, pre-cooling is not necessary. Ions with velocities lower than the corresponding threshold remain unharmed, whereas ions with higher velocities are neutralized. If the average thermal energy of the neutralized ions is higher than the initial energy of the ensemble, the remaining ions will re-thermalize through collisions, leading to a colder sample. This cooling technique can in principle be applied until a single ion is left in the trap, but larger particle numbers lead to faster equilibration times. The method of laser-assisted evaporative cooling, which does not rely on a resonant transition, can be used with any atomic negative ion species and represents a promising alternative to Doppler cooling.

7. CONCLUSION

In the course of this thesis, all main components of the UNIC apparatus were designed, built and/or commissioned: the negative-ion sputter source, the ion-beam line (ion optics, diagnostics, and mass separation unit), the spectroscope (for in-beam laser spectroscopy), the cw-OPO laser system, and the cryogenic Penning trap. Once each individual component had been characterized in several systematic tests, first experiments were conducted.

The high-resolution laser spectroscopy on the bound–bound E1 transition of $^{192}Os^-$ resulted in a 100-fold higher precision than the only prior measurement, and it agrees with the earlier result to within 0.6σ. Together with the determination of the resonant cross-section, which implicitly yielded the Einstein A coefficient, it concluded the first milestone of our project. In the subsequent experiments on all naturally occurring isotopes of osmium, the heretofore unknown total angular momentum of the bound excited state ^6D was found to be $J = 9/2$. In addition to this crucial information for future experiments on negative osmium, the hyperfine structure constants A and B of the odd isotopes were determined and the isotope shift was deduced from the corresponding spectra of all isotopes. Altogether, these experiments present the most precise study on any atomic anion to this day.

A second milestone was addressed in the course of measurements in high magnetic fields. The magnetic field of the superconducting magnet was used to split the energy levels into magnetic sub-levels. The mechanical setup of the cylindrical Penning trap enabled the transverse laser interaction with the negative ion beam. Spectra were recorded for different orientations of the laser polarization with respect to the magnetic field, enabling the separate observation of $\sigma^{+,-}$ and π transitions. All in all 28 lines were resolved, confirming the previous result of the total angular momentum of the excited state. In these experiments, the precision was hampered by the knowledge of the magnetic-field magnitude, resulting in an absolute uncertainty of 5%. But within these constrains, the experimental results of the Landé factors are in agreement with simple semi-classical calculations.

In addition to these laser spectroscopy measurements, the first successful trapping, manipulation and diagnostics experiments on the electron plasma in the cryogenic Penning trap were achieved. These results represent a starting point for the proposed pre-cooling of stored negative osmium ions. A stored cryogenic ensemble of Os^- is required for the ultimate goal, the actual laser cooling of negative ions.

The next milestone is the fluorescence spectroscopy of trapped Os^-. The UNIC apparatus has been prepared for this experiment, in which a photo multiplier tube (PMT) is foreseen as the fluorescence light detector. A stringent requirement for the success of such an experiment is the reduction of any ion loss mechanism, thus allowing for long (a few minutes, or even longer) storing and observation times. Another great challenge will be the expected count rate on the PMT, which is limited by the spontaneous decay rate, expected to be as low as ≈ 50 Hz due to the low Einstein A coefficient. This is particularly demanding of a low background level of the PMT. Spurious counts on the detector might result from dark counts and electronic noise, but most critically from scattered laser light, which, however, could be reduced by an appropriate combination of polarization filters. Furthermore, the experiment will only be feasible if at least one re-pumping laser is introduced, as discussed in Chap. 6.

The perspective of sympathetically cooling antiprotons with a laser-cooled anion ensemble is especially appealing since it might bring ultracold antihydrogen within reach. The fundamental questions which could be addressed with a cold sample of antihydrogen atoms, and the ongoing quest of finding their answers experimentally, warrant further investigations of negative osmium ions.

LIST OF FIGURES

1.1 Three possible ways to produce cold antihydrogen 3

2.1 Cutout of periodic table of elements with their EA 5
2.2 Binding potential in neutral atoms and negative ions 7
2.3 Photo-detachment spectrum of Os^- 9
2.4 Energy level diagram of Os^- 9
2.5 Breakup rate of the ${}^6D_{J_{e1}}$ state vs. electric field strength . . . 11
2.6 Breakup rate due to ion–ion collision 12
2.7 Photo-detachment cross-section from the ${}^6D_{J_{e1}}$ state 13
2.8 Lifetime of the ${}^6D_{J_{e1}}$ state due to BBR 14
2.9 Single particle orbit in the radial plane 16
2.10 A non-neutral plasma cloud 19
2.11 Sympathetic cooling technique 21
2.12 Electron cooling estimates for Os^- 23
2.13 Doppler cooling principle 24
2.14 Loss of cooling efficiency due to finite laser bandwidth 26
2.15 Optical sidebands in a harmonic trap 28

3.1 Cross-sectional view of the negative ion source 30
3.2 Ion beam setup 31
3.3 Laser system 32
3.4 Idler wave frequency as a function of the etalon angle 33
3.5 Schematic view of the spectrometer 34
3.6 Detailed sketch of the Penning trap 35
3.7 Simulated trapping potential 37
3.8 3D illustration of the Penning trap inside the magnet 39

4.1 Experimental setup for collinear spectroscopy 41
4.2 Resonance of the ${}^4F_{9/2} \rightarrow {}^6D_{J_{e1}}$ transition of $^{192}Os^-$ 43
4.3 Doppler shift for different beam energies 44
4.4 Time evolution of states in Os^- for different laser powers . . 46
4.5 Number of detected atoms vs. laser intensity at resonance . . 47
4.6 Isotopic shift of the E1 transition in Os^- 49
4.7 Residual isotope shifts vs. $\delta\langle r^2\rangle^{A,192}$ 52
4.8 Measured hyperfine splitting of $^{187}Os^-$ and $^{189}Os^-$ 53
4.9 Energy level diagram for $^{187}Os^-$ and $^{189}Os^-$ 55

5.1 Energy level scheme including magnetic sub-levels 58
5.2 Experimental setup for Zeeman spectroscopy 59
5.3 Absorption spectrum in an external magnetic field 61
5.4 Trap electrodes including electronics for diagnostics 62
5.5 Electron plasma excitation response 63
5.6 The (1,0) plasma mode frequency vs. applied trap depth . . . 64
5.7 RF heating of the e^- plasma followed by cyclotron cooling . . 65
5.8 Electron cooling time vs. magnetic field 65

6.1 Energy level diagram of Os^- in a magnetic field 68
6.2 Time evolution of states in the laser field 70

LIST OF TABLES

2.1 Different Penning trap frequencies 16

3.1 Design values for trap dimensions and voltages 36
3.2 Specifications of the superconducting magnet 38

4.1 Isotope masses, abundances and resonance frequencies 48
4.2 Residual isotope shifts vs. $\delta\langle r^2\rangle^{A,192}$ 51
4.3 Determined isotope shift coefficients 51
4.4 Hyperfine structure constants 55
4.5 Ratios of the magnetic dipole moment coupling constants . . 56

5.1 Comparison of exp. and theo. Landé factors 60

6.1 Parameters for different ensemble temperatures 70

BIBLIOGRAPHY

[1] C. D. Anderson. The positive electron. *Phys. Rev.*, 43:491, 1933. doi:10.1103/PhysRev.43.491.

[2] O. Chamberlain et al. Observation of antiprotons. *Phys. Rev.*, 100:947, 1955. doi:10.1103/PhysRev.100.947.

[3] John F. Donoghue. General relativity as an effective field theory: The leading quantum corrections. *Phys. Rev. D*, 50(6):3874, 1994. doi:10.1103/PhysRevD.50.3874.

[4] Particle Data Group, K. Hagiwara, et al. Review of particle properties. *Phys. Rev. D*, 66:010001, 2002. doi:10.1103/PhysRevD.66.010001.

[5] M. Niering et al. Measurement of the hydrogen 1S- 2S transition frequency by phase coherent comparison with a microwave cesium fountain clock. *Phys. Rev. Lett.*, 84:5496, 2000. doi:10.1103/PhysRevLett.84.5496.

[6] G. Gabrielse et al. Antihydrogen production within a Penning-Ioffe trap. *Phys. Rev. Lett.*, 100:113001, 2008. (ATRAP Collaboration). doi:10.1103/PhysRevLett.100.113001.

[7] G. B. Andresen et al. Compression of antiproton clouds for antihydrogen trapping. *Phys. Rev. Lett.*, 100:203401, 2008. (ALPHA Collaboration). doi:10.1103/PhysRevLett.100.203401.

[8] A. Kellerbauer et al. Proposed antimatter gravity measurement with an antihydrogen beam. *Nucl. Instr. and Meth. in Phys. Res. B*, 266:351, 2008. (AEGIS Proto-Collaboration). doi:10.1016/j.nimb.2007.12.010.

[9] M Holzscheiter, M Charlton, and M Nieto. The route to ultra-low energy antihydrogen. *Phys. Rep.*, 402:1, 2004. doi:10.1016/j.physrep.2004.08.002.

[10] M. Amoretti et al. Production and detection of cold antihydrogen atoms. *Nature*, 419:456, 2002. (ATHENA Collaboration). doi:10.1038/nature01096.

[11] G. Gabrielse et al. Background-free observation of cold antihydrogen with field-ionization analysis of its states. *Phys. Rev. Lett.*, 89:213401, 2002. (ATRAP Collaboration). doi:10.1103/PhysRevLett.89.213401.

[12] G. Gabrielse et al. First measurement of the velocity of slow antihydrogen atoms. *Phys. Rev. Lett.*, 93:073401, 2004. (ATRAP Collaboration). doi:10.1103/PhysRevLett.93.073401.

[13] N. Madsen et al. Spatial distribution of cold antihydrogen formation. *Phys. Rev. Lett.*, 94:033403, 2005. (ATHENA Collaboration). doi:10.1103/PhysRevLett.94.033403.

[14] K. S. E. Eikema, J. Walz, and T. W. Hänsch. Continuous coherent Lyman- alpha excitation of atomic hydrogen. *Phys. Rev. Lett.*, 86:5679, 2001. doi:10.1103/PhysRevLett.86.5679.

[15] J. Walz et al. Cold antihydrogen atoms. *Appl. Phys. B*, 77:713, 2003. doi:10.1007/s00340-003-1344-y.

[16] A. Kellerbauer and J. Walz. A novel cooling scheme for antiprotons. *New J. Phys.*, 8:45, 2006. doi:10.1088/1367-2630/8/3/045.

[17] T. Anderson, H. K. Haugen, and H. Hotop. Binding energies in atomic negative ions: III. *J. Phys. Chem. Ref. Data*, 28:1511, 1999. doi:10.1063/1.556047.

[18] J. C. Rienstra-Kiracofe et al. Atomic and molecular electron affinities: Photoelectron experiments and theoretical computations. *Chem. Rev.*, 102:231, 2002. doi:10.1021/cr990044u.

[19] B. J. Greenblatt, M. T. Zanni, and D. M. Neumark. Photodissociation of I-2(-)(Ar)(n) clusters studied with anion femtosecond photoelectron spectroscopy. *Science*, 276:1675, 1997. doi:10.1126/science.276.5319.1675.

[20] K. Asmis, T. Taylor, and D. Neumark. Electronic structure of indium phosphide clusters: anion photoelectron spectroscopy of In^xP^x- and In^x+$1P^x$- (x=1-13) clusters. *Chem. Phys. Lett.*, 308:347, 1999. doi:10.1016/S0009-2614(99)00671-5.

[21] E. Herbst. Can negative molecular ions be detected in dense interstellar clouds? *Nature*, 289:656, 1981. doi:10.1038/289656a0.

[22] S. Petrie and E. Herbst. Some interstellar reactions involving electrons and neutral species: Attachment and isomerization. *ApJ*, 491:210, 1997. doi:10.1086/304941.

[23] I. Musa et al. Ultra-low-threshold field emission from conjugated polymers. *Nature*, 395:362, 1998. doi:10.1038/26444.

[24] H.S.W. Massey. *Negative Ions*. Cambridge Univ. Press, 3rd edition, 1976.

[25] B. M. Smirnov. *Negative Ions*. McGraw-Hill, 1982.

[26] D. R. Bates. Negative ions: Structure and spectra. In *Adv. At. Mol. Phys.*, volume 27, page 1. Academic Press, 1990.

[27] D. J. Pegg. Structure and dynamics of negative ions. *Rep. Prog. Phys.*, 67:857, 2004. doi:10.1088/0034-4885/67/6/R02.

[28] T. Andersen. Atomic negative ions: Structure, dynamics and collisions. *Phys. Rep.*, 394:157, 2004. doi:10.1016/j.physrep.2004.01.001.

[29] S. Geltman. Multiphoton detachment of an electron from H^-. *Phys. Rev. A*, 42:6958, 1990. doi:10.1103/PhysRevA.42.6958.

[30] M. L. Du. Photodetachment spectra of H^- in parallel electric and magnetic fields. *Phys. Rev. A*, 40:1330, 1989. doi:10.1103/PhysRevA.40.1330.

[31] M. Vincke and D. Baye. Variational study of H^- and He in strong magnetic fields. *J. Phys. B*, 22:2089, 1989. doi:10.1088/0953-4075/22/13/013.

[32] H. Hotop et al. High-resolution photodetachment study of Se^- ions. *Phys. Rev. A*, 8:762, 1973. doi:10.1103/PhysRevA.8.762.

[33] J. B. Vosko et al. Theoretical study of even- and odd-parity states in La^- and Ac^-: Evidence for the uniqueness of La^-. *Phys. Rev. A*, 43:6389, 1991. doi:10.1103/PhysRevA.43.6389.

[34] D. Datta and D. R. Beck. Electron affinities of opposite-parity bound states in Th^-: Relativistic-configuration-interaction studies. *Phys. Rev. A*, 50:1107, 1994. doi:10.1103/PhysRevA.50.1107.

[35] K. Dinov et al. Electron affinities of six bound states of Ce^- formed by attachment of $6p$ and $5d$ electrons to Ce. *Phys. Rev. A*, 50:1144, 1994. doi:10.1103/PhysRevA.50.1144.

[36] S. M. O'Malley and D. R. Beck. Calculation of Ce^- binding energies by analysis of photodetachment partial cross sections. *Phys. Rev. A*, 74:042509, 2006. doi:10.1103/PhysRevA.74.042509.

[37] S. M. O'Malley and D. R. Beck. Valence calculations of lanthanide anion binding energies: $6p$ attachments to $4f^n 6s^2$ thresholds. *Phys. Rev. A*, 78:012510, 2008. doi:10.1103/PhysRevA.78.012510.

[38] C. H. Greene. Photoabsorption spectra of the heavy alkali-metal negative ions. *Phys. Rev. A*, 42:1405, 1990. doi:10.1103/PhysRevA.42.1405.

[39] J. L. Krause and R. S. Berry. Electron correlation in alkali negative ions. In *18th Conf. At. Mol. Phys.*, page 91, 1986. Comments.

[40] C. Froese Fischer and D. Chen. Numerical multiconfiguration Hartree-Fock calculations for nsnp3P states of Rb and Cs negative ions. *J. Mol. Struct.*, 199:61, 1989. doi:10.1016/0166-1280(89)80042-9.

[41] A. M. Covington et al. Measurement of the electron affinity of lanthanum. *J. Phys. B*, 31:L855, 1998. doi:10.1088/0953-4075/31/20/002.

[42] M. Scheer et al. Experimental evidence that the $6s6p^3p_j$ states of Cs^- are shape resonances. *Phys. Rev. Lett.*, 80:684, 1998. doi:10.1103/PhysRevLett.80.684.

[43] C. W. Walter et al. Infrared photodetachment of Ce^-: Threshold spectroscopy and resonance structure. *Phys. Rev. A*, 76:052702, 2007. doi:10.1103/PhysRevA.76.052702.

[44] R. C. Bilodeau and H. K. Haugen. Experimental studies of Os^-: Observation of a bound-bound electric dipole transition in an atomic negative ion. *Phys. Rev. Lett.*, 85:534, 2000. doi:10.1103/PhysRevLett.85.534.

[45] P. L. Norquist and D. R. Beck. Binding energies, hyperfine structure, and magnetic dipole decay rates for Os^- $5d^7 6s^2\ ^4f$ levels. *Phys. Rev. A*, 61:014501, 2000. doi:10.1103/PhysRevA.61.014501.

[46] H. K. Haugen et al. Storage-ring experiments with 10-100-keV Ca^- beams: Role of blackbody radiation. *Phys. Rev. A*, 46:R1, 1992. doi:10.1103/PhysRevA.46.R1.

[47] B. M. Smirnov and M. I. Chibisov. Breaking uo of atomic particles by an electric field and by electron collision. *Sov.Phys.–JETP*, 22:585, 1966.

[48] A. M. Perelomov et al. Ionization of atoms in an alternating electric field. *Sov.Phys.–JETP*, 23:924, 1966.

[49] E. P. Wigner. On the behavior of cross sections near thresholds. *Phys. Rev.*, 73:1002, 1948. doi:10.1103/PhysRev.73.1002.

[50] M. Scheer, R. C. Bilodeau, and H. K. Haugen. Negative ion of boron: An experimental study of the $3p$ ground state. *Phys. Rev. Lett.*, 80:2562, 1998. doi:10.1103/PhysRevLett.80.2562.

[51] M. Scheer et al. Threshold photodetachment of Al^-: Electron affinity and fine structure. *Phys. Rev. A*, 57:R1493, 1998. doi:10.1103/PhysRevA.57.R1493.

[52] T. Van Kleff and P. Klinkenberg. Spectral structure of neutral and ionized osmium. *Physica*, 27:83, 1961. doi:10.1016/0031-8914(61)90023-4.

[53] H. G. Dehmelt. Radiofrequency spectroscopy of stored ions I: Storage. *Adv. At. Mol. Phys.*, 3:53, 1969.

[54] L. S. Brown and G. Gabrielse. Geonium theory: Physics of a single electron or ion in a penning trap. *Rev. Mod. Phys.*, 58:233, 1986. doi:10.1103/RevModPhys.58.233.

[55] P. K. Ghosh. *Ion Traps.* Oxford Science Publications, 1995.

[56] J. B. Jeffries et al. Theory of space-charge shift of ion cyclotron resonance frequencies. *Int. J. of Mass Spectrom. and Ion Process.*, 54:169, 1983. doi:10.1016/0168-1176(83)85016-2.

[57] D. F. A. Winters et al. Electronic detection of charged particle effects in a Penning trap. *J. Phys. B*, 39:3131, 2006. doi:10.1088/0953-4075/39/14/019.

[58] L. R. Brewer et al. Static properties of a non-neutral $^9Be^+$-ion plasma. *Phys. Rev. A*, 38:859, 1988. doi:10.1103/PhysRevA.38.859.

[59] D. H. E. Dubin. Theory of electrostatic fluid modes in a cold spheroidal non-neutral plasma. *Phys. Rev. Lett.*, 66:2076, 1991. doi:10.1103/PhysRevLett.66.2076.

[60] D. H. E. Dubin. Equilibrium and dynamics of uniform density ellipsoidal non-neutral plasmas. *Phys. of Fluids B: Plasma Physics*, 5:295, 1993. doi:10.1063/1.860571.

[61] J. Bollinger et al. Low order modes of an ion cloud in a Penning trap. *Phys. Scr.*, 46:282, 1992. doi:10.1088/0031-8949/46/3/013.

[62] M. Amoretti et al. Complete nondestructive diagnostic of nonneutral plasmas based on the detection of electrostatic modes. *Phys. Plasmas*, 10:3056, 2003. (ATHENA Collaboration). doi:10.1063/1.1591187.

[63] D. J. Larson et al. Sympathetic cooling of trapped ions: A laser-cooled two-species nonneutral ion plasma. *Phys. Rev. Lett.*, 57:70, 1986. doi:10.1103/PhysRevLett.57.70.

[64] G. I. Budker et al. Experimental studies of electron cooling. *Part. Accel.*, 7:197, 1976.

[65] M. Steck et al. Electron cooling of heavy ions. *Nucl. Instr. and Meth. A*, 287:324, 1990. doi:10.1016/0168-9002(90)91817-U.

[66] H. Poth. Electron cooling: Theory, experiment, application. *Phys. Rep.*, 196:135, 1990. doi:10.1016/0370-1573(90)90040-9.

[67] L. Jr. Spitzer. *Physics of Fully Ionized Gases*. Interscience Publishers, 2nd edition, 1964.

[68] G. Zwicknagel. Electron cooling of ions and antiprotons in traps. In *Beam Cooling and Related Topics*, volume 821 of *AIP Conference Proceedings*, page 513, 2006. doi:10.1063/1.2190158.

[69] B. R. Beck, J. Fajans, and J. H. Malmberg. Temperature and anisotropic-temperature relaxation measurements in cold, pure-electron plasmas. *Phys. Plasmas*, 3:1250, 1996. doi:10.1063/1.871749.

[70] T. M. O'Neil. Centrifugal separation of a multi-species pure ion plasma. *Phys. Fluids*, 24:1447, 1981. doi:10.1063/1.863565.

[71] D. J. Wineland et al. Radiation-pressure cooling of bound resonant absorbers. *Phys. Rev. Lett.*, 40:1639, 1978. doi:10.1103/PhysRevLett.40.1639.

[72] W. Neuhauser et al. Optical-sideband cooling of visible atom cloud confined in parabolic well. *Phys. Rev. Lett.*, 41:233, 1978. doi:10.1103/PhysRevLett.41.233.

[73] K. Koo et al. Doppler cooling of Ca^+ ions in a Penning trap. *Phys. Rev. A*, 69:043402, 2004. doi:10.1103/PhysRevA.69.043402.

[74] D. J. Wineland and Wayne M. Itano. Laser cooling of atoms. *Phys. Rev. A*, 20:1521, 1979. doi:10.1103/PhysRevA.20.1521.

[75] W. M. Itano and D. J. Wineland. Laser cooling of ions stored in harmonic and penning traps. *Phys. Rev. A*, 25:35, 1982. doi:10.1103/PhysRevA.25.35.

[76] S. Stenholm. The semiclassical theory of laser cooling. *Rev. Mod. Phys.*, 58:699, 1986. doi:10.1103/RevModPhys.58.699.

[77] C. J. Foot. *Atomic Physics*. Oxford University Press Inc., New York, 2005.

[78] L. Schweikhard and A. G. Marshall. Excitation modes for fourier transform-ion cyclotron resonance mass spectrometry. *J. Am. Soc. Mass Spectrom.*, 4:433, 1993. doi:10.1016/1044-0305(93)80001-F.

[79] X.-P. Huang et al. Phase-locked rotation of crystallized non-neutral plasmas by rotating electric fields. *Phys. Rev. Lett.*, 80:73, 1998. doi:10.1103/PhysRevLett.80.73.

[80] H. F. Powell, D. M. Segal, and R. C. Thompson. Axialization of laser cooled magnesium ions in a penning trap. *Phys. Rev. Lett.*, 89:093003, 2002. doi:10.1103/PhysRevLett.89.093003.

[81] G. D. Alton. The sputter generation of negative-ion beams. *Nucl. Instr. and Meth. B*, 37-38:45, 1989. doi:10.1016/0168-9002(88)90028-9.

[82] R. Middleton. A versatile high intensity negative ion source. *Nucl. Instr. and Meth.*, 214:139, 1983. doi:10.1016/0167-5087(83)90580-X.

[83] B. Wolf. *Handbook of Ion Sources*. CRC Press, 1995.

[84] J. Meier. Matching of the beam from a negative-ion source for capture in a Penning trap, 2007. Diplomarbeit (University of Heidelberg).

[85] J. Bartschke. private communication, 2009. (XITON Photonics).

[86] S. Jochim. private communication, 2009.

[87] A. C. Riviere and D. R. Sweetman. Dissociation of H_2^+ and He^- by electric fields. *Phys. Rev. Lett.*, 5:560, 1960. doi:10.1103/PhysRevLett.5.560.

[88] M. Barat et al. Absolute detection efficiency of a microchannel plate detector for neutral atoms. *Rev. of Sci. Instr.*, 71:2050, 2000. doi:10.1063/1.1150615.

[89] H. Raimbault-Hartmann et al. A cylindrical penning trap for capture, mass selective cooling, and bunching of radioactive ion beams. *Nucl. Instr. and Meth. B*, 126:378, 1997. doi:10.1016/S0168-583X(96)01067-1.

[90] W. Demtröder. *Laser Spectroscopy*. Springer, Berlin, 3rd edition, 2002.

[91] U. Warring et al. High-resolution laser spectroscopy on the negative osmium ion. *Phys. Rev. Lett.*, 102:043001, 2009. doi:10.1103/PhysRevLett.102.043001.

[92] R. Loudon. *The quantum theory of light*. Oxford, 2nd edition, 1983.

[93] G. Audi, A. H. Wapstra, and C. Thibault. The AME2003 atomic mass evaluation (II): Tables, graphs and references. *Nucl. Phys. A*, 729:337, 2003. doi:10.1016/j.nuclphysa.2003.11.003.

[94] J. R. de Laeter et al. Atomic weights of the elements. *Pure Appl. Chem.*, 75:683, 2003. doi:10.1351/pac200375060683.

[95] H. Kopfermann. *Kernmomente*. Akademische Verlagsgesellschaft M.B.H., Frankfurt am Main, 2nd edition, 1956.

[96] J. Bauche and R.-J. Champeau. Recent progress in the theory of atomic isotope shift. *Adv. At. Mol. Phys.*, 12:39, 1976.

[97] P Aufmuth, K Heilig, and A Steudel. Changes in mean-square nuclear-charge radii from optical isotope shifts. *A. Data and Nucl. Data Tables*, 37:455, 1987. doi:10.1016/0092-640X(87)90028-3.

[98] W. C. Griffith et al. Improved limit on the permanent electric dipole moment of ^{199}Hg. *Phys. Rev. Lett.*, 102:101601, 2009. doi:10.1103/PhysRevLett.102.101601.

[99] E. U. Condon and G. H. Shortley. *The Theory of Atomic Spectra*. Cambridge Univ. Press, 1959.

[100] R. D. Kronig. The intensity of multiple lines and their Zeeman components. *Z. Phys.*, 31:885, 1925.

[101] A Sommerfeld and H Hönl. Intensity of multiplett-lines. *Sitzber. Preuss. Akad. Wiss. Phys.-Math. Kl.*, page 141, 1925.

[102] H. N. Russell. The intensities of lines in multiplets. *Nature*, 115:835, 1925. doi:10.1038/115835a0.

[103] P. A. M. Dirac. The elimination of the nodes in quantum mechanics. *Proc. Royal Soc. A*, 111:281, 1926.

[104] S. Kroger et al. Hyperfine structure and isotope shift of Osmium I. *Phys. Scr.*, 65:56, 2002. doi:10.1238/Physica.Regular.065a00056.

[105] S. Fritzsche. private communication, 2009.

[106] D. Gerlich. Ion-neutral collisions in a 22-pole trap at very-low energies. *Phys. Scr.*, T59:256, 1995. doi:10.1088/0031-8949/1995/T59/035.

[107] Y. Liu et al. In *Proceedings of the 19th Particle Accelerator Conference, Chicago*, volume 5, page 3885, 2001.

[108] G. Gabrielse et al. Precision mass spectroscopy of the antiproton and proton using simultaneously trapped particles. *Phys. Rev. Lett.*, 82:3198, 1999. doi:10.1103/PhysRevLett.82.3198.

[109] H. J. Metcalf and P. van der Straten. *Laser Cooling and Trapping*. Springer, 1999.

[110] A. Crubellier. Theory of laser evaporative cooling of trapped negative ions. I. Harmonically bound ions and RF traps. *J. Phys. B*, 23:3585, 1990. doi:10.1088/0953-4075/23/20/020.

ACKNOWLEDGMENTS – Thanks to...

Group Leader/Mentor	ALBAN KELLERBAUER
Post-Docs	MARCO AMORETTI CARLO CANALI
Team	JAN MEIER RAOUL HEYNE ARNE FISCHER CHRISTOPH MORHARD
Host Group	PROF. ULLRICH ALL MEMBERS
Distraction/Property Masters	MICHAEL SCHURICKE CHRISTIAN ROUX
Consultants	JOSÉ CRESPO LÓPEZ-URRUTIA SELIM JOCHIM ...
Construction	THOMAS WEBER ANNIKA ZWILLING
Mechanics	VOLKER MALLINGER MARTIN BECKMANN WORKSHOP GROUP
Special Effects	MANFRED KÖNIG ACCELERATOR GROUP
Script Corrections/Comments	ALBAN KELLERBAUER BILL CLELAND

To the whole MPIK group: Thanks for the wonderful time at the institute and the great opportunity to work with you – for discussions, advices, and various kinds of distractions.
I am very grateful for the continuing support from my family and friends.